

ADVANCED MATERIALS CHARACTERIZATION
BASED ON FULL FIELD DEFORMATION
MEASUREMENTS

by

A. PAIGE CARPENTIER

Presented to the Faculty of the Graduate School of
The University of Texas at Arlington in Partial Fulfillment
of the Requirements
for the Degree of

DOCTOR OF PHILOSOPHY

THE UNIVERSITY OF TEXAS AT ARLINGTON

August 2013

Copyright © by A. Paige Carpentier 2013

All Rights Reserved



Acknowledgements

I would like this opportunity to thank everyone who has made this thesis possible. I would never have been able to complete my thesis without the support of my committee members, family, and friends. I would especially like to thank my advisor, Dr. Andrew Makeev, who patiently guided and supported me throughout my research. Working with Dr. Makeev has been such a wonderful opportunity, and I am truly grateful for all the time and effort that he has spent with me over the past four years. He has been a true mentor and friend, and I am so fortunate to have had such an amazing advisor.

I would also like to thank Dr. Hubert Schreier for all the time he has spent with me over the past several years, helping me to understand the Vic3D analysis process. He has been incredibly helpful throughout my research, and I truly appreciate all of his efforts. I would like to thank Dr. Erian Armanios for introducing me into the aerospace engineering field, and who is largely responsible for my presence here today. My entire committee has been so wonderful and supportive. I thank Dr. Yuri Nikishkov, for always taking the time to answer my questions. Also, Dr. Chan, who has been such a wonderful teacher to me and always made himself available to answer any of my questions. It has been such a pleasure working with all of you, thank you.

Additionally, I would like to express my extreme gratitude to Brian Shonkwiler for all of his help in experimental work and Yihong He for his work in FEM. Their help has been invaluable for my research. Also, I would like to thank Bell Helicopter, Boeing, and Sikorsky for manufacturing the composite specimens used throughout this work.

I am so lucky to be surrounded by a loving family and wonderful friends who have always believed in me. I would especially like to thank my parents, John and Beth Carpentier, who have unconditionally supported me throughout my academic career. I

would also like to thank my sister, Kara Short, for always being a shoulder to lean on. I am truly blessed to have such a wonderful family.

I would like to personally acknowledge Dr. Mahera Philobos and Sandra Song, who have always given me confidence in my capabilities. They have guided me throughout my academic career, and have provided me with so many opportunities along the way. They have been mentors, and most of all friends. I can never thank them enough for all of their support. I am also grateful to Miguel Trigueiros for his strength and encouragement over the last few years. He has been a true inspiration for me. I would like to thank Ekaterina Bostaph for always being by my side and making this experience so memorable. To all of my friends and family, thank you so much for being so supportive. Finally, I owe everything in my life to god, who has blessed me with so much. Thank you.

July 22, 2014

Abstract

ADVANCED MATERIALS CHARACTERIZATION
BASED ON FULL FIELD DEFORMATION
MEASUREMENTS

A. Paige Carpentier, PhD

The University of Texas at Arlington, 2013

Supervising Professor: Andrew Makeev

Accurate stress–strain constitutive properties are essential for understanding the complex deformation and failure mechanisms for materials with highly anisotropic mechanical properties. Among such materials, glass-fiber- and carbon-fiber-reinforced polymer–matrix composites play a critical role in advanced structural designs. The large number of different methods and specimen types currently required to generate three-dimensional allowables for structural design slows down the material characterization. Also, some of the material constitutive properties are never measured due to the prohibitive cost of the specimens needed. This work shows that simple short-beam shear (SBS) specimens are well-suited for measurement of multiple constitutive properties for composite materials and that can enable a major shift toward accurate material characterization. The material characterization is based on the digital image correlation (DIC) full-field deformation measurement.

The full-field-deformation measurement enables additional flexibility for assessment of stress–strain relations, compared to the conventional strain gages. Complex strain distributions, including strong gradients, can be captured. Such flexibility enables simpler test-specimen design and reduces the number of different specimen types required for assessment of stress–strain constitutive behavior. Two key elements

show advantage of using DIC in the SBS tests. First, tensile, compressive, and shear stress–strain relations are measured in a single experiment. Second, a counter-intuitive feasibility of closed-form stress and modulus models, normally applicable to long beams, is demonstrated for short-beam specimens. The modulus and stress–strain data are presented for glass/epoxy and carbon/epoxy material systems. The applicability of the developed method to static, fatigue, and impact load rates is also demonstrated.

In a practical method to determine stress-strain constitutive relations, the stress approximation must be independent of the deformation measurements, independent of the material properties (geometric stress approximation), and be simple for use in the industry. A remarkable benefit of the full-field deformation measurement is that it lets us observe the physical phenomena of the deformation which enables the derivation of simple and accurate geometric stress approximations. In particular, linear axial through the thickness strain distributions consistently measured in composite short-beam specimens allow a rigorous derivation of extremely simple stress approximations. The observation of linear through the thickness axial strain distributions has become the basis for eliminating the need of using Bernoulli-Euler kinematic assumptions of the rigid cross sections remaining perpendicular to the beam neutral axis throughout the deformation. Such assumptions are not consistent with the deformation mechanisms and therefore are arguable as a rigorous basis for stress approximation. Simple stress approximations are derived in this work based on the observations from the full-field deformation measurements; accuracy of such approximations are verified; and their limitations determined.

Table of Contents

Acknowledgements	iii
Abstract	v
List of Illustrations	ix
List of Tables	xv
Chapter 1 Introduction.....	1
1.1 Motivation	1
1.2 Objective and Approach	4
Chapter 2 Literature Survey	6
2.1 Short Beam Shear Test Method	6
2.2 Digital Image Correlation	11
Chapter 3 Three Dimensional Material Characterization.....	16
3.1 Experimental Description.....	16
3.1 Closed Form Stress and Modulus Approximations	27
3.3 Experimental Results for S2-Glass/E773-Epoxy Composites.....	35
3.4 Experimental Results for E-Glass/5216-Epoxy Composites	46
3.5 Experimental Results for IM7-Carbon/8552-Epoxy Composites.....	49
3.4 DIC Based Axial Strain Distribution Measurements	72
3.6 Application of the Short Beam Shear Method for Fatigue and Impact Loading	76
3.6.1 Fatigue Loading.....	76
3.6.2 Impact Loading.....	80
Chapter 4 Verification Tests.....	91
4.1 V-notch Specimens	91
4.1.1 Experimental Results IM7-carbon/8552-epoxy	93

4.1.2 Experimental Results E-glass/5216-epoxy	98
4.2 Four Point Bending Tests	103
4.2.1 Experimental Results for S2-glass/E773-epoxy	105
4.2.2 Experimental Results for IM7-carbon/8552-epoxy	108
4.3 Curved Beam Test.....	109
4.4 Interlaminar Compressive Tests.....	118
Chapter 5 DIC Errors in SBS Testing	122
5.1 Interpolation Errors	123
5.2 Filtering Errors	125
5.2.1 Static Tests.....	125
5.2.1.1 IM7-carbon/8552-epoxy	126
5.2.1.2 S2-glass/E773-epoxy	131
5.2.2 Impact Tests	134
Chapter 6 Conclusion and Future Work.....	137
References.....	142
Biographical Information	147

List of Illustrations

Figure 2-1 Test configuration and geometry of the short beam shear test..... 6

Figure 2-2 Speckle pattern using black and white spray paint 12

Figure 3-1 Unidirectional composite panel with SBS specimens machined in the 0°, 90° and through the thickness for three-dimensional material characterization 16

Figure 3-2 SBS coupons exhibit compression, shear, or tensile failure depending on the fiber directions, specimen geometry, and support size and location 18

Figure 3-3 Material properties obtained in each plane of loading for specimens cut in three different configurations from a unidirectional composite panel 19

Figure 3-4 (a) Typical shear failure of SBS specimen in the 1-2 and 1-3 plane (b) Typical tensile failure of SBS specimen in the 2-3 plane 20

Figure 3-5 A SBS test setup with 2-inch diameter loading nose 21

Figure 3-6 Axial, transverse, and shear full field DIC and FEM strain distributions for the 1-2 material plane at 95% of failure load for S2-glass/E773-epoxy SBS specimen..... 23

Figure 3-7 Axial, transverse, and shear full field DIC and FEM strain distributions for the 1-2 material plane at 95% of failure load for a S2-glass/E773-epoxy SBS specimen..... 24

Figure 3-8 Axial, transverse, and shear full field DIC and FEM strain distributions for the 2-3 material plane at 95% of failure load for a S2-glass/E773-epoxy SBS specimen..... 25

Figure 3-9 Typical (a) Normalized axial strain distribution and (b) interlaminar shear strain distribution across the thickness in a 2 mm (.079 in.) gage section in mid-region between support and loading at 93% failure load..... 26

Figure 3-10 Coordinate notation and axial strain distribution 27

Figure 3-11 Typical transverse normal stress-strain error term through the thickness of a carbon/epoxy SBS specimen at 70% failure load 33

Figure 3-12 Axial normal and interlaminar shear strain distribution extracted from DIC in the center region between loading nose and support.....	36
Figure 3-13 Typical through the thickness axial strain distribution for S2-glass/E73-epoxy SBS specimens loaded in the (1-3), (1-2), and (2-3) material planes at close to failure load.....	37
Figure 3-14 Interlaminar (1-3 material plane) shear stress-strain response for unidirectional S2-glass/E773-epoxy tape.....	38
Figure 3-15 In-plane (1-2 material plane) shear stress-strain response for unidirectional S2-glass/E773-epoxy tape.....	39
Figure 3-16 Closed Form and FEM comparison of Interlaminar (1-3) shear stress distribution for S2-glass/E773-epoxy unidirectional SBS specimen at close to failure load	45
Figure 3-17 Closed Form and FEM comparison of axial normal stress distribution for S2-glass/E773-epoxy unidirectional SBS specimen at close to failure load	46
Figure 3-18 Interlaminar (1-3 material plane) shear stress-strain response for E-glass/5216-epoxy unidirectional tape.....	48
Figure 3-19 Typical through the thickness normalized axial strain distributions for IM7-carbon/8552-epoxy SBS specimens loaded in the (1-3), (1-2), and (2-3) material planes	51
Figure 3-20 Interlaminar (1-3 material plane) shear stress-strain response for IM7-carbon/8552-epoxy unidirectional tape	52
Figure 3-21 In-plane (1-2 material plane) shear stress-strain response for IM7-carbon/8552-epoxy unidirectional tape	53
Figure 3-22 Comparison of FEM results and closed form (20) stress approximations for S2-glass/E773-epoxy and IM7-carbon/8552-epoxy SBS coupons.....	58

Figure 3-23 Through the thickness interlaminar (1-3) shear stress distribution comparison for IM7-carbon/8552-epoxy unidirectional SBS specimen at close to failure load	59
Figure 3-24 Alignment device for the ASTM D 2344 Wyoming SBS test fixture	62
Figure 3-25 Comparison of average interlaminar shear stress-strain curve for each span with FEM results for IM7-carbon/8552-epoxy SBS specimens.....	64
Figure 3-26 Comparison between closed form shear stress approximations and finite element predictions for the maximum shear stress of carbon/epoxy SBS specimens tested at different spans	65
Figure 3-27 Average interlaminar shear stress-strain curve for IM7-carbon/8552-epoxy tested at varying spans using the bilinear model (30) for the maximum shear stress approximation along with FEM based shear stress-strain curve	67
Figure 3-28 Lagrange strain tensor components measured on the short-beam specimen surface right before failure	71
Figure 3-29 Axial strain distribution through the thickness from the left gage region of a IM7-carbon/8552-epoxy SBS specimen tested with a s/t ratio = 4.8 at 85% failure load after coordinate transformations by ± 1 degrees.	74
Figure 3-30 Transformed axial strain distribution of both the left and right gage region for an IM7-carbon/8552-epoxy SBS specimen tested with a s/t ratio = 4.8 and loaded in the (1-3) material plane at 65% failure load	75
Figure 3-31 Interlaminar shear strain history for fatigue IM7/8552 SBS tests at peak cyclic stresses equal to 68% and 70% of the static interlaminar shear strength	79
Figure 3-32 Interlaminar shear stress-strain response for early stages of fatigue loading	80
Figure 3-33 Experimental setup for three point bending impact test with a two inch diameter impactor nose.....	82

Figure 3-34 Shear delamination failure of unidirectional S2-glass/E773-epoxy SBS specimens subject to drop-weight impact.....	83
Figure 3-35 FEM and experimental contact force history for S2-glass/E773-epoxy SBS impact tests run at a 4.4 m/s impact velocity (10^2 strain rate)	84
Figure 3-36 DIC data and FE results for surface strain components for a unidirectional .	86
Figure 3-37 Shear stress strain responses for unidirectional S2-glass/E773-epoxy SBS specimens subjected to quasi static and 4.4 m/s impact tests	88
Figure 4-1 V-notch test fixture and specimen dimensions.....	92
Figure 4-2 Comparison of average measured interlaminar (1-3) shear stress-strain response from the SBS using beam theory (19) stress approximation and the V-notch test for IM7-carbon/8552-epoxy unidirectional composite tape	94
Figure 4-3 Comparison of average measured interlaminar (1-3) shear stress-strain response from the SBS test using bilinear (30) stress model and the V-notch test for IM7-carbon/8552-epoxy unidirectional composite tape	95
Figure 4-4 In-plane shear stress-strain response for IM7-carbon/8552-epoxy unidirectional tape V-notch specimens in the (2-3) material plane	96
Figure 4-5 Comparison of interlaminar shear stress-strain response from the SBS test method using beam theory (4) stress approximations and the V-notch test for E-glass/5216-epoxy unidirectional composite tape	99
Figure 4-6 Comparison of interlaminar shear stress-strain response from the SBS test method using the bilinear model (30) for shear stress approximations and the V-notch test for E-glass/5216-epoxy unidirectional composite tape.	102
Figure 4-7 Test configuration and geometry of the four point bending test	104
Figure 4-8 Typical axial strain distribution for S2-glass/E773 epoxy FPB specimen at 95% failure load in the (1-3) principal material plane	105

Figure 4-9 Curved beam geometry and schematic of a curved beam under four point bending	109
Figure 4-10 A curved-beam test setup and the DIC measured transverse tensile strain distribution right before delamination failure	113
Figure 4-11 ILT stress-strain response of unidirectional curved-beam coupons CB1-CB6	114
Figure 4-12 ILT stress-strain response of unidirectional curved-beam coupons CB7-CB14	118
Figure 4-13 A compression test setup and typical DIC measured transverse compressive strain distribution	119
Figure 4-14 Interlaminar compressive stress-strain response for IM7-carbon/8552-epoxy short beams machined and loaded through the thickness direction.....	120
Figure 5-1 A 300x300 pixel sample of an IM7/8552 SBS specimen surface image used for interpolation error study with corresponding subset size.....	123
Figure 5-2 Interpolation bias as a function of subpixel location for different interpolation filters used in Vic3D/2D software analysis	124
Figure 5-3 Filtered and unfiltered interlaminar shear strain distribution through the thickness and between supports of an FEM simulated IM78552 SBS specimen at close to failure loads (a) without noise (b) with noise.....	129
Figure 5-4 Filtered and unfiltered axial strain distribution through the thickness and between supports of an FEM simulated IM78552 SBS specimen at close to failure load a) without noise (b) with noise.....	130
Figure 5-5 Filtered and unfiltered interlaminar shear strain distribution through the thickness and between supports of an FEM simulated S2E773 SBS specimen at close to failure load (a) without noise (b) with noise.....	132

Figure 5-6 Filtered and unfiltered axial strain distribution through the thickness and between supports of an FEM simulated S2E773 SBS specimen at close to failure load (a) without noise (b) with noise..... 133

Figure 5-7 Interlaminar shear strain distribution through the thickness and between supports of an S2/E773 SBS specimen subject to an initial impact velocity of 4.4 m/s at 240 μ s after initial impact based on FEM strains and Gaussian filtered FEM strains (a) without noise (b) with noise..... 136

List of Tables

Table 3-1 S2-glass/381-epoxy Material Constitutive Properties Generated for the Interlaminar (1-3) Material Plane	41
Table 3-2 S2-glass/381-epoxy Material Constitutive Properties Generated for the in-plane (1-2) Material Plane.....	42
Table 3-3 S2-glass/E773-epoxy Material Constitutive Properties Generated for the (2-3) Material Plane from 90° Specimens	43
Table 3-4 E-glass/5216-epoxy Material Constitutive Properties Generated for the (1-3) Material Plane	49
Table 3-5 IM7-carbon/8552-epoxy Material Constitutive Properties Generated for the (1-3) Material Plane.	54
Table 3-6 IM7-carbon/8552-epoxy Material Constitutive Properties Generated for the (1-2) Material Plane.....	55
Table 3-7 IM7-carbon/8552-epoxy Material Constitutive Properties Generated for the (2-3) Material Plane.....	56
Table 3-8 Updated shear properties for IM7-carbon/8552-epoxy unidirectional composite tape using the bilinear model from Ref. [19]	60
Table 3-9 IM7-Carbon/8552-Epoxy material properties for various s/t ratios (English units).....	68
Table 3-10 IM7-Carbon/8552-Epoxy material properties for various s/t ratios (SI units).	69
Table 3-11 Interlaminar tensile and compressive modulus values measured based on the short-beam tests.	72
Table 3-12 Specimen dimension, failure loads and shear properties for unidirectional S2-glass/E773-epoxy prepreg tape measured from 4.4 m/s impact tests	89

Table 3-13 Comparison of shear properties under quasi static and 4.4 m/s impact tests for unidirectional S2-glass/E773-epoxy prepreg tape	90
Table 4-1 IM7-carbon/8552-epoxy unidirectional V-notch interlaminar (1-3) shear parameters	97
Table 4-2 IM7-carbon/8552-epoxy unidirectional V-notch in-plane (2-3) shear parameters	98
Table 4-3 E-glass/5216-epoxy unidirectional V-notch interlaminar (1-3) shear parameters	100
Table 4-4 Updated shear results for SBS E-glass/5216-epoxy unidirectional composite tape specimens using the bilinear model Eq. (30)	101
Table 4-5 S2-glass/E773-epoxy Tensile and Compressive Moduli results for Four Point Bending Tests tested in the (1-3) material plane	106
Table 4-6 S2-glass/E773-epoxy Tensile and Compressive Moduli results for Four Point Bending Tests tested in the (1-2) material plane	107
Table 4-7 IM7-carbon/8552-epoxy Tensile and Compressive Moduli results for Four Point Bending Tests	108
Table 4-8 ILT modulus values measured using the first batch of unidirectional 25.4-mm (1-in) wide curved-beam coupons.....	115
Table 4-9 ILT modulus values measured using the second batch of unidirectional 12.7-mm (0.5-in) wide curved-beam coupons.....	117
Table 4-10 Interlaminar compressive modulus values measured using IM7-carbon/8552-epoxy thick panel composite beams machined and loaded in the thickness direction...	121

Chapter 1

Introduction

1.1 Motivation

Highly anisotropic composite materials are becoming increasingly popular in structural design due to their ability to tailor many of their mechanical properties to the demanding requirements of advanced structural designs in various applications. Analysis of mechanical behavior for all materials and structures requires knowledge of material stress-strain constitutive properties. A rapid development of a large number of structural materials with highly-anisotropic mechanical properties, including glass and carbon-reinforced polymer-matrix composites, left accurate characterization of their constitutive properties behind. The lack of accurate material properties needed for understanding of the deformation and failure mechanisms causes significant delays in qualification of composite materials for structural applications, and results in extremely conservative designs. Structural analysis of composites oftentimes requires accurate assessment of their three-dimensional stress and deformation states to understand complex failure mechanisms [1]. Therefore, accurate three dimensional stress-strain relations are needed.

Standard techniques for assessment of stress-strain constitutive relations for materials are currently based on resistance strain gage measurements. Strain gages measure a “point” strain over an average of the gage area imposing constraints on the test specimen design. Full field deformation measurement techniques, such as DIC, can be used to assess strains over an entire surface of a specimen. Such techniques enable additional flexibility for assessment of stress-strain relations, compared to conventional strain gages. Complex strain distributions, including strong gradients, can be evaluated. This is a major advantage to using the full field deformation measurement techniques,

which can change the philosophy of the experimental methods to determine stress-strain constitutive relations from the measurement of a single material property to measuring multiple stress-strain relations in a single experiment. In particular, there is a strong demand to reduce the number of different test methods to fully characterize three-dimensional constitutive properties of composite materials. The fundamental shift in the development of methods to determine stress-strain curves to full-field deformation measurement will meet such demand and enable much simpler test/specimen designs to capture some of the material properties for structural analysis, which are currently not measured but assumed due to the prohibitive cost to measure such properties using conventional strain gage based techniques.

In a method to measure constitutive properties, the stress components corresponding to the measured strain component values must be calculated to determine the material stress-strain constitutive behavior. Ideally the stress approximations should be material independent, i.e. depend solely on the test/specimen geometry and loading conditions. Full-field deformation measurements allow us to physically observe the complex deformation of the test specimen, and assess the strain distributions throughout the surface, which is key in developing simple and accurate geometric stress approximations. In particular, linear axial through the thickness strain distributions, consistently measured in composite short beam specimens, throughout three-point bend loading allow a rigorous derivation of simple stress approximations. These observations enable such simple stress solutions to be developed without using the Bernoulli-Euler kinematic assumptions which state that plane sections initially perpendicular to the centroidal axis, remain plane and perpendicular to the axis after deformation [2]. Inconsistency of the Bernoulli-Euler assumptions in neglecting transverse normal stresses to derive simple closed-form approximations for the axial normal stresses and

the shear stresses in the classical beam theories has often been debated in the engineering community, and has led to attempts to increase the fidelity of the beam theories to support “more accurate” stress formulations. It is worth noting that such attempts were at the best not useful for a practical test method due to the complexity of the calculations [3]. Simple shear stress and axial modulus approximations are derived in this work based on linear axial strain distribution observations from the full-field deformation measurements; the accuracy of such simple stress and modulus approximations verified; and their limitations determined.

The short beam shear (SBS) test method combined with digital image correlation (DIC) based full field deformation measurements can potentially be extended to assess multiple material properties, in particular the axial normal tensile and compressive modulus values, Poisson’s ratio, and the interlaminar shear stress-strain curve in the plane of loading using a single test. And SBS coupons can be machined in the principal material directions from a single unidirectional panel to determine the three-dimensional stress-strain relations in the principal material coordinate system. Methods which are able to capture multiple material properties in a composite test specimen in a single experiment can drastically reduce the amount of testing required for material characterization. Such methods must be based on full-field measurement techniques which offer the flexibility to capture complex strain distributions.

SBS test coupons are among the simplest to manufacture and test at various load rates. Test specimens could be machined in the zero-degree and 90-degree from a single unidirectional panel and loaded in the principal material planes to characterize three dimensional constitutive relations of composite material systems. In addition thick panel composites can be manufactured and machined through the thickness to measure the interlaminar tensile and compressive modulus and interlaminar tensile strength.

Simple stress approximations, derived from static equilibrium, are found to apply to fatigue and low velocity impact loading conditions. The shear stress-strain response can be determined for various loading conditions using the SBS test method combined with DIC full field deformation measurements.

1.2 Objective and Approach

The purpose of this work is to develop a simple test method that can be used for accurate measurement of three dimensional material constitutive relations for composite materials. The short beam shear test method coupled with DIC full field deformation measurements is introduced in this work as a viable test method for the full three-dimensional characterization of stress-strain constitutive properties of composite materials. Observations of linear axial strain distributions through the thickness of the specimen in the region far from loading nose and support till failure allow for simple shear stress and axial modulus solutions to be derived. This observation enables the axial tensile and compressive Young's modulus, Poisson's ratio, and nonlinear shear stress-strain response to be measured in all three principal material planes using the developed test method. In particular, a single SBS specimen will be demonstrated to generate these material properties in the plane of loading. In addition, consistent interlaminar shear failure when loaded in the (1-3) material plane will be demonstrated using a modified short beam shear test configuration allowing interlaminar shear strength to be assessed for each of the material systems in this work. SBS specimens will be machined in the zero-degree and 90-degree directions and loaded in the principal material planes for multiple material systems to demonstrate three-dimensional characterization capabilities of the developed SBS test method. Thick panel composites machined in the thickness direction enable assessment of interlaminar tensile and compressive

properties. Furthermore the application of the SBS test method for fatigue and impact loading conditions will be demonstrated. The applicability of the simple stress solution will be determined for different test configurations, for different material systems, and for different loading rates. The reliability of the DIC-based full field strain tensors will also be considered.

Material properties determined from this test method will be verified using alternative test methods, finite element method (FEM) based analysis, and published material properties. The composite material systems selected for the investigation are the unidirectional S2-glass/E773-epoxy prepreg tape, the unidirectional E-glass/5216-epoxy prepreg tape and the unidirectional IM7-carbon/8552-epoxy prepreg tape.

Chapter 2

Literature Survey

2.1 Short Beam Shear Test Method

In a short beam shear test, a specimen with a short span and uniform rectangular cross section is loaded under three point bending so that shear failure occurs. A typical short beam test configuration is shown in Figure 2-1.

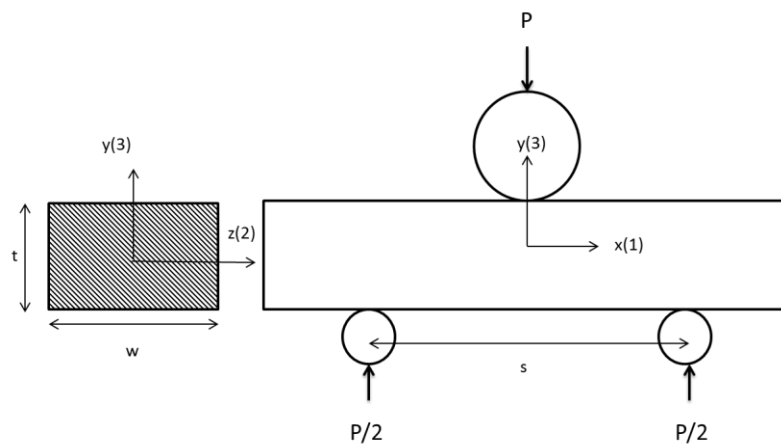


Figure 2-1 Test configuration and geometry of the short beam shear test

The short beam rests upon two cylindrical supports and a load is applied through the center of the specimen through a cylindrical loading nose. A standard short beam shear test method is outlined in the American Society for Testing and Materials (ASTM) D 2344 [4] and was designed as a method to measure short beam strength of composite materials. A support diameter of .125 in. (3.2mm) and loading nose diameter of .25 in. (6.3 mm) is recommended in the standard test method. In addition the standard recommends a width to thickness (w/t) ratio of 2 and a span to thickness (s/t) ratio of 4 or 5 [4]. In the current work the specimen geometry and test configuration are modified.

A strong interlaminar shear strain gradient through the thickness of the specimen makes strain gages impractical for accurate peak shear strain measurements. A conventional strain gage that would be suitable for measuring the peak shear strain would need to be narrow enough to minimize the effect of the strong gradient. In addition, the use of strain gages for this test method would require precise knowledge of the location of the neutral axis for each specimen. This location is not always known, for instance materials such as unidirectional composites often exhibit different tensile and compressive axial stiffness causing a shift in the neutral axis [5]. For these reasons the short beam shear method has traditionally been used for assessment of the interlaminar shear strength, and not the stress-strain constitutive model. The short beam shear test is one of the most common shear strength tests due to the ease of manufacturing and cost efficiency of the specimen design [6]. Full field deformation measurements overcame the conventional strain gage limitations in the SBS tests and proved the validity of simple shear stress models to characterize interlaminar shear stress-strain behavior [7].

From Bernoulli-Euler kinematic assumptions of classical beam theory, the beam deforms with a rigid cross section that remains perpendicular to the neutral axis [8]. From this assumption it can be derived that the axial strain varies linearly through the thickness. However, the classical beam theory also assumes that transverse normal stress is zero which is not consistent with the rigid cross-section kinematic assumption. Such inconsistency resulted in many debates in the engineering community [3, 9]. The following axial stress solution is derived for long beams subject to bending loads using Bernoulli-Euler assumptions

$$\sigma_{xx} = -\frac{My}{I} \quad (1)$$

where I is the second moment of area, and M is the bending moment. For long beams with rectangular cross sections this equation becomes

$$\tau_{xy} = \frac{3P}{4A} \left(1 - \left(\frac{2y}{h} \right)^2 \right) \quad (2)$$

which can be solved for the maximum shear stress (3) by substituting $y = 0$, based on boundary conditions.

$$\tau_{xy}^{\max} \approx \frac{3}{4} \frac{P}{A} \quad (3)$$

where P is the applied force and A is the cross sectional area. Classical beam theory solutions are suggested by the ASTM D 2399 standard SBS test method to be used to approximate the short beam strength of the material [4].

Fiber reinforced polymer composites exhibit nonlinear stress-strain behavior. In particular, the matrix dominated interlaminar shear stress-strain response becomes nonlinear at low shear strains, above 1%. A Ramberg-Osgood equation (5) is used to generalize the interlaminar shear stress-strain relationship in Ref. [7]. This equation represents a general practice for stress-strain approximation of nonlinear behavior. As the Hooke's law generalizes the stress strain response for linear elastic material behavior, the log-linear Ramberg-Osgood equation has been used as the simplest expression for nonlinear stress-strain constitutive behavior [10].

$$\gamma_{ij} = \frac{\tau_{ij}}{G_{ij}} + \left(\frac{\tau_{ij}}{K_{ij}} \right)^{1/n_{ij}} \quad (4)$$

where K_{ij} and n_{ij} are parameters that define the nonlinear relationship between shear stress and shear strain. The Ramberg-Osgood equation (5) is commonly used in the approximation of nonlinear constitutive properties for metallic materials [11]. One of the

early applications of the Ramberg-Osgood equation to composite materials was by Renieri and Herakovich who implemented nonlinear material behavior in a quasi 3D FEM model using a 1 Dimensional Ramberg-Osgood relationship [12]. It should be noted that other mathematical expressions, including cubic polynomials, have also been used to characterize the nonlinear shear stress-strain relationship of composite materials [13].

The use of Eq. (4) for approximating the maximum shear stress for a short beam subject to three point bending is often debated [14-18]. Several FEM based studies found that the nonlinearity of the shear stress strain relationship reduces the maximum shear stress approximation in comparison with classical beam theory approximations [10, 12, 16, 17, 19]. In addition, the transverse normal stress concentrations introduced by the loading nose and supports can significantly affect the stress distributions in the short beam [12, 14, 17, 18, 20]. For this reason the ASTM D 2344 standard SBS test method outlined in [4], which is designed for measuring short beam strength of a material, using Eq. (4) for the maximum shear stress approximation, is recommended to be used only for quality control and material development and is discouraged as a method for measuring design allowables [21].

A method for measuring the interlaminar shear stress-strain response of unidirectional polymer composites using a combination of DIC full field deformation measurements and the SBS test method was first introduced in Ref. [7]. A linear axial strain distribution through the thickness of the short beam specimens is observed until failure for numerous composite material studies [7, 22]. The linear axial strain distribution through the thickness of the specimen proves the validity of simple shear stress models enabling us to obtain the interlaminar shear stress-strain relationship [7]. However, FEM based studies show that the maximum shear stress predicted by classical beam theory is not fully reached in the area between the loading nose and supports in the nonlinear

shear regime. The difference between the closed-form approximation (4) and FEM results becomes more pronounced close to material failure as nonlinearity in the shear stress-strain response becomes stronger [10]. For carbon/epoxy specimens tested at a span to thickness ratio of 5, the difference between stresses reaches a maximum of 15% at the failure load [10]. For glass/epoxy the shear stresses obtained using Eq. (4) stay within 5% of FEM based stresses as a result of the lower shear strength of this material [19].

A method to determine accurate interlaminar shear stress-strain behavior using the modified SBS test method with DIC based strain and FEM stress predictions was developed in References [10, 23]. Taking the FEM based stresses determined using the iterative procedure developed in References [10, 23] and comparing them with beam theory maximum interlaminar shear stress predictions for SBS specimens, a shear stress model was developed in Reference [19] to more accurately approximate the maximum shear stresses in a SBS test with a span to thickness ratio equal to 5.

$$\tau_{13}^{\max} = \begin{cases} \frac{3 P}{4 A}, & \frac{3 P}{4 A} \leq 6.8ksi \\ 0.8 \left(\frac{3 P}{4 A} - 6.8ksi \right) + 6.8ksi & \frac{3 P}{4 A} > 6.8ksi \end{cases} \quad (5)$$

This bilinear model approximates the maximum shear stress in a SBS specimen with less than 5% error when used for both glass/epoxy and carbon/epoxy specimens. However, this model does not account for varying support span to thickness (s/t) ratios, which changes the maximum shear stress of the short beam in the nonlinear regime [15]. It should be noted from Eq. (4) that the maximum interlaminar shear stress is considered to be independent of span length. However a number of studies where the s/t ratio of the SBS specimen was varied show an increase in “apparent” interlaminar shear strength with a decrease in s/t ratio [6, 24-27]. An FEM based study of the shear stress

distributions through the thickness of SBS carbon/epoxy and glass/epoxy specimens show that the maximum shear stresses at the mid-thickness of the specimens decrease with decreasing s/t ratios [15]. For composite specimens with various s/t ratios that are subject to the same applied force, the specimens with lower s/t ratios are subjected to lower shear stresses and therefore exhibit higher shear strength. Based on these studies it becomes apparent that the maximum shear stress in the short beam is geometrically dependent.

The SBS test method can be applied to various loading conditions. The application of the developed short beam method coupled with DIC based strains for fatigue loads was introduced in Reference [19]. Interlaminar shear S-N fatigue curves were generated for both glass/epoxy and carbon/epoxy unidirectional composite tape in Ref. [19] using a bilinear stress model (6) for more accurate shear stress approximation. Despite differences in material properties, including shear strength, of the two materials, the S-N curves generated for each were quite similar when normalized. The bilinear model was derived using an iterative FEM process [19].

2.2 Digital Image Correlation

Digital image correlation (DIC) is a non-contact method which acquires images of an object in digital form and performs analysis on the images to acquire sensor plane motions which can be converted into “full field” shape, deformation, and motion measurements of the object [28]. Typically, this method is implemented by dividing the images into subregions and matching these regions between undeformed and deformed images to acquire full field deformation measurements. The digital image correlation full field deformation measurement technique is becoming increasingly popular in experimental mechanics. Initially developed in the 1980’s as a two dimensional method for measuring planar displacements from in plane loading, the concept expanded to

stereo vision in the 1990's developing into a three dimensional non-contact deformation measurement technique [28]. Stereo vision involves two or more cameras creating multiple viewpoints of an object that are used to estimate the three dimensional deformation field on the surface of an object. Calibration of the stereo vision system is used to define the relationship between the cameras [29]. An initial image is taken of the object as a reference image, while subsequent images are taken once deformation occurs. The reference image is divided into square subregions, called subsets, whose side length corresponds to a specified number of pixels. Each subset is characterized by a unique grayscale pattern, determined in the reference image. In order to obtain unique grayscale patterns for each subset, the surface being analyzed must contain a random pattern. This is often accomplished by applying a random speckle pattern to the surface of the object using black and white spray paint. It is important when using this technique to make sure the paint properly adheres to the surface of the specimen and deforms with the specimen. An example of a typical spray paint speckle pattern is shown in Figure 2-2.

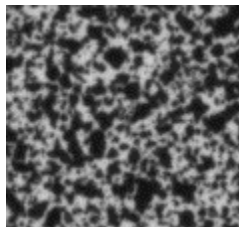


Figure 2-2 Speckle pattern using black and white spray paint

The digital image correlation method works by matching subset areas from the reference image to subset areas in the deformed image. It accounts for both translation and deformation by transforming the reference pixel coordinates to the deformed image

using subset shape functions. DIC displacement fields are not directly fit to measured data but are instead determined by optimizing the parameter vectors of the subset shape functions using a cost function, denoted as the optimization criterion. The subset shape functions place additional requirements on the resolution of the system for accurate displacement measurements [29]. For practical purposes a scale-invariant optimization criterion must be used to account for offsets in intensity patterns which can be caused by changes in lighting, changes in specimen reflectivity due to strain, and changes to the orientation of the specimen. The term digital image correlation is derived from using such a criterion, referred to as the normalized cross-correlation. An alternative scale invariant optimization criterion, zero-mean normalized sum of square differences, is implemented in Vic3D [29] to improve the efficiency of the optimization process. This technique accounts for changes in both brightness and contrast between images. Both of these criterion are based on the assumption that all lighting changes are approximately constant over the size scale of the subset [29].

To obtain sub-pixel accuracy, the matching criterion must be evaluated at non integer locations. This requires the grayscale values and gradients of the grayscales to be interpolated. Common interpolators, including polynomial and B-spline, introduce errors in the DIC measurements by altering the phase and amplitude of the input signal. One method of reducing these errors is by using a highly contrasted uniform speckle pattern [30]. The size of the speckles is also important in determining sub pixel accuracy. Speckles that are too small will cause aliasing and will bias the displacement measurements. Instead the speckles need to be large enough that they are oversampled as a feature. The optimal size of a speckle is based on the subset window size, but a typical rule of thumb is no smaller than 3 pixels [29].

The DIC analysis software used throughout this work is Vic3D by Correlated Solutions [29]. Among the reasons 3D measurements is used for these tests is the contribution of the out-of-plane displacement to the in-plane Lagrange strain tensor components. There are three main user defined parameters in Vic3D software; subset size, step size and filter size. The subset size refers to the subset region previously discussed, and the step size refers to the number of pixels between the midpoint of neighboring subsets. Displacement data is obtained for each individual subset. The displacement field is then numerically differentiated using a strain computation algorithm in Vic3D [29] to compute the Lagrangian strain tensor. One benefit of image correlation is that subset regions are overlapping, therefore, creating a dense data set. The strain fields are smoothed using a Gaussian smoothing filter. The filter size defines the number of data points, n , used in an $n \times n$ filter for strain calculations. Choosing the correct subset size, step size, and filter size is an important step to obtaining meaningful results. A compromise between higher resolution and less noise needs to be reached to obtain the optimal results. Typically it is desirable to have the smallest subset size possible while still large enough to ensure accuracy and isotropy in the subset matching process. A general rule of thumb is to have each subset contain at least 3 by 3 speckles [29]. The step size determines how many data points the analysis will use. Increasing the number of data points can increase the processing time required by the software to analyze the data. Also, the step size along with the filter size dictate the size of the strain window, which can be thought of as a virtual strain gauge. The input parameter for the filter size is defined in terms of data points. The strain window is the number of data points multiplied by the number of pixels between data points, or step size. By increasing the step size, this will increase the strain window. Therefore there is an inverse relationship between the step size and filter size in order to maintain a consistent strain

window. As a result the step size has less effect on the uncertainty of the DIC displacement fields than the strain calculations [31]. Determining the optimal strain window size for each test is important in the accuracy of the strain calculations. A strain window size that is too small will not filter out a sufficient amount of noise, and a strain window size that is too large can alter the strain distribution, especially in regions of strong strain gradients. These effects will be discussed in further detail later in this work.

Chapter 3

Three Dimensional Material Characterization

3.1 Experimental Description

Short beam shear coupons are prismatic coupons with a rectangular cross section. For unidirectional composite materials the three principal material planes are denoted 1-2, 1-3, and 2-3. As shown in Figure 3-1, the fiber direction is denoted as 1 (0°), the in plane transverse direction is denoted as 2 (90°), and the laminate thickness (interlaminar) direction is denoted as 3 [5]. Unidirectional composites are considered orthotropic materials, having two planes of symmetry, where nine independent material constants exist. For such materials the shear stresses and strains are independent from the normal stresses and strains as well as other shear stresses and strains from separate planes [32].

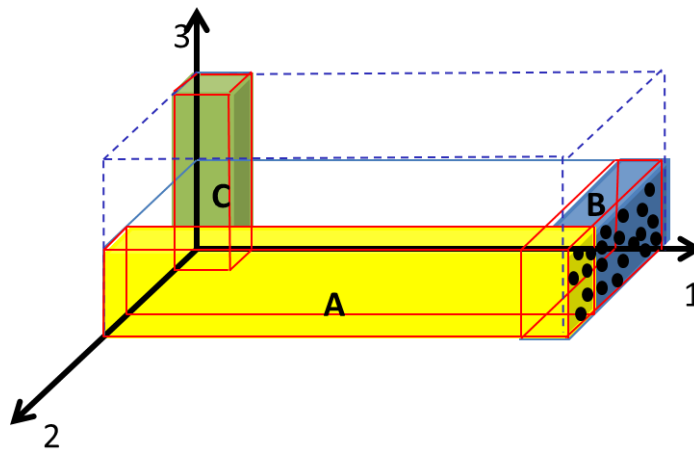


Figure 3-1 Unidirectional composite panel with SBS specimens machined in the 0° , 90° and through the thickness for three-dimensional material characterization

In this work both carbon/epoxy and glass/epoxy unidirectional composite SBS specimens machined and loaded in the three principal material planes are considered.

For quasi-static testing each specimen was placed in a servohydraulic load frame and monotonically loaded at .05 in. (1.27 mm) /min crosshead displacement rate until failure. ASTM standard designates the width to thickness (w/t) ratio as 2:1 and the span to thickness (s/t) ratio as 4 or 5. The loading nose diameter is specified to be .25 in. (6.4 mm), with a .125 in. (3.2 mm) diameter supports [4]. A typical SBS test configuration can be seen in Figure 2-1. An alternative configuration to the ASTM test configuration is used throughout this study. Several different specimen dimensions and loading configurations were tested in order to determine the optimum test configurations that result in the desired failure mode. The failure mode in the SBS tests varies with fiber directions, specimen geometry, and support size and location. Figure 3-2 schematically shows compression failure under the loading nose for a unidirectional 0.25 in. (6.4 mm) thick carbon/epoxy SBS specimen with a 0.25 in. (6.4 mm) diameter loading nose; shear delamination failure in the similar specimen once the loading nose diameter has been increased to 4 inches; and matrix tensile failure in a 90-degree specimen. The width is reduced from the ASTM recommended 200% to 100% of the specimen thickness in order to create a more uniform strain distribution through the width of the specimen away from the supports [6]. The loading nose diameter is increased from the ASTM standard of .25 in. (6.4 mm) to 4 in. (101.6 mm) for carbon/epoxy specimens and 2 in. (50.5 mm) for glass/epoxy specimens in order to reduce compressive damage under the loading nose and prevent undesired failure modes. The standard lower support diameter of .125 in. (3.2 mm) is used throughout this study.

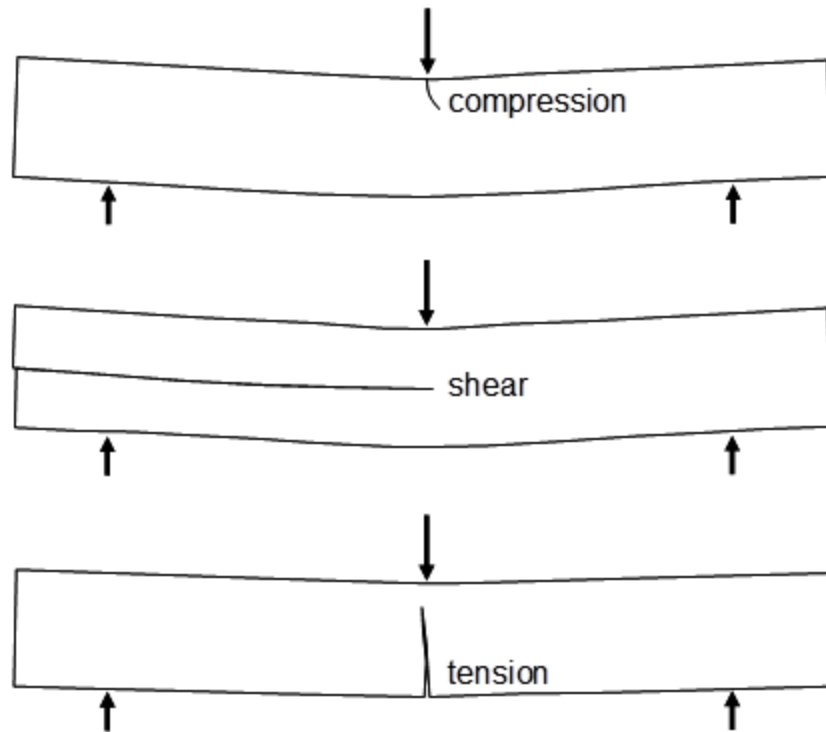


Figure 3-2 SBS coupons exhibit compression, shear, or tensile failure depending on the fiber directions, specimen geometry, and support size and location

As shown in Figure 3-1, the SBS specimens can be machined in the zero degree or 90 degree direction from a single unidirectional composite panel and loaded in any of the three principal material planes, 1-2, 1-3, or 2-3. In addition thick panel composites, $\frac{3}{4}$ inch to 1 inch, can be manufactured to obtain through the thickness short beam specimens. By loading the SBS specimens in the principal material planes, a complete set of 3D material constitutive properties can be generated. Successful three dimensional characterization of both carbon/epoxy and glass/epoxy specimens using the developed DIC technique was accomplished in the following References [22, 33]. Material properties that can be generated using this test method are included in Figure 3-3.

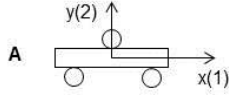
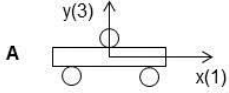
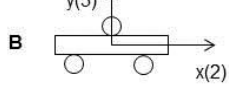
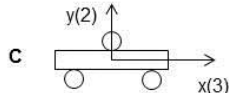
Material Plane	Measured Properties
 <p>A</p>	Axial Tensile Modulus, E_{11T} Axial Compressive Modulus, E_{11C} Poisson's Ratio, ν_{12} Shear Modulus, G_{12} Secant Intercept Modulus, K_{12} Exponent, n_{12}
 <p>A</p>	Axial Tensile Modulus, E_{11T} Axial Compressive Modulus, E_{11C} Poisson's Ratio, ν_{13} Shear Modulus, G_{13} Secant Intercept Modulus, K_{13} Exponent, n_{13}
 <p>B</p>	Axial Tensile Modulus, E_{22T} Axial Compressive Modulus, E_{22C} Poisson's Ratio, ν_{23} Shear Modulus, G_{23}
 <p>C</p>	Interlaminar Tensile Modulus, E_{33T} Interlaminar Compressive Modulus, E_{33C} Poisson's Ratio, ν_{23} Shear Modulus, G_{23}

Figure 3-3 Material properties obtained in each plane of loading for specimens cut in three different configurations from a unidirectional composite panel

Figure 3-3 lists the material properties that can be measured for each type of specimen, A B or C, and each loading plane, 1-2 1-3 or 2-3, using the developed static short beam test method. It is worth noting that for polymer composite short beam specimens loaded in the (2-3) principal material plane tensile failure is observed at low loads, preventing the nonlinear shear stress-strain response from being captured.

A typical tensile failure for SBS specimens loaded in the 2-3 material plane can be seen in Figure 3-4 (b). For materials loaded in the (1-2) and (1-3) material planes a typical shear failure initiates at the center of the specimen in the area of maximum shear stress between the loading nose and support and then propagates to the edge of the

specimen as seen in Figure 3-4 (a), allowing shear strength to be measured from these material planes.

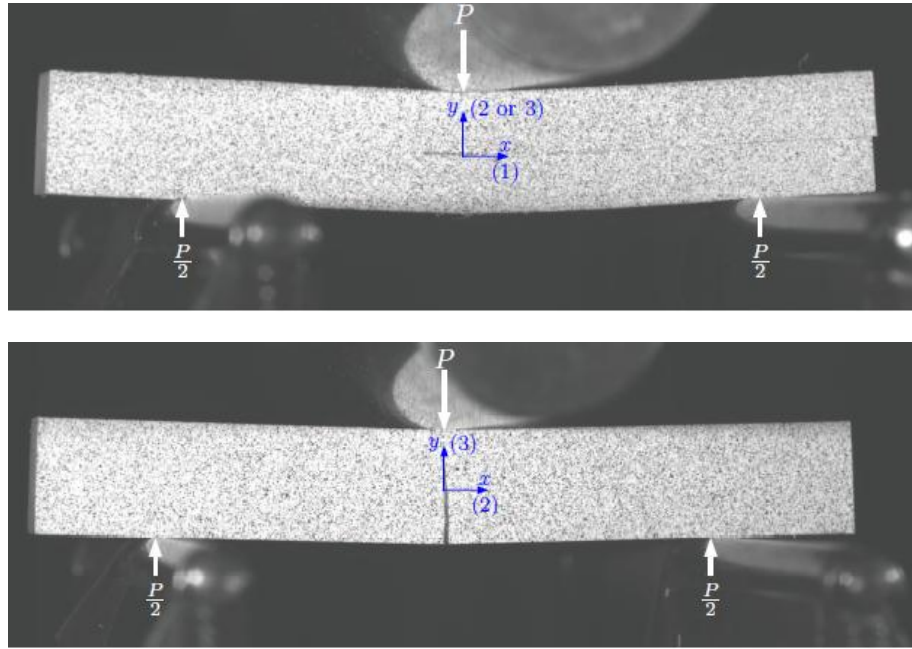


Figure 3-4 (a) Typical shear failure of SBS specimen in the 1-2 and 1-3 plane (b) Typical tensile failure of SBS specimen in the 2-3 plane

DIC software Vic3D is used in this work to assess the Green-Lagrange strain tensor components along the surface of the specimen [29]. A random pattern is applied to the surface of each specimen using black and white spray paint, making a similar pattern to that shown in Figure 2-2. While load is applied to the specimen, a sequence of images are obtained using a stereo camera system. The Vic3D software determines three dimensional positions before and after deformation by tracking the gray scale pattern for individual subsets throughout the acquired stereo image sequence [29]. The developed SBS test configuration using DIC full field deformation measurements can be seen in Figure 3-5 for a glass/epoxy SBS specimen with a 2 in. loading nose diameter.

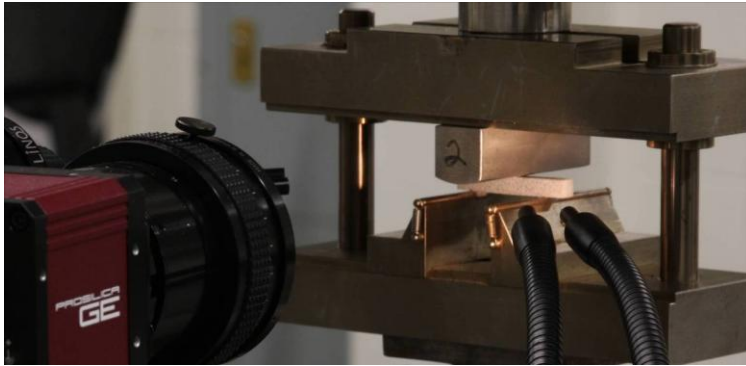


Figure 3-5 A SBS test setup with 2-inch diameter loading nose

As previously mentioned, the Green-Lagrange strain tensor is computed using a strain computation algorithm in the Vic3D software [29]. A typical axial, transverse, and shear surface strain distribution for an S2-glass/E773-epoxy loaded in the 1-2, 1-3, and 2-3 material planes can be seen in Figure 3-6, Figure 3-7, and Figure 3-8. Results of nonlinear three dimensional finite element simulations are also shown for comparison. Stress results generated from a nonlinear 3D FEM of a SBS specimen specified for each material system were used to verify the accuracy of simple closed form stress predictions throughout this study. The model was generated using ABAQUS finite element analysis software. First order (C3D8I) elements were utilized for this problem. Symmetry boundary conditions were used to model half width of the specimen. The nonlinear FEM includes geometric nonlinearity, material nonlinearity, and contact interaction. The loading nose and the lower supports are assumed to be rigid and modeled with cylindrical surfaces. Nonlinear shear stress-strain relations (5) are implemented in the material constitutive model through a user subroutine UMAT in the ABAQUS software. In the FEM, average measured values for shear properties, Young's moduli and Poisson's ratios are used. Observations of approximate transvers isotropic material behavior for both S2-glass/E773-epoxy and IM7-carbon/8552-epoxy allow the model to make the following assumptions; $G_{12}=G_{13}$, $K_{12}=K_{13}$, $n_{12}=n_{13}$, and $G_{23}=E_{22}/(2\times(1+\nu_{23}))$ for each

material system. Linear shear behavior is utilized in the 2-3 principal plane since the shear strain, γ_{23} , is negligible in the specimen sections. The FEM results used for static SBS comparison come from a model which generates accurate nonlinear shear stress-strain behavior using an iterative procedure developed in References [10, 23]. This procedure involves using initial shear properties obtained from DIC strains and closed form stress approximations (4) when running an initial simulation. The peak shear stresses in the region between support and loading nose are then plotted against the DIC peak shear strain measurements for each load step. The shear properties obtained from this shear stress-strain response are updated into the model, and a new FEM simulation is performed. This procedure continues till the shear properties converge. To further verify these results the full field strain distribution from FEM and DIC can be compared. Figure 3-6, Figure 3-7, and Figure 3-8 show typical engineering surface strain components obtained experimentally from DIC and analytically from FEM for S2-glass/E773-epoxy SBS specimens machined and loaded in the (1-2), (1-3), and (2-3) principal material planes which show good agreement at close to failure loads.

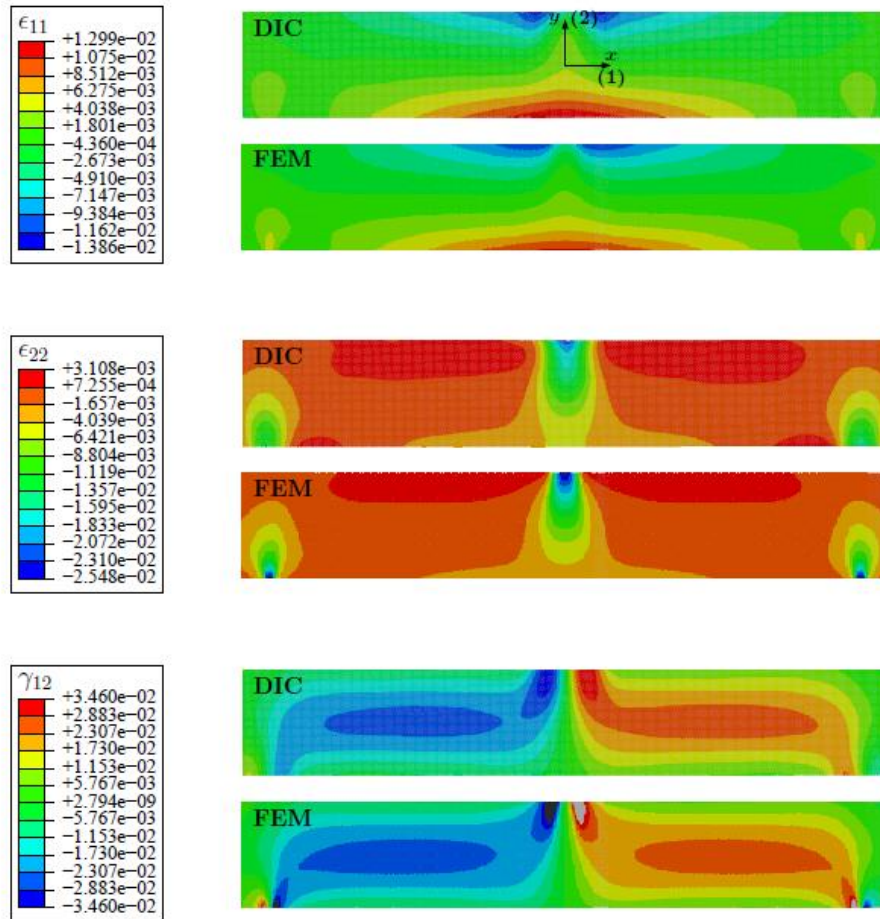


Figure 3-6 Axial, transverse, and shear full field DIC and FEM strain distributions for the 1-2 material plane at 95% of failure load for S2-glass/E773-epoxy SBS specimen

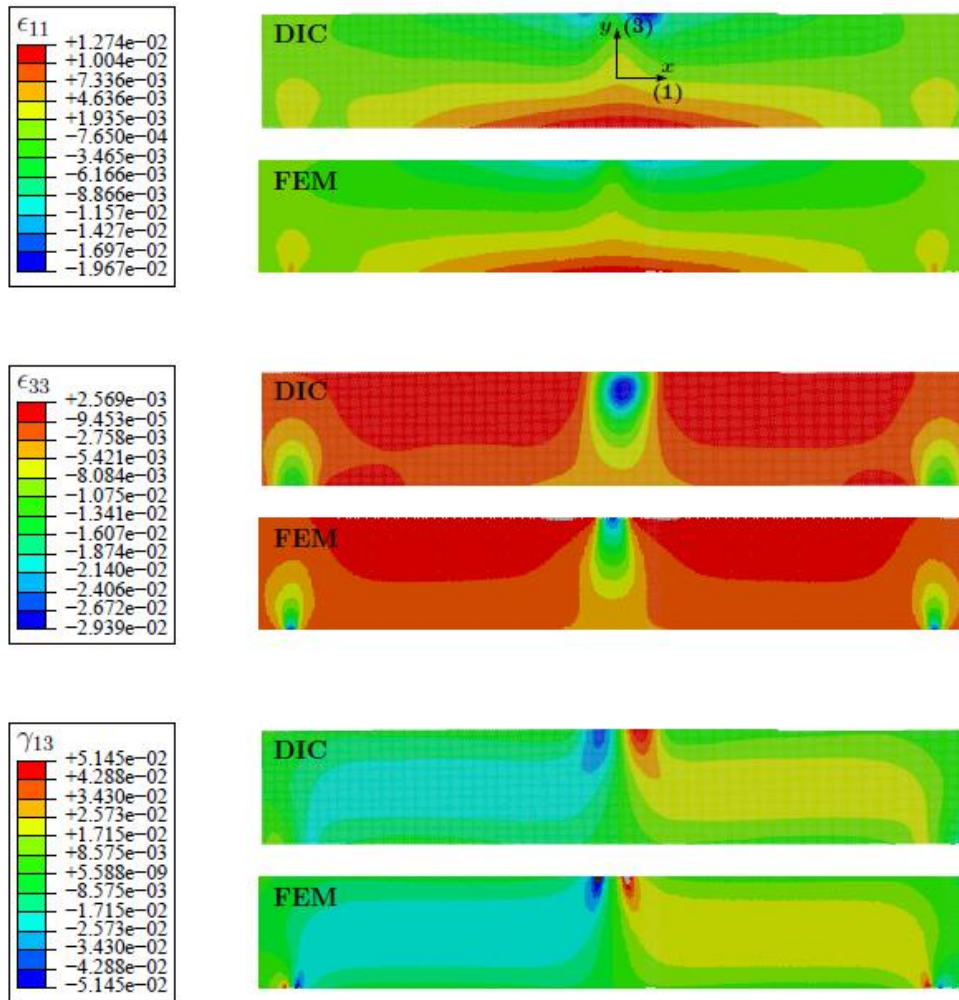


Figure 3-7 Axial, transverse, and shear full field DIC and FEM strain distributions for the 1-2 material plane at 95% of failure load for a S2-glass/E773-epoxy SBS specimen

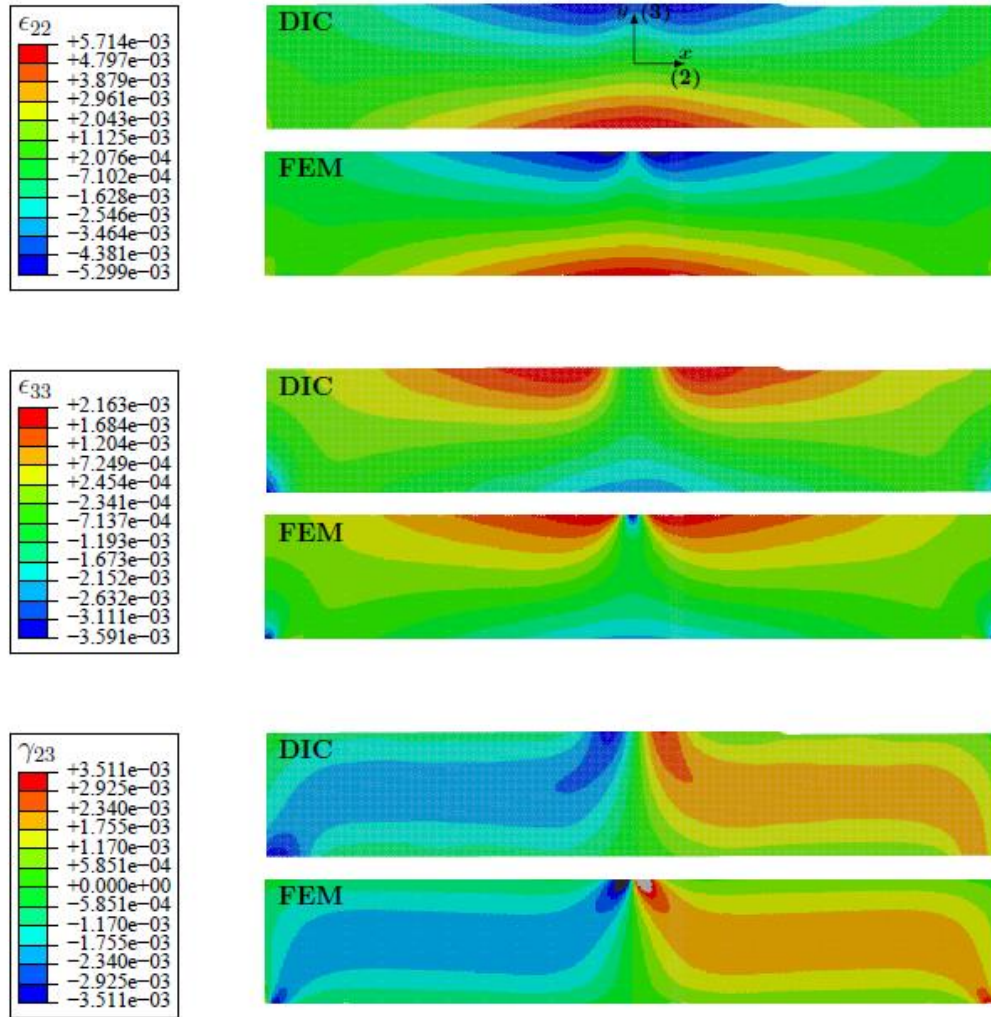


Figure 3-8 Axial, transverse, and shear full field DIC and FEM strain distributions for the 2-3 material plane at 95% of failure load for a S2-glass/E773-epoxy SBS specimen

Strains are extracted from a 2 mm gage region between the supports and the loading nose on both the left and right side. Figure 3-9 shows a typical (a) normalized axial strain distribution and (b) average interlaminar shear strain distribution extracted

from the 2 mm (.079 in) gauge region, at 93% of the failure load for S2-glass/E773-epoxy specimen.

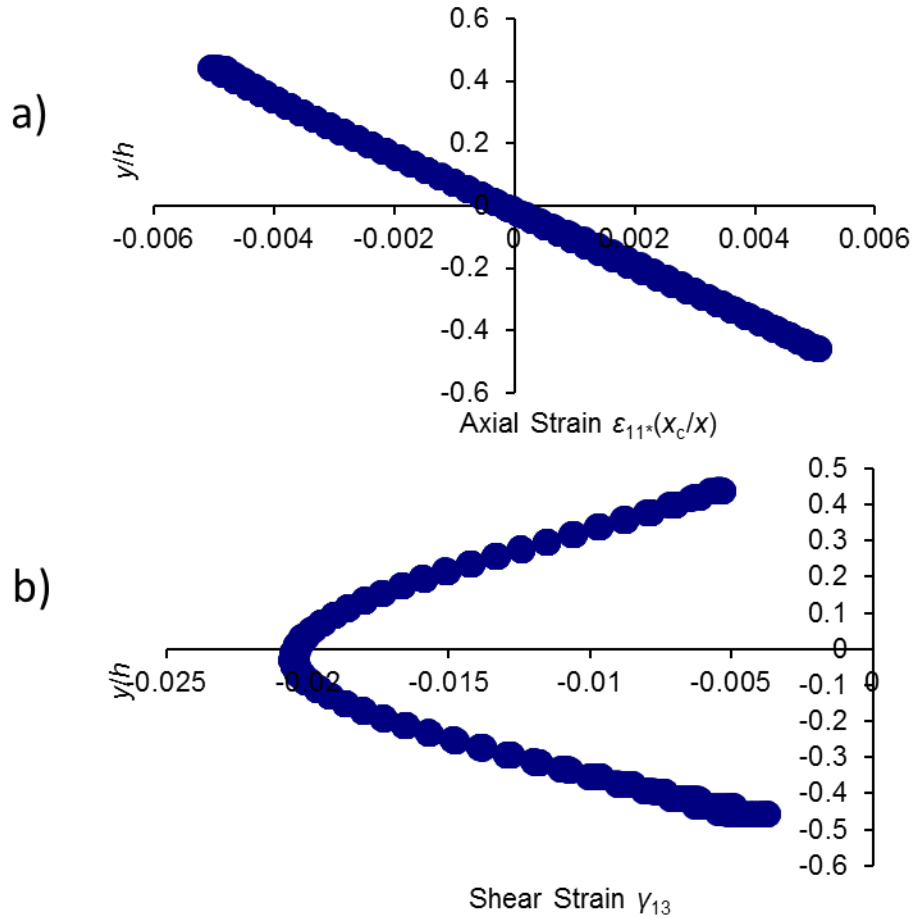


Figure 3-9 Typical (a) Normalized axial strain distribution and (b) interlaminar shear strain distribution across the thickness in a 2 mm (.079 in.) gage section in mid-region between support and loading at 93% failure load

Deformation measurements for the glass/epoxy and carbon/epoxy unidirectional tape composites under quasi-static loading conditions confirm close to linear axial strain distribution through the thickness of the SBS specimen thickness far from the loading nose and support, and a linear axial stress-strain response till failure.

3.1 Closed Form Stress and Modulus Approximations

As illustrated schematically in Figure 3-10, the axial strain distribution varies linearly through the thickness of the specimen until failure which allows for simple closed-form approximations for shear stresses as well as tensile and compressive axial moduli. The tensile and compressive axial moduli are not assumed to be the same, since some composites, such as carbon-fiber composites, have significant differences in their tensile and compressive behavior. Carbon-fiber composites are known to exhibit different tensile and compressive modulus behavior in the fiber direction where the material behavior is dominated by the anisotropic behavior of the carbon-fibers [34].

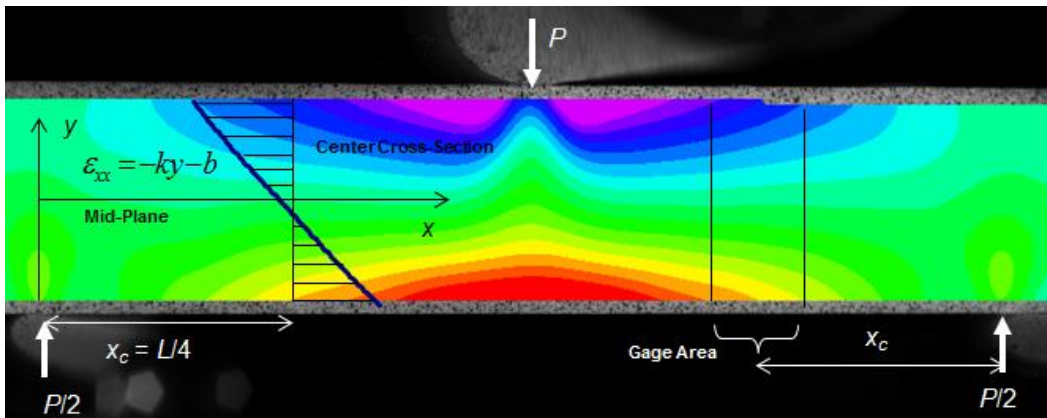


Figure 3-10 Coordinate notation and axial strain distribution

The linear axial strain distribution can be expressed as

$$\varepsilon_{xx} = -ky - b, \quad -\frac{h}{2} \leq y \leq \frac{h}{2} \quad (6)$$

where $y = -b/k$ corresponds to the neutral axes location of the composite test specimen. First we will derive the closed form moduli solution assuming that transverse normal stresses are negligible in the area between the loading nose and supports where we can express the linear axial tensile and compressive stresses using one-dimensional Hooke's law as

$$\sigma_{xx} = \begin{cases} E_T \varepsilon_{xx}, & -\frac{h}{2} \leq y \leq -\frac{b}{k} \\ E_c \varepsilon_{xx}, & -\frac{b}{k} \leq y \leq \frac{h}{2} \end{cases} \quad (7)$$

where E_T and E_c are the tensile and compressive axial moduli. The axial force and bending moment approximations for the specimen cross-section are

$$N = \int_{-\frac{h}{2}}^{\frac{h}{2}} \int_{-\frac{b}{k}}^{\frac{b}{k}} \sigma_{xx} dy dz = 0 \quad (8)$$

and

$$M = - \int_{-\frac{h}{2}}^{\frac{h}{2}} \int_{-\frac{b}{k}}^{\frac{b}{k}} \sigma_{xx} y dy dz \quad (9)$$

where w is the width of the specimen and h is the thickness of the specimen. The bending moment, M , for the three point bending configuration is

$$M = \frac{Px}{2} \quad (10)$$

where P is the applied load and x is the axial distance to the closest lower support.

Substituting Eq. (6) into Eq. (7) gives the following expression for axial stress

$$\sigma_{xx} = \begin{cases} E_T (-ky - b), & -\frac{h}{2} \leq y \leq -\frac{b}{k} \\ E_c (-ky - b), & -\frac{b}{k} \leq y \leq \frac{h}{2} \end{cases} \quad (11)$$

Substituting Eq. (11) into Eq. (8), neglecting any variability of stress through the width of the specimen, and integrating to obtain the following relationship between the tensile and compressive modulus:

$$E_T = \frac{(1+a)^2}{(1-a)^2} E_c, \quad a = \frac{2b}{hk} \quad (12)$$

Further substituting Eq. (11) and (12) into Eq. (9), neglecting any variability of stress through the width of the specimen, and integrating along the thickness to obtain the following approximations for the tensile and compressive Young's moduli

$$E_{T,C} = \frac{M}{k \frac{wh^3}{12} (1 \mp a)^2}, \quad a = \frac{2b}{hk} \quad (13)$$

where $\frac{wh^3}{12}$ is the polar moment of inertia for the rectangular beam cross-section. It is

worth noting that the intercept, b , vanishes if the tensile and compressive modulus are similar and Eq. (13) reduces to

$$E_{T,C} = \frac{M}{k \frac{wh^3}{12}} \quad (14)$$

and the linear axial normal stress distribution (15) matches classical beam theory stress approximation

$$\sigma_{xx} = -\frac{My}{\frac{wh^3}{12}} \quad (15)$$

The maximum shear stress in the area between supports can be derived using the following force equilibrium equation at the cross section equidistant between loading nose and support.

$$\int_{-b/k}^{h/2} \sigma w dy - \int_{-b/k}^{h/2} (\sigma + \partial \sigma) w dy + \tau w dx = 0 \quad (16)$$

which simplifies to

$$\tau = \int_{-b/k}^{h/2} \frac{\partial \sigma}{\partial x} dy \quad (17)$$

From (11) the axial normal stress can be expressed in terms of the linear axial strain distribution multiplied by the Young's modulus. Substitute (13) for the Young's modulus and (10) for the bending moment and take the derivative with respect to x to get

$$\tau_{y=-b/k} \approx \int_{-b/k}^{h/2} \frac{P/2}{\frac{wh^3}{12} k \left(1 + \frac{4b}{hk} + \frac{4b^2}{h^2 k^2} \right)} \times (-ky - b) dy \quad (18)$$

From boundary conditions, the maximum shear stress can be determined to occur at the neutral axis, $y = -b/k$. The maximum shear stress in the beam becomes

$$\tau_{xy}^{\max} \approx \frac{3}{4} \frac{P}{A}, \quad A = wh \quad (19)$$

This expression is the same as the expression developed from classical beam-theory assumptions (3) for the maximum shear stresses in long beams under bending loads. The maximum shear stress approximation (19) is derived based on the observation of a linear axial strain distribution through the thickness of the beam, and not from the classical beam theory kinematic assumptions where the cross section remains rigid and perpendicular to the neutral axis. For materials with the same tensile and compressive modulus values the following distribution through the thickness of the beam [8] is derived, which matches beam theory approximations.

$$\tau_{xy} = \frac{3P}{4A} \left[1 - \left(\frac{2y^*}{h} \right)^2 \right] \quad (20)$$

As the tensile and compressive modulus values are material properties independent of the location, x , and the bending moment is a linear function of x , the curvature, k and the intercept, b are also linear functions of x . The linear axial strain approximation (6) can be generalized as

$$\varepsilon_{xx} = -Kxy - Bx, \quad -\frac{h}{2} \leq y \leq \frac{h}{2} \quad (21)$$

where K and B are constants. Using this observation, a normalized strain can be derived that is not dependent on the x location allowing the distribution to no longer be constrained to a single cross section. Eq. (13) can be rewritten as

$$E_{T,C} = \frac{M_c}{k_c \frac{wh^3}{12} (1 \mp a)^2}, \quad a = \frac{2b_c}{h k_c} \quad (22)$$

where

$$M_c = \frac{Px_c}{2}, \quad k_c = Kx_c = \frac{k}{x} x_c, \quad b_c = Bx_c = \frac{b}{x} x_c \quad (23)$$

and $x_c = L/4$ corresponds to the center cross-section location. The constants k_c and b_c are measured as the slope and the intercept of the normalized axial strain distribution, $\varepsilon_{xx} x_c / x$, throughout the thickness of the SBS specimen away from the supports and loading nose.

The closed form solution, Eq. (13), was developed assuming transverse normal stresses to be negligible in the area of measurement. However, this is not necessarily true for short beams. It is important to determine how any non-zero transverse stress

impacts our closed form solution, in order to determine if the solution needs to be more accurate. In the absence of transverse normal stress, σ_{yy} , on the lateral surfaces of the SBS coupons, transverse longitudinal strain is related to the axial strain through the following expression

$$\varepsilon_{yy} = -\nu_{xy} \varepsilon_{xx} \quad (24)$$

where ν_{xy} is the Poisson's Ratio. However, if σ_{yy} is not zero, Eq. (24) can be changed to

$$\varepsilon_{yy} = -\nu_{xy} \varepsilon_{xx} + \varepsilon_{rr} \quad (25)$$

where the ε_{rr} term represents an error in the transverse longitudinal strain resulting from a nonzero transverse normal stress, σ_{yy} . This term is then normalized with respect to the axial strain.

$$error = \frac{\varepsilon_{yy}}{\varepsilon_{xx}} + \nu_{xy} \quad (26)$$

A typical *error* distribution through the thickness of a specimen can be seen in Figure 3-11.

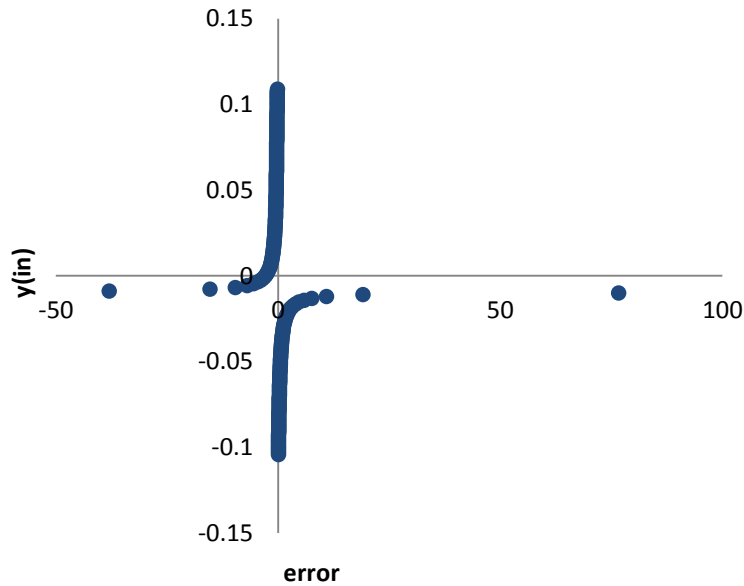


Figure 3-11 Typical transverse normal stress-strain error term through the thickness of a carbon/epoxy SBS specimen at 70% failure load

A FEM based stress analysis shows that such *error* distribution follows the same trend as the ratio of the transverse normal stress, σ_{yy} , to the axial normal stress, σ_{xx} , through the thickness of the beam in the same region. However, based on FEM stress results the transverse normal stress still remains quite small in comparison to the axial normal stress; e.g. reaching a peak of .5% of the axial normal stress for carbon/epoxy in the center of the specimen, when using a s/t ratio of 4.8. Still it is important to determine whether the stress can be neglected in the axial modulus formulation. When transverse normal stresses are nonzero the simplified one-dimensional Hooke's law no longer applies to this problem and the axial normal stress becomes

$$\sigma_{xx} = \begin{cases} E_T \varepsilon_{xx} \left(1 + \frac{v_{yx} \text{error}}{1 - v_{xy} v_{yx}} \right), & -\frac{h}{2} \leq y \leq -\frac{b}{k} \\ E_c \varepsilon_{xx} \left(1 + \frac{v_{yx} \text{error}}{1 - v_{xy} v_{yx}} \right), & -\frac{b}{k} \leq y \leq \frac{h}{2} \end{cases} \quad (27)$$

where an additional term $E_{T,C} \varepsilon_{xx} \frac{v_{yx} \text{error}}{1 - v_{xy} v_{yx}}$ is added to the one-dimensional Hooke's law equation. Since $v_{yx} v_{xy}$ is much less than one for polymer-matrix composites in the (1-3) and (1-2) principal material planes, including unidirectional carbon/epoxy and glass/epoxy, this term reduces to $E_{T,C} \varepsilon_{xx} v_{yx} \text{error}$. Here we can see the *error* multiplied by the out-of-plane Poisson's Ratio, $v_{yx} \times \text{error}$, is approximately equal to the percentage increase of the axial stress approximation to the one dimensional solution at each location, y , along the thickness. For SBS specimens, in the region equidistant between support and loading nose, the value $v_{yx} \times \text{error}$ only reaches values above 5% in the regions of very small axial strains, close to the neutral axis. When substituting Eq. (27) for the axial stress into Eq. (8), used to derive the tensile and compressive axial moduli, the additional terms have little influence on the resulting solution for both the tensile and compressive axial moduli. In particular, when using the non-zero transverse normal stress solution to measure the tensile and compressive moduli for the SBS tests run at a s/t ratio equal to 4.8, the results vary less than 1% from the values obtained from Eq. (13). Increasing the span to thickness ratio was found to reduce the difference even further, which can be explained by the reduced transverse normal stresses along the gage region.

3.3 Experimental Results for S2-Glass/E773-Epoxy Composites

To demonstrate the assessment of three dimensional stress strain relations a set of fifteen S2-glass/E773-epoxy SBS specimens were machined from a 26-ply .24 in. (6.1 mm) thick unidirectional composite panel. Ten specimens were machined in the fiber (0°) direction and five specimens were machined from the (90°) material direction. The specimen geometry included an average specimen length of 1.75 in. (44.5 mm) and width of .25 in (6.4 mm). A support span of 1.2 in (30.5 mm) was used for each specimen resulting in a span to thickness ratio of 5. Each test was run using a .5 in. (12.7 mm) loading nose diameter. All tests were performed under room temperature ambient conditions.

Specimens S1-S5, machined in the fiber direction, were statically loaded in the 1-3 principal material plane; specimens S6-S10, also machined in the fiber direction, were statically loaded in the 1-2 principal material plane; and specimens S11-S15, machined in the 90° plane, were statically loaded in the 2-3 principal material plane. All specimens were tested using a loading rate of 1.27 mm/min (.05 in/min). Full field surface strain components were obtained for each specimen in the plane of loading using a DIC 16 MP stereo camera system combined with Vic3D software analysis [29]. Each specimen was analyzed using a subset window size of 45x45 pixels, corresponding to an approximate area of .0007 in² (.44 mm²) for SBS specimens. Displacement vectors were analyzed on 9 pixel centers, resulting in roughly 11,000 data points for SBS tests. The displacement measurements were then numerically differentiated over a local neighborhood using a 15x15 array of points applied to a strain algorithm in VIC-3D software in order to compute the Lagrange strain tensor [29]. Images were obtained during the loading sequence at a 1 Hz frequency along with simultaneous load data which is supplied by the hydraulic testing machine.

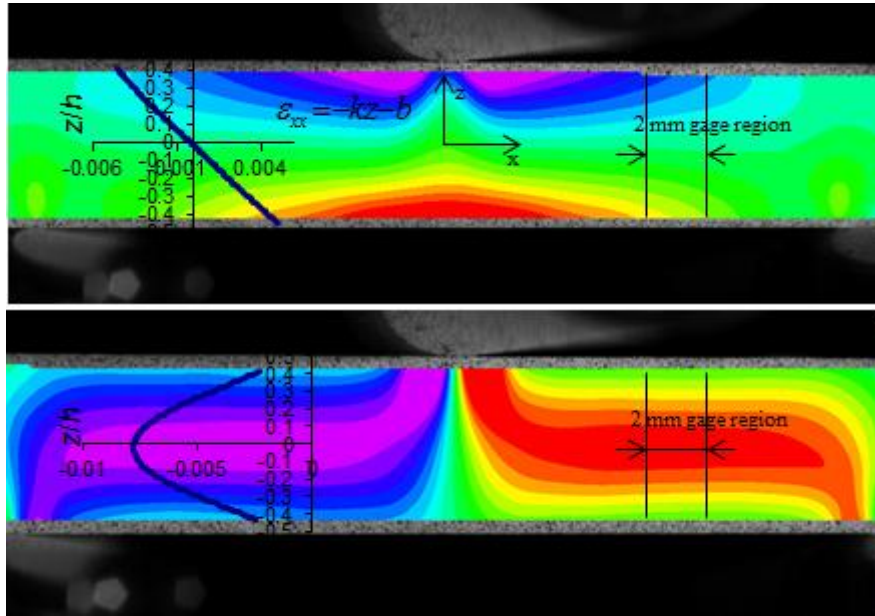


Figure 3-12 Axial normal and interlaminar shear strain distribution extracted from DIC in the center region between loading nose and support

Data is extracted from a .079 in. (2 mm) gage region centered between the loading nose and lower support, as shown in Figure 3-12, on both the left and right side of each specimen. An example of a typical axial normal and interlaminar shear strain distribution extracted from this region can be seen in Figure 3-12. Deformation measurements obtained from these gage regions confirm (a) close to linear axial strain distributions through the SBS specimen thickness far from the loading nose and support locations; and (b) linear axial stress-strain response till failure. Figure 3-13 illustrates the typical axial strain distributions of three specimens loaded in the 1-2, 1-3, and 2-3 material plane. The transverse coordinate, y , is normalized with respect to the thickness, h , in the plane of loading.

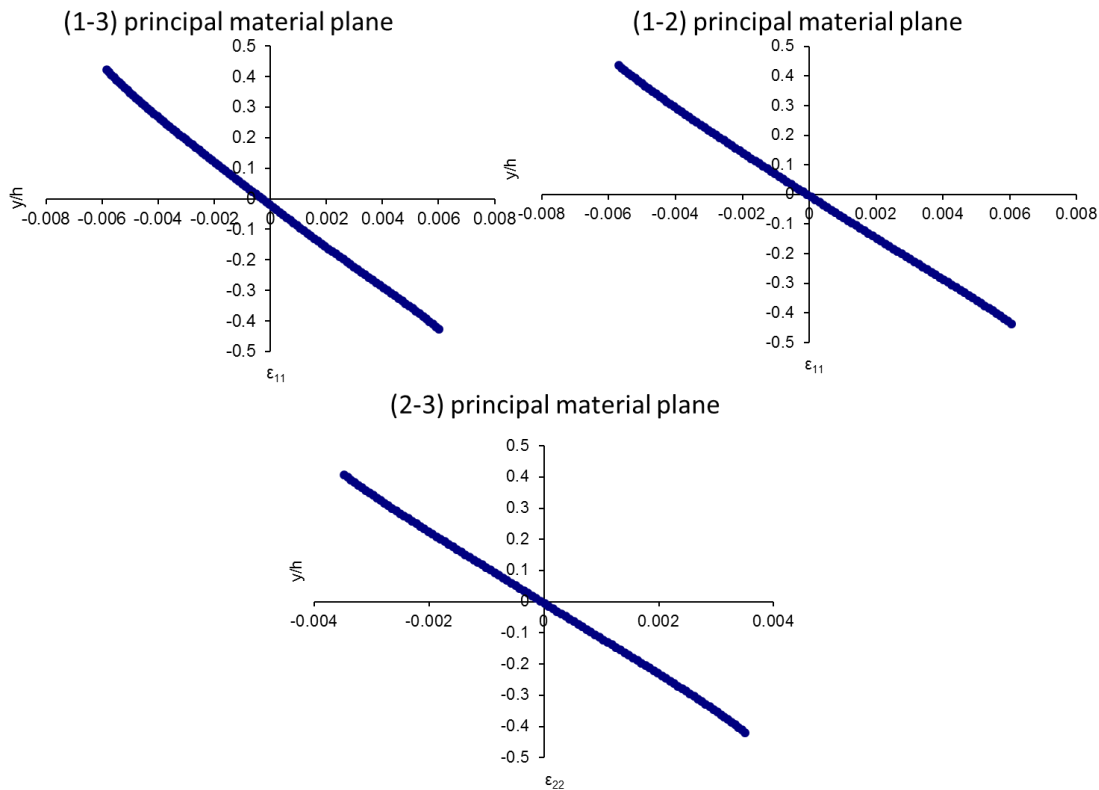


Figure 3-13 Typical through the thickness axial strain distribution for S2-glass/E73-epoxy SBS specimens loaded in the (1-3), (1-2), and (2-3) material planes at close to failure load

Average maximum shear strains through the 2 mm gauge region were used to assess the shear stress-strain behavior of each specimen. The Ramberg-Osgood equation (4) was used to characterize the nonlinear shear stress strain behavior in both the (1-3) and (1-2) principal material planes using a least squares approximation. The linear shear modulus, G_{ij} , is determined by taking the slope of the linear portion of the shear stress-strain curve. For each of the tests in this study the slope is taken at strain values between 1,000 and 6,000 $\mu\epsilon$. The shear stress was approximated using Eq. (19). The measured results for the linear shear modulus, G_{ij} , the secant-intercept modulus, K_{ij} ,

and the exponent n_{ij} used in Eq. (4) are listed in Table 3-1 and Table 3-2. The sample average and coefficient of variation are listed for each measurement. The shear stress strain curves for each specimen tested in the 1-3 and 1-2 material plane are shown in Figure 3-14 and Figure 3-15 along with a trend line based on the average shear parameters. For shear strains, γ_{13} and γ_{12} , higher than 1% the SBS specimens exhibited highly nonlinear shear behavior.

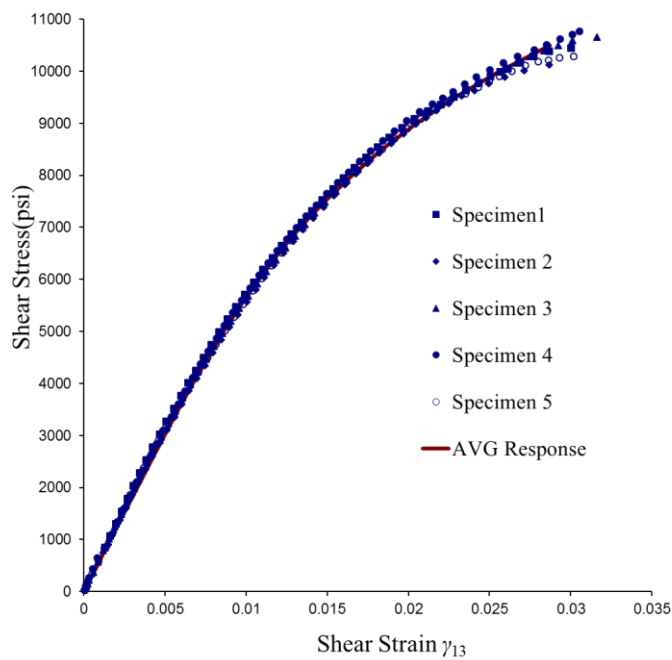


Figure 3-14 Interlaminar (1-3 material plane) shear stress-strain response for unidirectional S2-glass/E773-epoxy tape

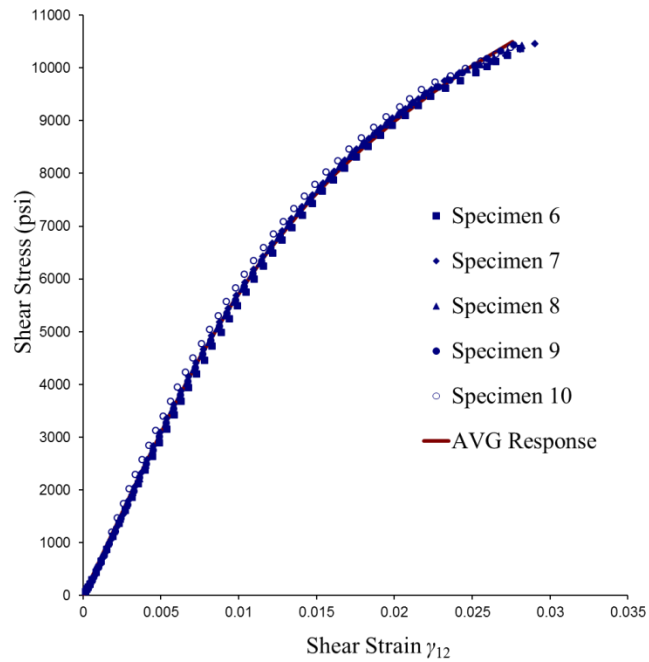


Figure 3-15 In-plane (1-2 material plane) shear stress-strain response for unidirectional S2-glass/E773-epoxy tape

Tensile failure for the 90° SBS specimens loaded in the (2-3) material plane occurred at shear strains, γ_{23} , between 2,000 and 3,000 $\mu\epsilon$ preventing any shear nonlinearity from being captured in this material plane. Therefore, only the linear shear modulus could be measured in the (2-3) plane using the SBS test method. Table 3-3 lists the (2-3) plane shear modulus values. Also, compressive damage under the loading nose was observed for specimens tested in the (1-2) principal material plane before ultimate delamination failure. To reduce the stress concentrations introduced by the loading nose and supports it is suggested to increase the loading nose diameter to 2 in. (50.8 mm) for glass/epoxy composite materials tested in the (1-2) and (1-3) material planes. Shear failure has consistently been observed for several glass/epoxy composite systems using a 2 in. (50.8 mm) loading nose diameter in both the (1-2) and (1-3)

principal material planes. The material parameters generated using the 2 in. (50.8 mm) diameter loading nose were consistent with the values listed in Table 3-1.

The average axial modulus, E_{11} , tensile axial modulus E_{11T} , and compressive axial modulus, E_{11C} , are also listed in Table 3-1 and Table 3-2. They are obtained using the developed closed form axial modulus solution Eq. (13) and Eq. (14). The average in-plane modulus, E_{22} , obtained using (14) is listed in Table 3-3. In addition, the Poisson's ratio, ν_{xy} , was measured for each plane of loading and is listed in the following tables.

The Poisson's ratios are approximations based on the axial and transverse strains obtained from the top and bottom surfaces of the center cross-section. It is worth noting that the constitutive parameters listed in Table 3-1, Table 3-2, and Table 3-3 are the average between the values measured from both the left and right gage sections of the specimen.

Table 3-1 S2-glass/381-epoxy Material Constitutive Properties Generated for the Interlaminar (1-3) Material Plane

Specimen	t mm (in)	w mm (in)	G_{13} GPa (msi)	K_{13} MPa (ksi)	n_{13}	E_{11T} Gpa (msi)	E_{11C} Gpa (msi)	E_{11} Gpa (msi)	ν_{13}	S_{13} MPa (ksi)
1	6.20 (.244)	6.30 (.248)	4.23 (.614)	194 (28.1)	.223	45.9 (6.66)	45.5 (6.60)	45.7 (6.62)	.28	71.7 (10.4)
2	6.08 (.2395)	6.32 (.249)	4.11 (.596)	191 (27.6)	.219	47.9 (6.95)	47.9 (6.94)	47.8 (6.94)	.26	69.9 (10.1)
3	6.11 (.2405)	6.30 (.248)	4.09 (.594)	192 (27.9)	.218	47.2 (6.85)	46.7 (6.77)	46.2 (6.70)	.26	73.1 (10.6)
4	6.07 (.239)	6.30 (.248)	4.23 (.613)	186 (27.0)	.212	46.2 (6.70)	46.8 (6.79)	47.4 (6.88)	.27	73.8 (10.7)
5	6.12 (.241)	6.30 (.248)	4.15 (.602)	192 (27.8)	.222	50.5 (7.32)	48.2 (6.99)	46.1 (6.69)	.27	71.0 (10.3)
AVG	6.11 (.2408)	6.30 (.248)	4.16 (.604)	191 (27.7)	.219	47.6 (69.0)	47.0 (6.82)	46.6 (6.76)	.27	71.7 (10.4)
COV	.81%	.17%	1.6%	1.5%	1.9%	3.8%	2.2%	2.1%	2.9%	2.3%

Table 3-2 S2-glass/381-epoxy Material Constitutive Properties Generated for the in-plane

(1-2) Material Plane

Specimen	t mm (in)	w mm (in)	G_{12} GPa (msi)	K_{12} MPa (ksi)	n_{12}	E_{11} Gpa (msi)	ν_{12}
6	6.30 (.248)	6.10 (.24)	4.07 (.590)	204 (29.6)	.230	48.1 (6.98)	.28
7	6.30 (.248)	6.11 (.241)	4.36 (.633)	218 (31.6)	.247	47.8 (6.94)	.28
8	6.30 (.248)	6.22 (.245)	4.14 (.600)	216 (31.3)	.239	47.6 (6.90)	.29
9	6.30 (.248)	6.10 (.24)	4.33 (.629)	223 (32.3)	.250	48.2 (6.99)	.30
10	6.35 (.250)	6.07 (.239)	4.35 (.631)	196 (28.5)	.221	47.8 (6.94)	.28
AVG	6.30 (.248)	6.12 (.241)	4.25 (.617)	211 (30.7)	.237	49.1 (6.95)	.29
COV	.81%	.17%	3.22%	5.1%	5.0%	.56%	3.1%

Table 3-3 S2-glass/E773-epoxy Material Constitutive Properties Generated for the (2-3)

Material Plane from 90° Specimens

Specimen	t mm (in)	w mm (in)	G_{23} GPa (msi)	E_{22} Gpa (msi)	ν_{23}
11	6.10 (.24)	6.29 (.2475)	4.47 (.648)	12.6 (1.83)	.42
12	6.10 (.24)	6.29 (.2475)	4.54 (.658)	12.6 (1.82)	.40
13	6.10 (.24)	6.29 (.2475)	4.52 (.655)	12.6 (1.83)	.42
14	6.10 (.24)	6.30 (.248)	4.43 (.643)	12.7 (1.84)	.41
15	6.10 (.240)	6.30 (.248)	4.41 (.640)	12.3 (1.78)	.40
AVG	6.10 (.240)	6.30 (.248)	4.47 (.649)	12.8 (1.82)	.41
COV	0%	.11%	2.3%	1.29%	2.6%

Similar values for both the tensile and compressive axial modulus makes the average axial modulus a good approximation for the axial behavior of the beam. Consistent measurements in the (1-2) material plane further verify these measurements. The in-plane (1-2) shear stress-strain response is similar to the interlaminar (1-3) shear stress-strain response. In addition the (2-3) plane shear modulus is close to a transverse isotropic material approximation.

$$G_{23} \approx \frac{E_{22}}{2(1+\nu_{23})} = 4.4GPa \quad (28)$$

This is important, since the transverse isotropy observation could reduce the number of tests required to characterize the material [34]. However, it is important to note that the interlaminar shear strength is lower than the in-plane shear strength for this material. Figure 3-16 compares the simple closed-form shear stress approximation with the shear stress distribution predicted from 3D FEM based stresses in the region equidistant from support and loading nose for an S2-glass/E773-epoxy SBS specimen loaded in the material (1-3) plane at a close to failure load.

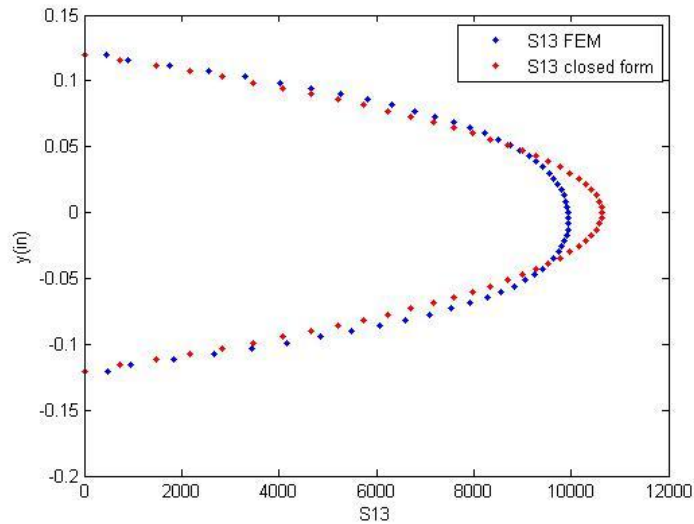


Figure 3-16 Closed Form and FEM comparison of Interlaminar (1-3) shear stress distribution for S2-glass/E773-epoxy unidirectional SBS specimen at close to failure load

The maximum shear stress before failure predicted by closed form solution (20) is 6% higher than FEM based maximum shear stress. To more accurately predict the shear strength of the material, a stress model similar to Eq. (5) can be used. This model is expanded later in this work to account for varying span to thickness ratios of the SBS test setup. Simple shear stress approximations (19) can be used to reasonably assess the shear material parameters (G_{13} , K_{13} , n_{13}) for glass/epoxy unidirectional specimens since the error reaches a maximum around 6%, and remains within 5% of FEM predictions for the majority of the loading phase. Figure 3-17 compares the FEM axial stress predictions with the axial stresses determined from DIC measurements and axial modulus measurements.

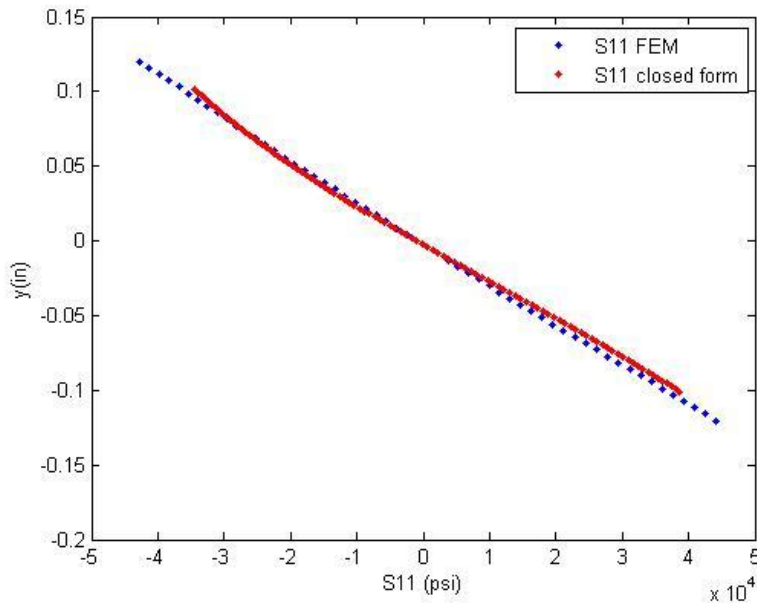


Figure 3-17 Closed Form and FEM comparison of axial normal stress distribution for S2-glass/E773-epoxy unidirectional SBS specimen at close to failure load

3.4 Experimental Results for E-Glass/5216-Epoxy Composites

To demonstrate the applicability of the SBS test method in measuring the interlaminar shear stress-strain response for glass/epoxy material systems a set of five 30-ply unidirectional E-glass/5216-epoxy composite tape SBS specimens were machined in the 0° and statically loaded using a servo-hydraulic testing machine at a loading rate of 1.27 mm/min (.05 in/min) in the (1-3) material direction until failure. Specimen dimensions include a 38 mm (1.5 in.) length, 6 mm (.24 in.) thickness, and 4.4 mm (.17 in.) width. A support length of 25.4 mm (1 in.) was used for all tests resulting in a span to thickness (s/t) ratio of 4. Interlaminar shear failure was observed for all five specimens, where the delamination started in the center region between supports and propagated to the edge. Full field surface strain calculations were obtained from the plane of loading

using a DIC 16 MP stereo camera system combined with Vic3D software analysis. Images were taken at a 1 Hz frequency and analyzed using a subset window size of 21x21 pixels, corresponding to an approximate area of .0004 in² (.25 mm²) for SBS specimens. Displacement vectors were analyzed on 4 pixel centers, resulting in roughly 20,000 data points for each specimen. The displacement measurements were then numerically differentiated over a local neighborhood using a 15x15 array of points applied to a strain algorithm in VIC-3D software in order to compute the Lagrange strain tensor [30]. An observed linear axial strain distribution, through the thickness of the specimen in the center between support and loading nose, till failure allowed the use of simple closed form solution (19) for the maximum shear stress approximation in the beam. Figure 3-18 shows the shear stress-strain response measured for each specimen using Eq. (19) for shear stress calculations. Nonlinear shear stress-strain behavior was observed above 1% shear strain. The Ramberg-Osgood equation (4) was used to characterize the nonlinear shear stress-strain behavior using a least squares approximation. Table 3-4 lists the linear shear modulus, G_{13} , secant-intercept modulus, K_{13} , and exponent, n_{13} , associated with the Ramberg-Osgood equation (4) as well as the interlaminar shear strength, S_{13} . The ultimate shear strength measurement in Table 3-4 is based on simple shear stress approximation Eq. (19) at the failure load.

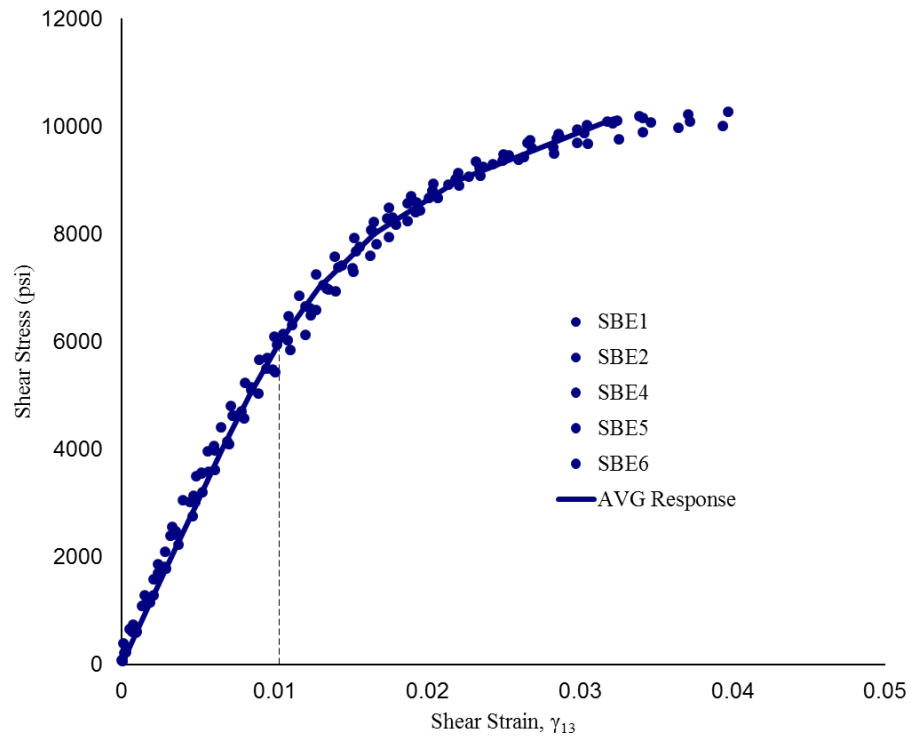


Figure 3-18 Interlaminar (1-3 material plane) shear stress-strain response for E-glass/5216-epoxy unidirectional tape

Table 3-4 E-glass/5216-epoxy Material Constitutive Properties Generated for the (1-3)

Material Plane

Specimen	t mm (in)	w mm (in)	G_{13} GPa (msi)	K_{13} GPa (ksi)	n_{13}	S_{13} MPa (ksi)
SBE 1	5.99 (.236)	4.43 (.1745)	4.51 (.654)	.128 (18.6)	.15	71.7 (10.4)
SBE 2	6.02 (.237)	4.39 (.173)	4.16 (.603)	.128 (18.6)	.15	71.5 (10.4)
SBE 4	6.01 (.2365)	4.38 (.1725)	4.10 (.595)	.143 (20.7)	.17	67.1 (9.7)
SBE 5	6.05 (.238)	4.41 (.1735)	4.04 (.585)	.141 (20.5)	.17	69.1 (10.0)
SBE 6	5.98 (.2355)	4.41 (.1735)	4.29 (.622)	.131 (19.0)	.15	70.0 (10.2)
AVG	6.01 (.2367)	4.41 (.1738)	4.22 (.612)	.134 (19.5)	.16	69.9 (10.1)
COV	.37%	.72%	4.4%	5.4%	7.4%	2.7%

3.5 Experimental Results for IM7-Carbon/8552-Epoxy Composites

The tensile modulus values for glass/epoxy material are similar to the compressive modulus values in the corresponding direction. Higher difference is expected for carbon/epoxy material systems as a result of the anisotropic nature of carbon fibers [34]. To demonstrate the application of three dimensional characterization, using the SBS test method for carbon/epoxy unidirectional composites, a set of fourteen SBS IM7-carbon/8552-epoxy specimens were machined in the zero-degree and 90-degree directions and loaded in the three principal material planes. Each specimen was cut from a 34-ply .25 in. (6.35 mm) thick panel and machined at a 1.75 in. (44.5 mm) length and .25 in (6.35 mm) width. It should be noted that the same panel was not used

for all of the following tests. The support length is 30.5 mm (1.2 in.) resulting in a 4.8 s/t ratio. The loading nose diameter is increased from the ASTM standard of .25 in. (6.4 mm) to 4 in. (101.6 mm), in order to eliminate compressive damage under the loading nose resulting in undesired failure modes, for specimens tested in both the (1-2) and (1-3) principal material planes. It should be noted that a 2 in. diameter loading nose was used for glass/epoxy composites tested in the (1-2) and (1-3) principal material planes. The larger interlaminar shear strength of carbon/epoxy composites requires a larger loading nose diameter in order to ensure the shear delamination. A standard lower support diameter of .125 in. (3.2 mm) is used throughout this study. Full field surface strain calculations were obtained from the plane of loading using a DIC 16 MP stereo camera system combined with Vic3D software analysis. Each specimen was analyzed using a subset window size of 35x35 pixels, corresponding to an approximate area of .0006 in² (.39 mm²) for SBS specimens. Displacement vectors were analyzed on 7 pixel centers, resulting in roughly 14,000 data points for SBS tests. The displacement measurements were then numerically differentiated over a local neighborhood using a 15x15 array of points applied to a strain algorithm in VIC-3D software in order to compute the Lagrange strain tensor [29]. Table 3-5 lists the nonlinear shear properties as well as the average tensile and compressive axial modulus values. A close to linear axial strain distribution till failure allows the use of Eq. (19) for the maximum shear stress approximation. Figure 3-19 illustrates the typical axial strain distributions of three specimens loaded in the 1-2, 1-3, and 2-3 material plane. The transverse coordinate, y , is normalized with respect to the thickness, h , in the plane of loading.

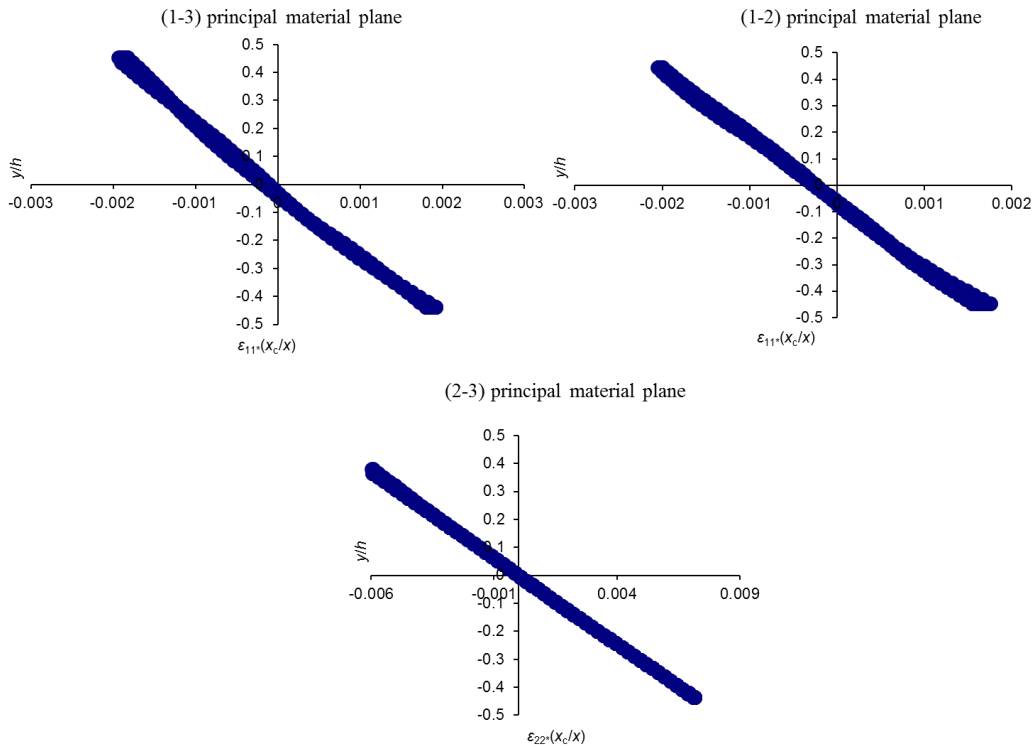


Figure 3-19 Typical through the thickness normalized axial strain distributions for IM7-carbon/8552-epoxy SBS specimens loaded in the (1-3), (1-2), and (2-3) material planes

Figure 3-20 and Figure 3-21 show the nonlinear shear stress-strain curves for the IM7-carbon/8552 SBS specimens, 19-23 and 40-43, loaded in the (1-3) and (1-2) material plane using Eq. (20) for the maximum shear stress approximation. Similar to glass/epoxy specimens nonlinear shear behavior is observed as γ_{13} and γ_{12} reach above 1%. The Ramberg-Osgood equation (4) is used to fit the nonlinear shear stress-strain data using a least squares approximation for specimens tested in both the (1-2) and (1-3) material planes. Nonlinear shear stress-strain behavior is not observed in the (2-3) material plane due to tensile failure of the specimen at low loads where γ_{23} is still less than 1%. In addition the higher nonlinear shear strength of carbon/epoxy composites

prevent the in-plane shear strength from being measured in this experiment due to compression damage under the loading nose before shear failure initiation.

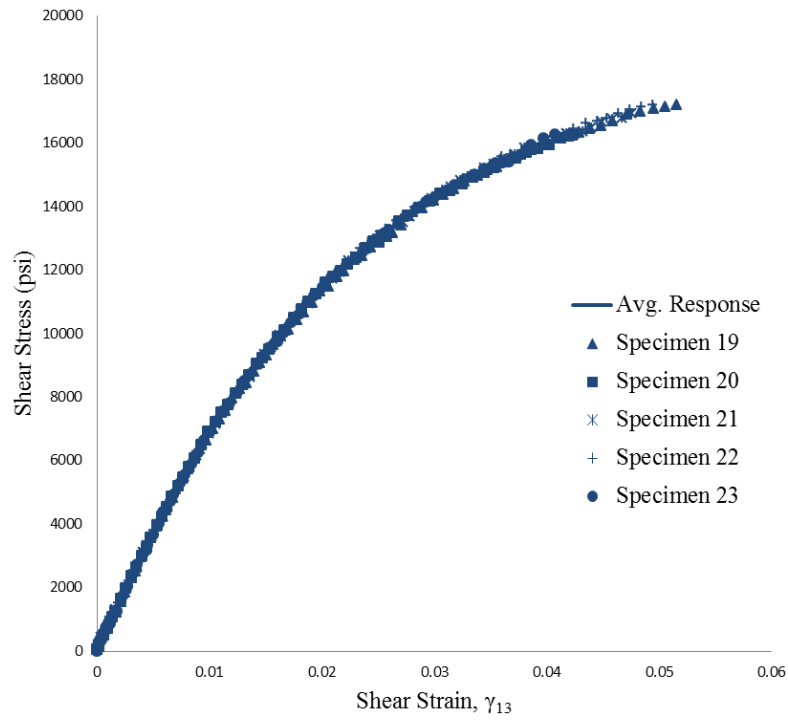


Figure 3-20 Interlaminar (1-3 material plane) shear stress-strain response for IM7-carbon/8552-epoxy unidirectional tape

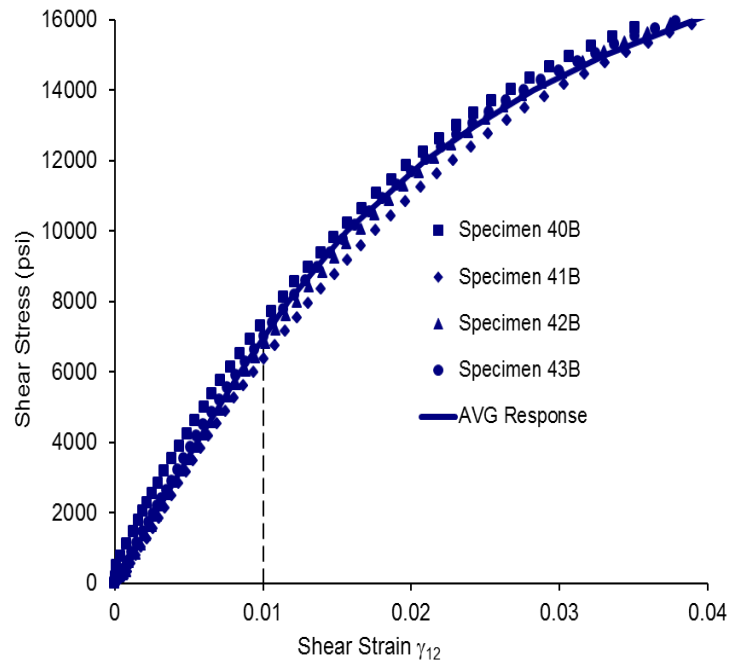


Figure 3-21 In-plane (1-2 material plane) shear stress-strain response for IM7-carbon/8552-epoxy unidirectional tape

Table 3-5 IM7-carbon/8552-epoxy Material Constitutive Properties Generated for the (1-3) Material Plane.

Specimen	t mm (in)	w mm (in)	G_{13} GPa (ksi)	K_{13} MPa (ksi)	n_{13}	E_{11T} Gpa (msi)	E_{11C} Gpa (msi)	E_{11} Gpa (msi)	ν_{13}	S_{13} MPa (ksi)
19	6.15 (.242)	6.34 (.2495)	5.07 (735)	270 (39.2)	.223	164 (23.8)	142 (20.6)	152 (22.1)	.34	109 (15.8)
20	6.17 (.243)	6.34 (.2495)	5.01 (726)	277 (40.2)	.227	167 (24.2)	141 (20.4)	153 (22.2)	.29	110 (15.9)
21	6.12 (.241)	6.34 (.2495)	4.83 (701)	268 (38.8)	.223	164 (23.7)	137 (19.8)	148 (21.5)	.32	108 (15.6)
22	6.12 (.241)	6.32 (.249)	4.87 (706)	253 (36.7)	.208	159 (23.1)	137 (19.8)	148 (21.4)	.35	110 (16.0)
23	6.13 (.2415)	6.34 (.2495)	4.98 (723)	306 (44.4)	.253	164 (23.8)	134 (19.5)	148 (21.4)	.33	110 (15.9)
AVG	6.15 (.242)	6.34 (.2495)	4.95 (718)	275 (39.9)	.227	163 (23.7)	138 (20.0)	150 (21.7)	.34	110 (15.9)
COV	.35%	.09%	2%	7%	7%	2%	2%	2%	6%	1%

Table 3-6 IM7-carbon/8552-epoxy Material Constitutive Properties Generated for the
(1-2) Material Plane

Specimen	t mm (in)	w mm (in)	G_{12} GPa (ksi)	K_{12} MPa (ksi)	η_{12}	E_{11} GPa (msi)	ν_{12}
40B	6.52 (.2565)	6.34 (.2495)	5.08 (737)	269 (39)	.22	145 (21.1)	.30
41B	6.52 (.2565)	6.34 (.25)	4.72 (685)	255 (37)	.21	152 (22.0)	.34
42B	6.53 (.257)	6.34 (.25)	4.98 (723)	262 (38)	.21	143 (20.8)	.28
43B	6.54 (.2575)	6.32 (.2505)	5.21 (756)	276 (40)	.22	143 (20.8)	.32
AVG	6.53 (.257)	6.34 (.25)	5.01 (726)	262 (38)	.21	146 (21.2)	.31
COV	.2%	.2%	2%	3%	3%	2%	8%

Table 3-7 IM7-carbon/8552-epoxy Material Constitutive Properties Generated for the
(2-3) Material Plane

Specimen	t mm (in)	w mm (in)	G_{23} GPa (ksi)	E_{22T} Gpa (msi)	E_{22C} Gpa (msi)	E_{22} Gpa (msi)	ν_{23}
4	6.86 (.27)	6.45 (.254)	2.81 (407)	8.83 (1.28)	9.17 (1.33)	8.89 (1.29)	.49
5	6.90 (.2715)	6.41 (.2525)	2.81 (408)	8.69 (1.26)	9.31 (1.35)	8.96 (1.30)	.50
6	6.90 (.2715)	6.44 (.2535)	2.80 (406)	8.48 (1.23)	8.83 (1.28)	8.62 (1.25)	.51
7	6.90 (.2715)	6.41 (.2525)	2.85 (414)	8.76 (1.27)	8.83 (1.28)	8.83 (1.28)	.47
8	6.83 (.269)	6.44 (.2535)	2.88 (417)	8.69 (1.26)	8.76 (1.27)	8.69 (1.26)	.49
AVG	6.88 (.2707)	6.43 (.2532)	2.83 (410)	8.69 (1.26)	8.96 (1.30)	8.83 (1.28)	.49
COV	.4%	.3%	2%	2%	3%	2%	3%

Similar to S2-glass/E773-epoxy measurements, the in-plane (1-2) shear stress-strain response is similar to the interlaminar (1-3) shear stress-strain response for IM7-carbon/8552-epoxy. In addition the (2-3) plane shear modulus is close to a transverse isotropic material approximation.

$$G_{23} \approx \frac{E_{22}}{2(1 + \nu_{23})} = 2.9GPa \quad (29)$$

Results from these tests confirm that the transverse isotropy assumption is a good approximation for the material properties of IM7-carbon/8552-epoxy unidirectional composite tape, especially in the linear elastic regime. However, a higher shear strength of unidirectional IM7-carbon/8552-epoxy is observed in the (1-2) principal material plane versus the (1-3) principal material plane. Therefore, it is important to measure these properties independently, especially when these values are used as part of the failure criteria in failure prediction models. In particular, the interlaminar shear strength is necessary for accurate failure prediction models of thick panel composites structures, such as rotor blades. FEM based stresses using material properties generated for IM7-carbon/8552-epoxy are compared with closed form shear stress approximations. Accurate nonlinear shear stresses are obtained using an iterative procedure previously discussed and outlined in Ref. [10, 23]. A comparison of FEM based maximum shear stress and simple closed form maximum shear stress approximation (20) for both unidirectional S2-glass/E773-epoxy SBS specimens and IM7-carbon/8552-epoxy SBS specimens, in the region midway between the loading nose and supports shown in Figure 3-22.

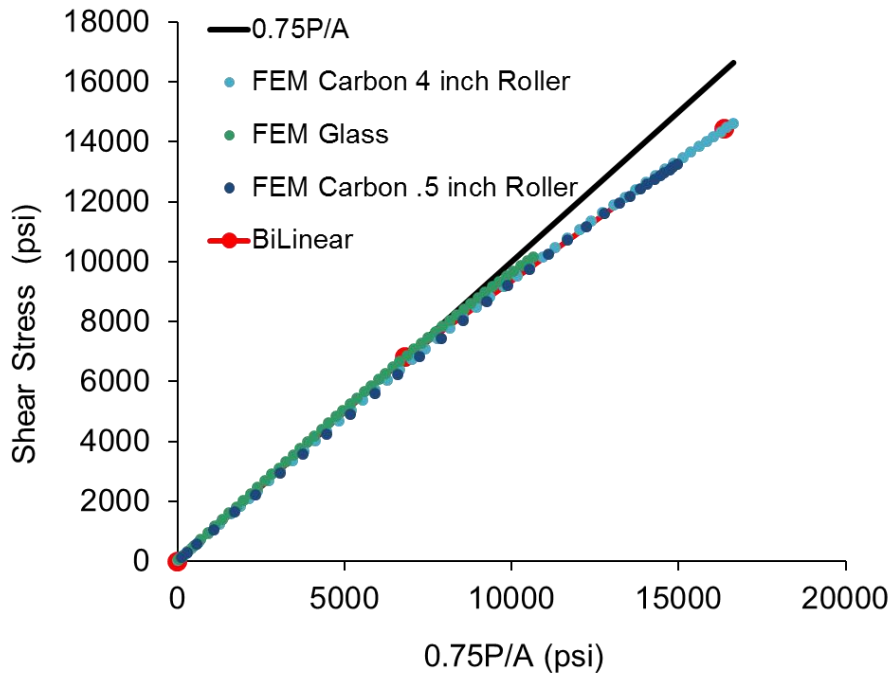


Figure 3-22 Comparison of FEM results and closed form (20) stress approximations for S2-glass/E773-epoxy and IM7-carbon/8552-epoxy SBS coupons

Figure 3-22 shows that each of the stress results are in close agreement at small loads which correspond to the linear-elastic region. This is counterintuitive since elasticity equations depend on the constitutive properties of the anisotropic materials even for stress-bound problems [35]. It is also observed that both glass/epoxy and carbon/epoxy exhibit similar shear stress behavior throughout loading, even though there is a large difference between the ratios of the Young's Modulus in the fiber direction and the transverse direction for each material. The larger discrepancy between the maximum shear stress predicted by FEM and the closed form approximation (19) for IM7-carbon/8552-epoxy SBS specimens close to failure loads compared with S2-glass/E773-epoxy SBS specimens can be attributed to the higher shear strength of carbon/epoxy which causes the specimen to fail further into the nonlinear regime, where the

discrepancy between FEM and the closed form solution (19) is more pronounced. These results indicate that the maximum shear stresses in the SBS specimens do not have a strong material dependency, and can therefore be well approximated using a geometric (material independent) stress approximation.

Figure 3-23 shows a comparison of the FEM based shear stress distribution and simple closed form shear stress distribution (20) in the center between the support and loading nose for an IM7-carbon-8552-epoxy SBS specimen at a 4.8 s/t ratio close to failure load. This demonstrates the larger discrepancy between FEM and the closed form solution (19) when reaching further into the nonlinear shear regime right before failure.

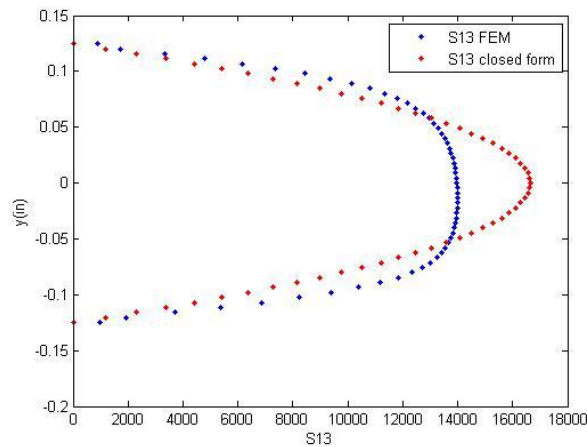


Figure 3-23 Through the thickness interlaminar (1-3) shear stress distribution comparison for IM7-carbon/8552-epoxy unidirectional SBS specimen at close to failure load

A 17% difference is observed between the maximum shear stress approximated using (20) and FEM based maximum shear stress at close to failure loads. Based on these results it is clear that Eq. (20) is not a good approximation of the maximum shear stress in the beam for carbon/epoxy specimens in the nonlinear shear regime. The application of this equation to SBS specimens has been addressed in several studies. As previously discussed Eq. (6) was developed in Reference [19] as a more accurate

stress model prediction for the maximum shear stress of SBS specimens. Using this model the maximum shear stress is within 5% of FEM predictions. The model does not change the linear shear modulus measurements but will affect the nonlinear shear parameters. The updated nonlinear parameters for both the SBS specimens in the (1-3) and (1-2) plane are listed in Table 3-8.

Table 3-8 Updated shear properties for IM7-carbon/8552-epoxy unidirectional composite tape using the bilinear model from Ref. [19]

Plane		K_{ij} (ksi)	n_{ij}	S_{ij} (ksi)
(1-3)	AVG (COV)	33.2 (3.7%)	.219 (3.2%)	14.1 (.86%)
(1-2)	AVG (COV)	30.9 (5.1%)	.197 (6.3%)	N/A

The bilinear model developed in Ref. [19] predicts an 11% decrease in shear strength from the closed form prediction for the SBS IM7-carbon/8552-epoxy unidirectional SBS specimens tested in the (1-3) material plane. The deviation of the stresses from closed form beam theory approximations is a result of the nonlinear shear behavior as well as the short span to thickness ratio of the SBS specimen design [10, 15, 16, 19]. For small span to thickness ratios the classical beam theory approximation (4) becomes invalid [15]. The model in Ref. [19] does not account for varying s/t ratios which will change the apparent maximum shear stress of the beam in the nonlinear regime [15]. One way to further reduce the transverse stresses in the region between loading nose and support is to increase the span to thickness (s/t) ratio of the short beam. By running a series of SBS tests at different s/t ratios the effect of the lower transverse stresses in this region on the accuracy of the stress approximation (19) can be determined. This is accomplished in the following study where IM7-carbon/8552-epoxy SBS tests were run

with varying span to thickness (s/t) ratios to determine this effect and expand the stress model developed in Ref. [19]. SBS tests were performed for six different s/t ratios. A sample size of five IM7-carbon/8552-epoxy unidirectional tape SBS specimens were tested at each of the following spans: 1.2 in. (30.5 mm), 1.3 in. (33 mm), 1.5 in. (38.1 mm), 1.75 in. (44.5 mm), 2 in. (50.8 mm), and 2.5 in. (63.5 mm). Each specimen was cut from a 35-ply resulting in a .25 in. (6.4 mm) thickness, and .25 in. (6.4 mm) width. Three separate panels were used for these tests. The SBS specimens of the first three spans were cut from the same panel while the specimens with the last three spans were cut from a combination of two additional panels. Each specimen was statically loaded in the interlaminar (1-3) material plane, under 72° room temperature ambient conditions.

The span between lower supports, s , varies from a 1.2 in. (30.5 mm) to 2.5 in. (63.5 mm), resulting in the following s/t ratios: 4.8, 5.2, 6, 7, 8, and 10. Each specimen was machined with a square cross section of .25 in. (6.3 mm) width and thickness. A 4 in. (101.6 mm) loading nose diameter is used, consistent with previous tests for carbon/epoxy composites. Symmetry of the test configuration was ensured using an alignment device developed in this work for the ASTM D 2344 standard SBS test fixture. This device, shown in Figure 3-24, was placed between supports and allowed the loading nose to rest directly in the center before tightening each of these supports in the test fixture. The distance between lower supports could be further adjusted using spacers placed at each side of the alignment device as needed.

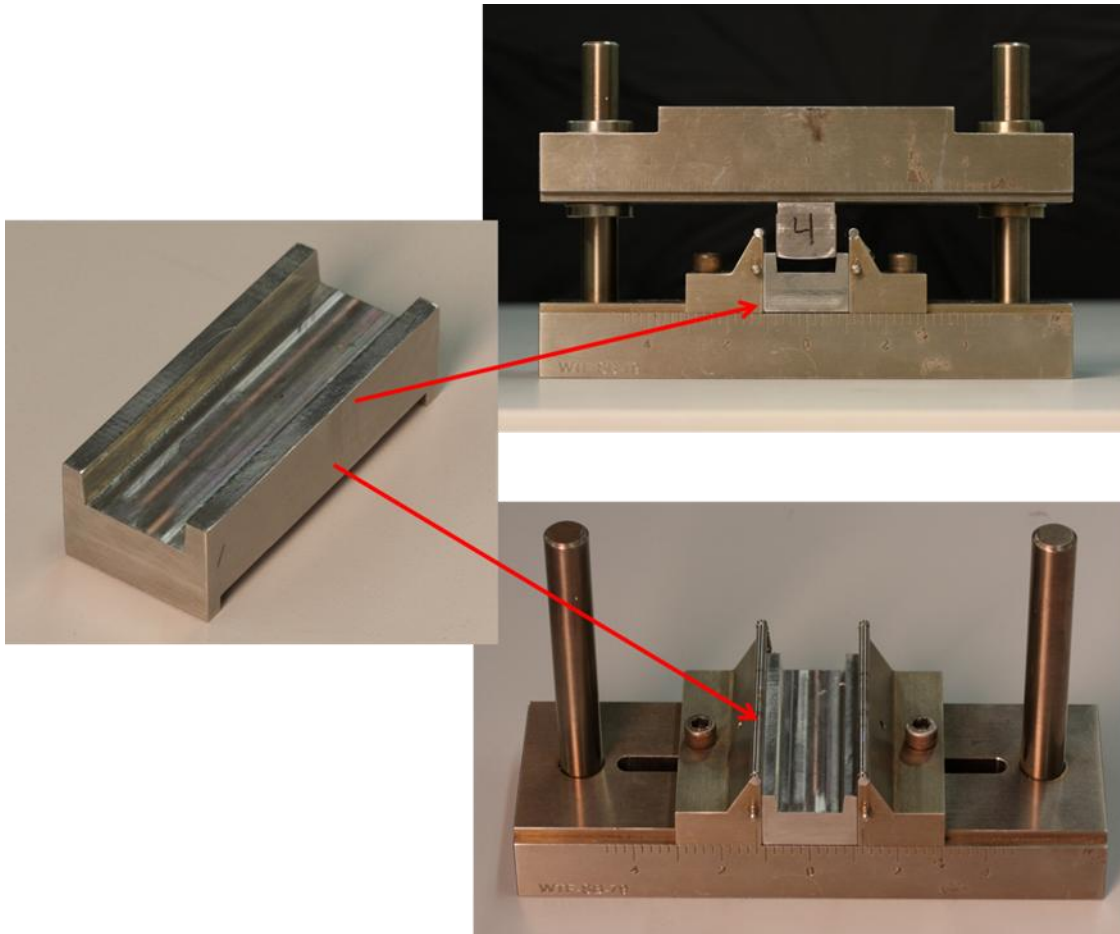


Figure 3-24 Alignment device for the ASTM D 2344 Wyoming SBS test fixture

In this study, the SBS specimens were placed in a servohydraulic load frame and monotonically loaded at .05 in. (1.27 mm)/min crosshead displacement rate until failure.

Figure 3-4(a) shows a typical interlaminar shear failure for SBS specimens in the (1-3) material plane. Axial compressive failure was observed for specimens with s/t ratios larger than 6. Figure 3-2 schematically shows a typical compression failure for such specimens.

DIC, Vic3D software, was used to assess the Lagrange strain tensor components on the specimen surface [29]. Each specimen was analyzed using a subset

window size of 35x35 pixels, corresponding to an approximate area of .0006 in² (.39 mm²) for SBS specimens. Displacement vectors were analyzed on 7 pixel centers, resulting in roughly 14,000 data points for SBS tests. The displacement measurements were then numerically differentiated over a local neighborhood using a 15x15 array of points applied to a strain algorithm in VIC-3D software in order to compute the Lagrange strain tensor components [29].

DIC measurements for IM7-carbon/8552-epoxy unidirectional tape composites under quasi-static loading conditions confirm that for each tested span a close to linear axial normal strain distribution, ϵ_{11} , through the thickness of the specimen far from the loading and support locations, is observed until failure. Strain data was extracted over a .079 in. (2 mm) region between the loading nose and support. The transverse normal (thickness) coordinate, y , is normalized with respect to the thickness of the specimen. Eq. (4) is used to generalize the interlaminar shear stress-strain relationship for each specimen. Eq. (13) is used to assess the axial tensile and compressive modulus for each specimen.

Interlaminar shear stress-strain relations generated based on the closed form shear stress approximation (19) were compared with FEM stress based shear stress-strain response for IM7-carbon/8552-epoxy unidirectional tape. Initial interlaminar shear failure was observed in each SBS specimen with s/t ratios less than 7. Compressive(flexural) failure was observed for specimens with s/t ratios greater than 6. In Figure 3-25 the average interlaminar shear stress-strain curve is shown for each s/t ratio using beam theory shear stress approximations and DIC based strains.

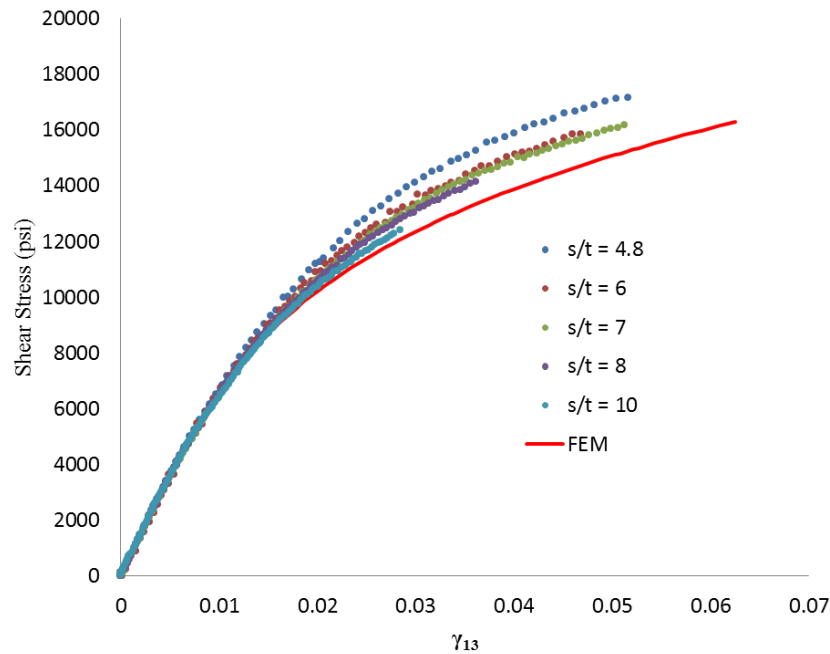


Figure 3-25 Comparison of average interlaminar shear stress-strain curve for each span with FEM results for IM7-carbon/8552-epoxy SBS specimens

In this study, accurate shear stresses were generated using a 3D FEM model in ABAQUS finite element analysis software. The iterative FEM based procedure developed in Ref. [10, 23] resulted in the accurate nonlinear portion of the shear stress-strain curve for the carbon/epoxy material. The material properties were obtained using this iterative method for the specimens tested at a s/t ratio equal to 4.8. These material parameters were then used as the initial estimate for all subsequent tests. Each s/t ratio FEM model converged after a single iteration, when using the DIC based strains from each specimen, and the material parameters obtained from the iterative procedure for SBS carbon/epoxy specimens with a s/t ratio of 4.8, further verifying the parameters obtained using the iterative FEM procedure as accurate material properties. The interlaminar shear stress-strain relationship predicted by FEM for IM7-carbon/8552-epoxy is included in Figure 3-25. Results from Figure 3-26 show that the measured interlaminar

shear stress-strain response changes for different s/t ratios in the nonlinear regime, tending towards the FEM based response as the s/t ratio of the SBS test increases. For SBS tests using a s/t ratio of 10 the interlaminar shear stress-strain response is within 5% of FEM based response. This is a major improvement from an error reaching a maximum up to 17% near failure for SBS carbon/epoxy specimens tested at a s/t ratio of 4.8. The relationship between FEM based maximum interlaminar shear stresses and beam theory maximum shear stress approximations for each span can be seen in Figure 3-26, which shows an increase in accuracy of the beam theory stress approximations for increasing s/t ratios of the SBS test method.

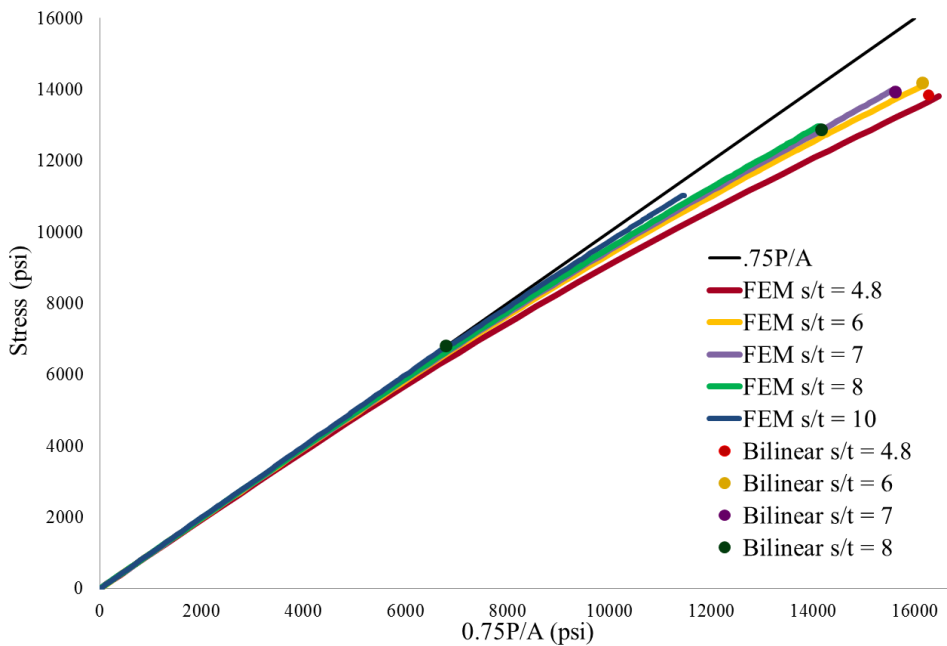


Figure 3-26 Comparison between closed form shear stress approximations and finite element predictions for the maximum shear stress of carbon/epoxy SBS specimens tested at different spans

For more accurate maximum shear stress approximations in the nonlinear regime of SBS specimens tested with s/t ratios less than 10 an FEM or an alternative stress model should be used. A bilinear stress model was introduced in Reference [19] for both glass/epoxy and carbon/epoxy SBS specimens tested using a s/t ratio equal to 5. Observations from this study show that the s/t ratio changes the relationship between the closed form maximum shear stress approximations (19) and FEM based maximum shear stress in the beam. The following bilinear model represents an engineering approximation which keeps the error below 5% for carbon/epoxy SBS specimens with varying s/t ratios.

$$\tau_{13} = \begin{cases} \frac{3P}{4A}, & \frac{3P}{4A} \leq \tau_0 = 6800 \text{ psi} \\ \left((0.03(s/t) + 0.6) \left(\frac{3P}{4A} - 6800 \right) \right) + 6800, & \frac{3P}{4A} > \tau_0 = 6800 \text{ psi} \end{cases} \quad (30)$$

As the beam become longer with respect to its cross section the closed form solution (19) becomes a more accurate representation of the stresses throughout the beam. In Figure 3-27 the average interlaminar shear stress-strain responses are plotted using Eq. (30) for maximum shear stress approximations. For the interlaminar shear stress-strain response of the specimens tested with a s/t ratio of 10, closed form maximum shear stress approximations (19) were still used, which demonstrates the applicability of the closed form solution (19) to the three point loading configuration for longer s/t ratios.

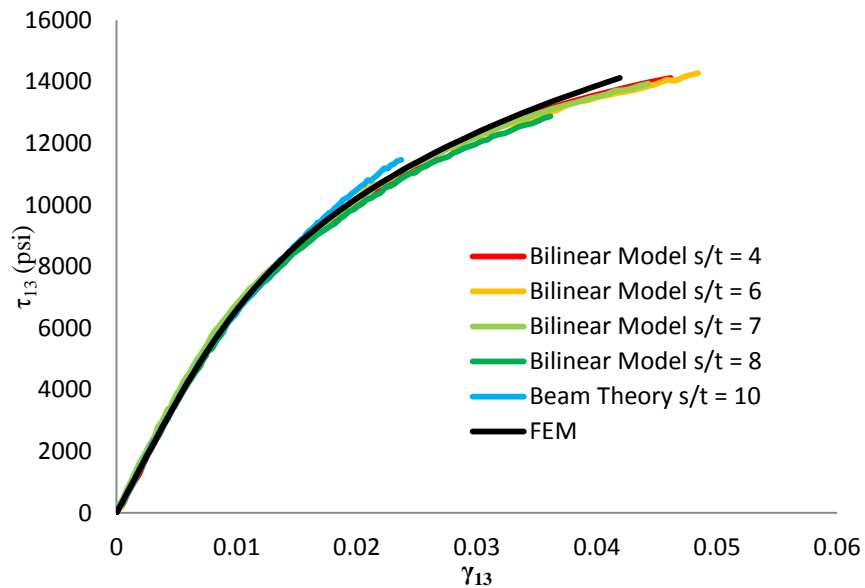


Figure 3-27 Average interlaminar shear stress-strain curve for IM7-carbon/8552-epoxy tested at varying spans using the bilinear model (30) for the maximum shear stress approximation along with FEM based shear stress-strain curve

In Figure 3-27 the interlaminar shear stress-strain responses for each s/t ratio tested, using (30) for maximum shear stress prediction, collapse into a single curve that follows the same trend as the FEM based material interlaminar shear stress-strain response for IM7-carbon/8552-epoxy unidirectional tape.

Table 3-9 lists the average measurements from both the left and right side of each set of SBS tests. Axial normal tensile and compressive moduli results were compared with material properties published by the prepreg manufacturer [36] and generated using ASTM standard methods for measurement. These values for IM7-carbon/8552-epoxy include 23.7 msi (163.4 GPa) for the axial normal tensile modulus and 21.7 msi (149.6 GPa) for the axial normal compressive modulus. The tensile and compressive modulus results from Table 3-9 are consistent with the parameters generated by the prepreg manufacturer and show little variability, less than 4%, between

the different s/t ratios tested. A relatively low compressive modulus compared with manufacturer provided data was consistently measured for each SBS test, and is confirmed from the average tensile and compressive modulus measurement from four point bending tests that are discussed in a later chapter.

Table 3-9 IM7-Carbon/8552-Epoxy material properties for various s/t ratios (English units).

Span(in)	Side	Value	G ₁₃ (ksi)	K ₁₃	n ₁₃	E _{11T} (msi)	E _{11C} (msi)	E ₁₁ AVG (msi)	S ₁₃ (ksi)
1.20	Left	AVG COV	718 (1.3%)	39913 (8.1%)	.2254 (8.4%)	24.0 (3.7%)	20.1 (1.1%)	21.9 (2.1%)	15.9 (1.0%)
	Right	AVG COV	717 (4.1%)	39817 (7.0%)	.2280 (7.5%)	23.9 (2.6%)	19.5 (2.1%)	21.6 (1.2%)	
1.30	Left	AVG COV	700 (2.5%)	41310 (3.9%)	.2412 (4.2%)	24.8 (4.8%)	18.9 (5.1%)	21.5 (2.0%)	16.5 (2.8%)
	Right	AVG COV	743 (1.8%)	44396 (5.5%)	.2567 (5.6%)	24.5 (3.1%)	20.4 (2.1%)	22.3 (1.9%)	
1.50	Left	AVG COV	715 (3.4%)	40595 (4.7%)	.2499 (3.1%)	23.4 (5.21%)	19.7 (.5%)	21.4 (2.6%)	16.0 (1.3%)
	Right	AVG COV	725 (3.8%)	41928 (5.4%)	.2532 (5.4%)	24.3 (2.7%)	20.0 (4.6%)	22.0 (2.2%)	
1.75	Left	AVG COV	716 (1.9%)	40256 (8.1%)	.2473 (7.7%)	23.1 (4.4%)	19.8 (2.4%)	21.3 (2.5%)	N/A
	Right	AVG COV	711 (3.0%)	40949 (7.2%)	.2510 (6.9%)	22.9 (5.6%)	19.9 (5.7%)	21.2 (1.1%)	
2.00	Left	AVG COV	703 (2.6%)	40248 (8.0%)	.2506 (6.6%)	23.0 (1.7%)	19.9 (1.6%)	21.4 (1.1%)	N/A
	Right	AVG COV	700 (2.0%)	42554 (5.5%)	.2667 (5.2%)	22.5 (4.2%)	19.5 (2.4%)	20.9 (1.3%)	
2.50	Left	AVG COV	698 (2.3%)	36440 (4.4%)	.2440 (4.0%)	22.2 (1.6%)	20.1 (2.9%)	21.1 (1.0%)	N/A
	Right	AVG COV	699 (2.3%)	36973 (4.5%)	.2450 (4.2%)	22.2 (1.9%)	20.0 (2.2%)	21.1 (1.2%)	

Table 3-10 IM7-Carbon/8552-Epoxy material properties for various s/t ratios (SI units).

Span(mm)	Side	Value	G ₁₃ (GPa)	K ₁₃ (MPa)	n ₁₃	E _{11T} (GPa)	E _{11C} (GPa)	E ₁₁ AVG (GPa)	S ₁₃ (MPa)
30.5	Left	AVG COV	4.95 (1.3%)	275 (8.1%)	.2254 (8.4%)	165.5 (3.7%)	138.6 (1.1%)	151.0 (2.1%)	109.6 (1.0%)
	Right	AVG COV	4.94 (4.1%)	275 (7.0%)	.2280 (7.5%)	164.8 (2.6%)	134.4 (2.1%)	148.9 (1.2%)	
33.0	Left	AVG COV	4.82 (2.5%)	285 (3.9%)	.2412 (4.2%)	171.0 (4.8%)	130.3 (5.1%)	148.2 (2.0%)	113.7 (2.8%)
	Right	AVG COV	5.12 (1.8%)	306 (5.5%)	.2567 (5.6%)	168.9 (3.1%)	140.7 (2.1%)	153.8 (1.9%)	
38.1	Left	AVG COV	4.93 (3.4%)	280 (4.7%)	.2499 (3.1%)	161.3 (5.21%)	135.8 (.5%)	147.5 (2.6%)	110.3 (1.3%)
	Right	AVG COV	5.00 (3.8%)	289 (5.4%)	.2532 (5.4%)	167.5 (2.7%)	137.9 (4.6%)	151.7 (2.2%)	
44.5	Left	AVG COV	4.94 (1.9%)	278 (8.1%)	.2473 (7.7%)	159.3 (4.4%)	136.5 (2.4%)	146.9 (2.5%)	N/A
	Right	AVG COV	4.90 (3.0%)	282 (7.2%)	.2510 (6.9%)	157.9 (5.6%)	137.2 (5.7%)	146.2 (1.1%)	
50.8	Left	AVG COV	4.85 (2.6%)	278 (8.0%)	.2506 (6.6%)	158.6 (1.7%)	137.2 (1.6%)	147.5 (1.1%)	N/A
	Right	AVG COV	4.83 (2.0%)	293 (5.5%)	.2667 (5.2%)	155.1 (4.2%)	134.4 (2.4%)	144.1 (1.3%)	
63.5	Left	AVG COV	4.81 (2.3%)	251 (4.4%)	.2440 (4.0%)	153.1 (1.6%)	138.6 (2.9%)	145.5 (1.0%)	N/A
	Right	AVG COV	4.82 (2.3%)	255 (4.5%)	.2450 (4.2%)	153.1 (1.9%)	137.9 (2.2%)	145.5 (1.2%)	

The current short beam method has also been successfully used to measure the interlaminar tensile (ILT) modulus, E_{33T}. To enable assessment of the ILT modulus in this work, six short-beam specimens were machined in the thickness direction from a 106-ply thick IM7/8552 carbon/epoxy unidirectional tape panel cured at 350 degrees F per prepreg manufacturer's specifications [36]. The cured ply-thickness was approximately

0.183 mm (0.0072 in) resulting in 19.4-mm (0.76-in) panel thickness. Therefore, the ILT short-beam specimen length is 19.4-mm (0.76-in). The coupons are 3.8-mm (0.15-in) thick, and 2.8-mm (0.11-in) wide. The coupon thickness corresponds to the in-ply 90-degree principal material direction; and the 2-3 principal material plane is the plane of loading. The short-beam specimens were placed in an ASTM D 2344 test fixture with a 0.5-inch diameter loading nose and 0.125-inch diameter supports; and loaded in an electromechanical load frame at a constant 0.05 in/min crosshead displacement rate till failure. The support length was 0.59 inches, resulting in a s/t ratio of 4. The tests were conducted at 72° F room-temperature ambient conditions. All short-beam specimens failed in tension in the middle of the specimen as shown in Figure 3-2.

All coupons exhibited similar behavior. Figure 3-28 shows typical Lagrange surface strain tensor components measured right before failure using the DIC technique. The DIC strain analysis used a subset (data point) size of 31×31 pixels, corresponding to approximately 0.227 mm² for these particular tests. Data was obtained on 5 pixel centers, resulting in approximately 6,000 data points per load case. The displacement measurements were then numerically differentiated over a local neighborhood using a 15x15 array of points applied to a strain algorithm in VIC-3D software in order to compute the Lagrange strain tensor components [29]. The strain distributions in Figure 3-28 are well within the linear elastic range [22]. Also the short-beam coupons exhibit a linear through-the-thickness axial strain, ϵ_{33} , distribution throughout the coupons, including the cross sections away from the support locations. This allows us to derive the same closed form approximation, Eq. (13), for the interlaminar tensile and compressive modulus. Figure 3-28 shows a typical normalized axial strain distribution through the thickness in a 1 mm long gage area right before failure. A linear distribution is evident. Table 3-11 lists the interlaminar tensile and compressive modulus values measured using the short-beam

tests. The applied force corresponding to the modulus measurements was 205 N (46 lbs) on average. The average ILT modulus value is 9.93 GPa (1.44 msi) and the coefficient of variation (COV) is 5.35%.

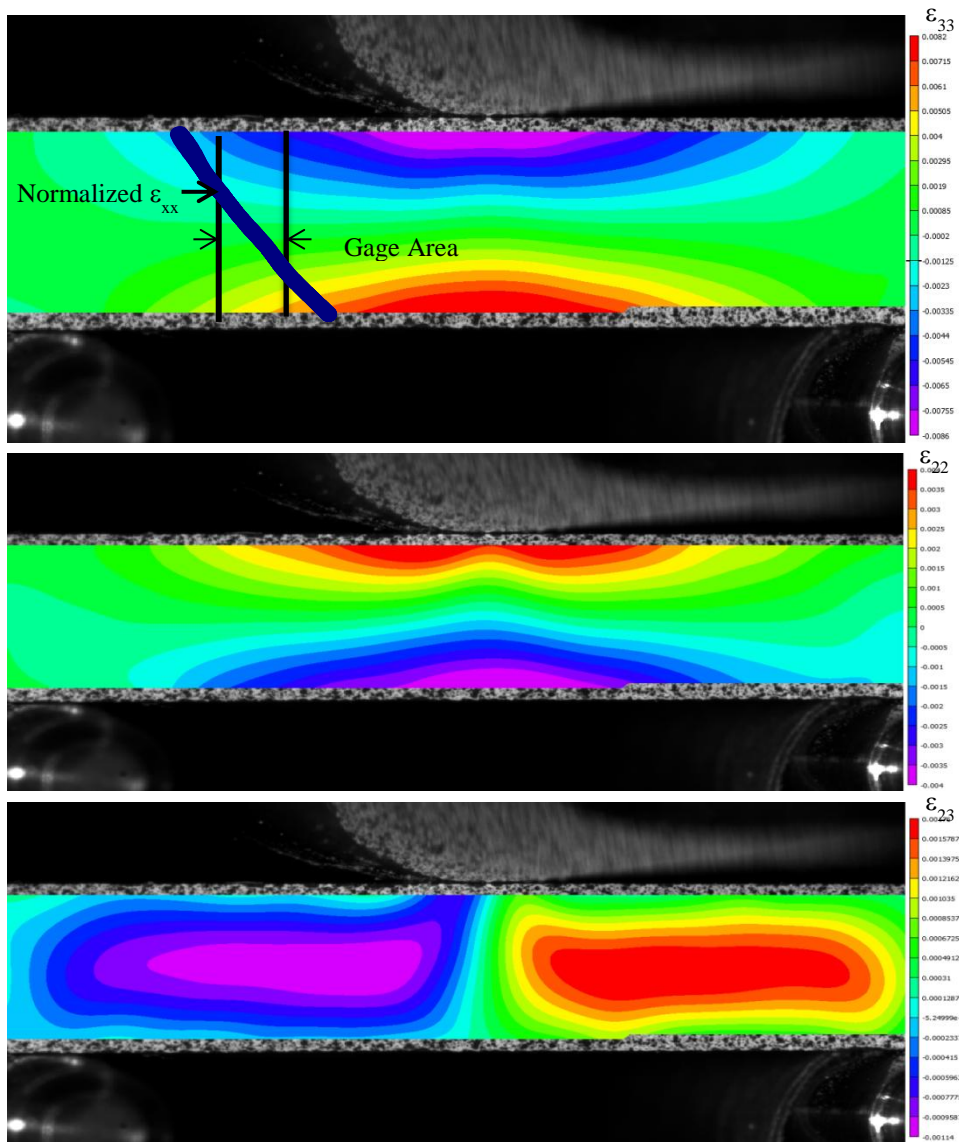


Figure 3-28 Lagrange strain tensor components measured on the short-beam specimen surface right before failure

Table 3-11 Interlaminar tensile and compressive modulus values measured based on the short-beam tests.

IM7/8552	Left Gage Area		Right Gage Area		Average Values	
ILT Short-Beam	E_{33T} GPa (msi)	E_{33C} GPa (msi)	E_{33T} GPa (msi)	E_{33C} GPa (msi)	E_{33T} Gpa (msi)	E_{33C} GPa (msi)
SB1	9.88 (1.43)	8.81 (1.28)	9.86 (1.43)	9.17 (1.33)	9.87 (1.43)	8.99 (1.30)
SB2	9.53 (1.38)	9.04 (1.31)	9.62 (1.39)	8.97 (1.30)	9.57 (1.39)	9.01 (1.31)
SB3	10.10 (1.47)	8.90 (1.29)	10.03 (1.45)	8.25 (1.20)	10.07 (1.46)	8.58 (1.24)
SB4	10.42 (1.51)	9.42 (1.37)	10.31 (1.50)	9.50 (1.38)	10.37 (1.50)	9.46 (1.37)
SB5	9.33 (1.35)	8.42 (1.22)	8.92 (1.29)	8.45 (1.23)	9.13 (1.32)	8.44 (1.22)
SB6	10.37 (1.50)	8.74 (1.27)	10.80 (1.57)	9.74 (1.41)	10.58 (1.53)	9.24 (1.34)
AVG	9.94 (1.44)	8.89 (1.29)	9.92 (1.44)	9.01 (1.31)	9.93 (1.44)	8.95 (1.30)
COV	4.46%	3.75%	6.42%	6.41%	5.35%	4.32%

3.4 DIC Based Axial Strain Distribution Measurements

A small-angle coordinate transformation of the axial strain distribution for unidirectional composites subject to three point bending can cause a large shift between the transformed strain distribution and the original axial strain distribution. The amount shifted is directly related to the stiffness ratio of the material, E_{xx}/G_{xy} . This is important knowledge when measuring the full field strain distribution of a unidirectional composite SBS specimen. Alignment of the coordinate axes associated with the strain measuring

device, in this case the DIC stereo camera system, and the material coordinate axes is imperative for accurate measurement of tensile and compressive moduli. Materials with high stiffness ratios, such as unidirectional carbon/epoxy composites with a stiffness ratio of more than 30 in the (1-3) material plane, are more sensitive to such alignment than materials with lower stiffness ratios, such as unidirectional glass/epoxy composites with a stiffness ratio around 10. Due to the low shear stiffness of unidirectional composite plies compared to the axial stiffness in the fiber direction, much larger shear strains occur along a significant portion of the thickness of the specimen in comparison with the axial strains. Based on the following coordinate transformation it becomes apparent that the much larger shear strains (compared to axial strains) present along the beam will have a noticeable contribution to any transformation of the axial strains even at small angles.

$$\varepsilon_{xx}^* = \frac{\varepsilon_{xx} + \varepsilon_{yy}}{2} + \frac{\varepsilon_{xx} - \varepsilon_{yy}}{2} \cos 2\theta + \frac{\gamma_{xy}}{2} \sin 2\theta \quad (31)$$

Figure 3-29 shows the effect of a positive and negative one-degree coordinate transformation on the axial strain distribution through the thickness, midway between the loading nose and the support location on the right side of a carbon/epoxy unidirectional SBS specimen with a s/t ratio equal to 4.8. Since shear strains are of the opposite signs on the left and right portions of the short beam; and the axial strain in the transformed coordinates is related to the surface strain components in the original coordinate system through Eq. (31), a misalignment between the material coordinate axes and the DIC system axes will artificially increase the axial strain on one side of the specimen and reduce it on the other side.

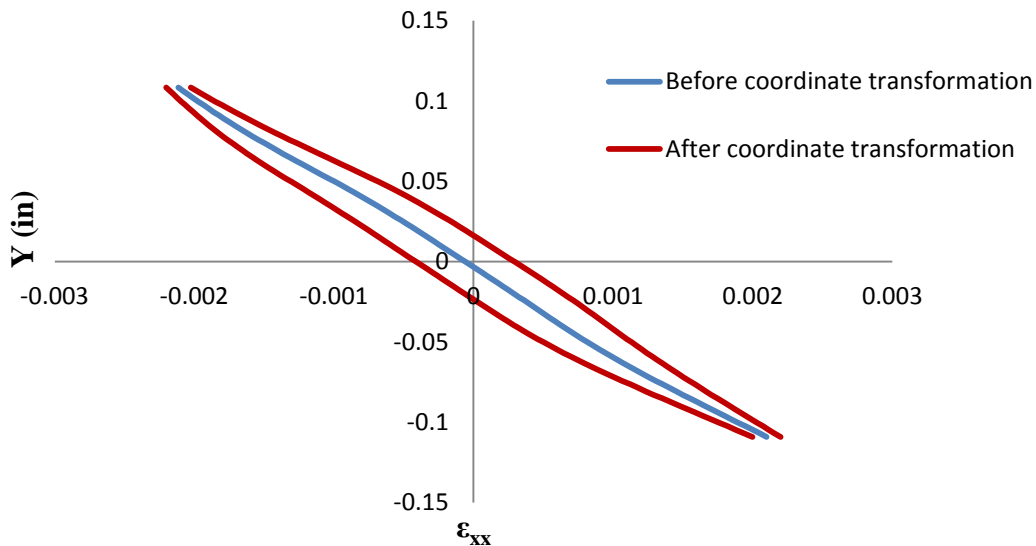


Figure 3-29 Axial strain distribution through the thickness from the left gage region of a IM7-carbon/8552-epoxy SBS specimen tested with a s/t ratio = 4.8 at 85% failure load after coordinate transformations by ± 1 degrees.

Figure 3-29 shows that as a result of a slight misalignment, the shifted strain distributions have similar slopes, but their intercepts differ. The tensile and compressive modulus closed form solution (13) is very sensitive to the slope and intercept of the axial strain distribution. For example, one degree coordinate transformation could change the tensile and compressive modulus approximations by approximately 15% for an IM7/8552 carbon/epoxy SBS specimen with a 4.8 s/t ratio. However, the average modulus determined using Eq. (14) is not effected by the coordinate transformation. Observations from the varying s/t ratio experiments on unidirectional carbon/epoxy composites showed that the axial strain distribution's sensitivity to axes alignment decreases with increasing s/t ratio. This can be attributed to the increase in the bending moment which increases the axial strains in the gage area in comparison to the shear strains. Also taking the measurements near the linear shear regime will decrease this

sensitivity, since this is the point when the ratio between axial and shear strains is greatest. Unlike in the tensile and compressive modulus assessment, sensitivity to coordinate axes alignment is not observed for the interlaminar shear strain distributions in the SBS specimens.

Initially, most of the DIC data used in this study has been slightly misaligned with the principal coordinate axis of the SBS specimens, resulting in inconsistent axial tensile and compressive modulus measurements from both the left and right gage regions. Transformations of the DIC coordinate system were applied in the post-processing step of the Vic3D analysis to account for any coordinate misalignments. The coordinate transformation angle was determined by finding a transformation angle which would produce close to symmetric axial strain distributions on both the right and left side of each specimen tested in a single set. Figure 3-30 shows the axial strain distributions from both the left and right side of an IM7-carbon/8552-epoxy SBS specimen after a small angle coordinate transformation was applied to the DIC data.

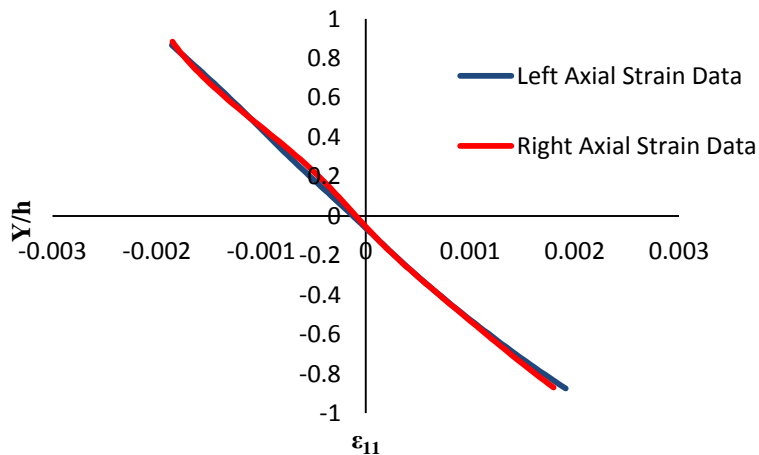


Figure 3-30 Transformed axial strain distribution of both the left and right gage region for an IM7-carbon/8552-epoxy SBS specimen tested with a s/t ratio = 4.8 and loaded in the (1-3) material plane at 65% failure load

3.6 Application of the Short Beam Shear Method for Fatigue and Impact Loading

3.6.1 Fatigue Loading

Fatigue is defined as the change in property as a result of repeated mechanical loading in the appropriate environmental conditions [21]. The ability to predict failure under cyclic loading for composite materials is one of the major challenges in the aerospace industry. Fatigue damage is an important design criteria for composite structural components, in particular for rotating components, such as helicopter rotor blades or wind turbine blades, which experience high cycle counts over short periods of time [37]. The primary failure mechanism of these components is delamination, which can cause significant stiffness loss and possible catastrophic failure of the structure. Therefore, through the thickness (interlaminar) shear fatigue properties are of particular importance in structural design of such components. Important characteristics of a through the thickness shear fatigue test include simple identification of failure initiation, simple specimen preparation, measurement of interlaminar properties, and simple test setup [37].

Fatigue testing is performed by cyclic loading of a test specimen at a load level below static failure load of the material to determine the number of cycles till failure [21]. The ratio between the peak maximum load and peak minimum load of the cycle is known as the load ratio. A load ratio of $R = 0.1$ was used in each of these examples. The test frequency should be at a rate low enough that it does not introduce excessive heat, more than 5° F, to the specimen which can cause thermally induced failure. For polymer composites a loading frequency between 5-10 Hz is generally used [21]. The maximum stress is plotted against the log of the number of cycles to failure for multiple stress levels to generate a semi-log fatigue stress vs. cycles plot (S/N curve).

The ASTM Standard SBS test configuration was used in Ref. [37] to examine the applicability of this test method for generating fatigue S-N curves for carbon/epoxy composites. Matrix cracking was observed in Ref. [37] before ultimate failure resulting in a combined failure mode, therefore, the authors discouraged the use of the SBS test for measuring interlaminar shear fatigue properties of carbon/epoxy composites. Using the modified SBS test configuration, accurate fatigue shear properties can be generated for unidirectional composite materials in the (1-3) principal material plane. This is demonstrated for both glass/epoxy and carbon/epoxy unidirectional composite tape SBS specimens in Ref. [19], where interlaminar shear S-N curves are generated for IM7-carbon/8552-epoxy and E-glass/5216-epoxy. Increasing the loading nose diameter reduces the transverse stresses under the loading nose ensuring a consistent interlaminar shear failure mode for each specimen. Full field deformation measurements can be obtained at specified cycles and load values, defined by the user in the DIC image capturing software. Although strain measurements are not used to generate fatigue (S-N) curves, useful information can come from monitoring the deformation of the specimen throughout its fatigue life. In addition, a more precise cycles till failure count can be achieved by taking incremental images throughout the life of the specimen.

The exposure time used to capture images for DIC is not a primary concern for quasi-static SBS tests, but for situations where object motions occur during image acquisition the role of this parameter becomes more significant. The average image displacement during the exposure time can be approximated as the vertical velocity times the exposure time and the image magnification. This value can be compared with the average calibration variability to determine if the exposure time is too large; i.e. if this value is larger than the average calibration variability [29].

DIC can be used to monitor both the peak strain and strain hysteresis of the test. Since the DIC system is limited to capturing images at a 1 Hz frequency, a single strain cycle consists of images taken from several consecutive cycles at different load values. For instance, it would take 400 cycles (40 s) to obtain a 40 data point stress-strain hysteresis for a test running at a 10 Hz frequency.

For demonstration purposes two IM7-carbon/8552-epoxy unidirectional composite SBS specimen were cyclically loaded at 68% and 70% failure stress. More accurate stress models, such as Eq. (5) or (30) can be used to approximate maximum shear stress in the beam instead of (19) for carbon/epoxy composite specimens tested in the nonlinear shear regime. The load was applied at a 10 Hz frequency with a load ratio of $R = .1$. The dimensions of the specimens were .25 in. (6.4 mm) thickness and .25 in. (6.4 mm) width. A 1.2 in. (30.5 mm) span was used equaling a 4.8 s/t ratio. A loading nose diameter of 4 in. (101.6 mm) was used. Interlaminar shear failure was observed. A 16 MP stereo camera system combined with DIC software, Vic3D, was used to obtain full field deformation measurements and strain assessments of the specimen using the same input parameters as the static test method. Images are obtained at peak loads every 500 cycles to obtain full field strain calculations throughout the life of each specimen. Sufficiently small exposure time was used for reliable DIC measurements. Average peak interlaminar shear strains were obtained from a .079 in. (2 mm) gage region between loading nose and support. Figure 3-31 shows the shear strain history of the SBS specimen at the location of delamination midway between support and loading nose for peak load levels.

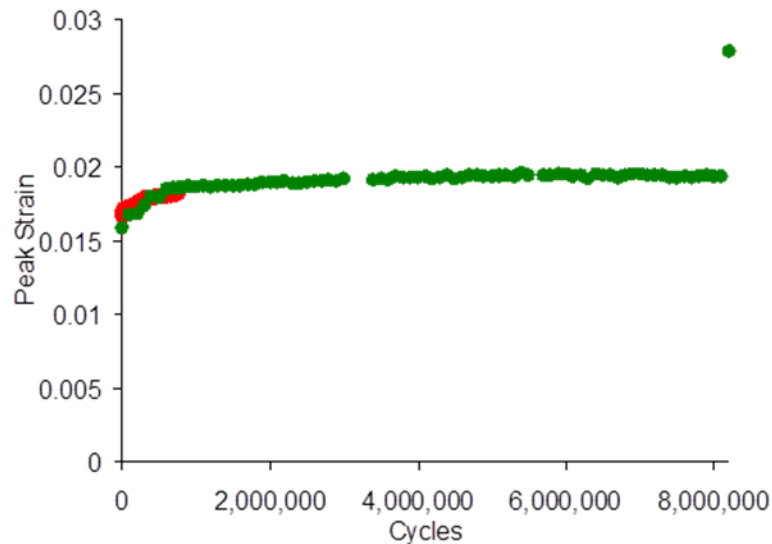


Figure 3-31 Interlaminar shear strain history for fatigue IM7/8552 SBS tests at peak cyclic stresses equal to 68% and 70% of the static interlaminar shear strength

The strain history can be broken into three phases; an initial rapid increase in strain, small linear increase, followed by failure where strain increases abruptly. The sharp increase in peak shear strain at the end of the loading history is most likely caused by non-visible damage accumulation in the matrix before onset of visible delamination. An increase in up to 20% of the original peak shear strain value is observed for each of the specimens in the first few hundred thousand cycles.

To monitor stress-strain behavior of a material under fatigue loading, images can be obtained throughout the loading cycle. Figure 3-32 shows the stress strain behavior over the life cycle of the second IM7-carbon/8552-epoxy SBS specimen also subject to cyclic loading with a peak shear stress value at 68% of its static strength. Forty images were taken for each cycle set. The stress-strain cyclic behavior was not captured in the fatigue region characterized by a sharp increase in peak shear strain observed right before failure for this specimen. Since the shear strain increase occurs abruptly and over

such a small number of cycles, it is difficult to capture the stress-strain behavior in this region of the fatigue life.

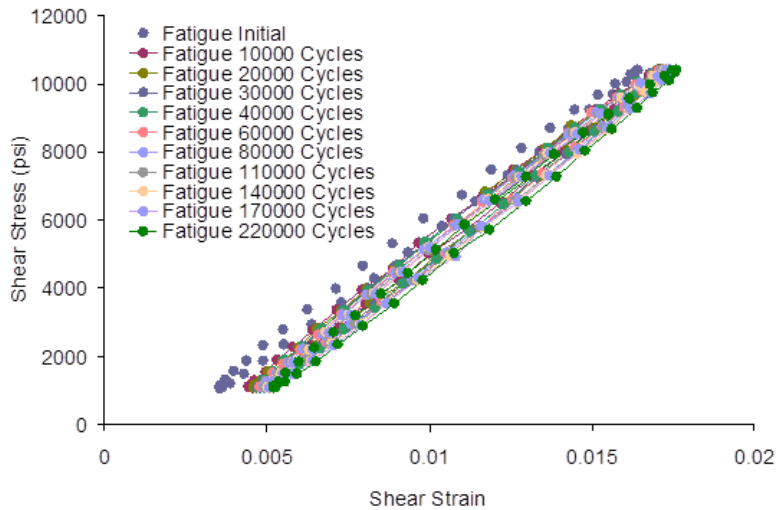


Figure 3-32 Interlaminar shear stress-strain response for early stages of fatigue loading

A constant shear modulus is observed in the early stages of the fatigue loading. Such observations might be useful when developing fatigue damage models [38]. The increase that is observed in the peak shear strains over the fatigue life appear not to be caused by a change in stiffness, but in a kinematic shift of the fatigue stress-strain behavior. This could be caused by creep which is a known behavior for polymer matrix composites [39], however, the mechanism behind the shear strain increase has not been fully investigated.

3.6.2 Impact Loading

In addition to fatigue and static loading conditions, the short beam shear method coupled with DIC deformation measurements can be used to obtain the shear stress-strain behavior of unidirectional composites subject to impact loading conditions. The process of a short-beam specimen subjected to drop-weight impact is a complex event. Nevertheless, the nature of impact response can be approximated to a quasi-static event

since duration of the impact is long compared to the speed of the stress wave propagation through the specimen and the ratio of the impactor mass to specimen mass is on the order of hundreds [40]. Furthermore, since the quasi-static equilibrium is achieved well before the onset of failure, the desired failure mode, i.e., shear delamination, can be obtained. Also, preliminary measurement of deformation in low-velocity impact tests using unidirectional fiberglass SBS coupons proves that the deformation rate of the material during the impact loading quickly becomes constant and stays constant till delamination failure. Constant velocity during the impact test supports the quasi-static equilibrium based approximation of shear stresses. To demonstrate the applicability of the SBS test method for impact loading conditions five low velocity SBS impact tests were run for S2-glass/E773-epoxy unidirectional composite tape in the (1-3) material plane. An Instron gravity based load frame was used to perform impact tests at a 4.4 m/s impact velocity corresponding to 10^2 strain rate. An impactor weight of 6.2 lbs (2.8 kg) was used. The specimen geometry is consistent with both static and fatigue tests; .25 in. (6.4 mm) thickness and .25 in. (6.4 mm) width. A 2 in. (50.8 mm) diameter impact loading nose was used for all specimens. Figure 3-33 shows a typical test setup used for impact SBS tests.

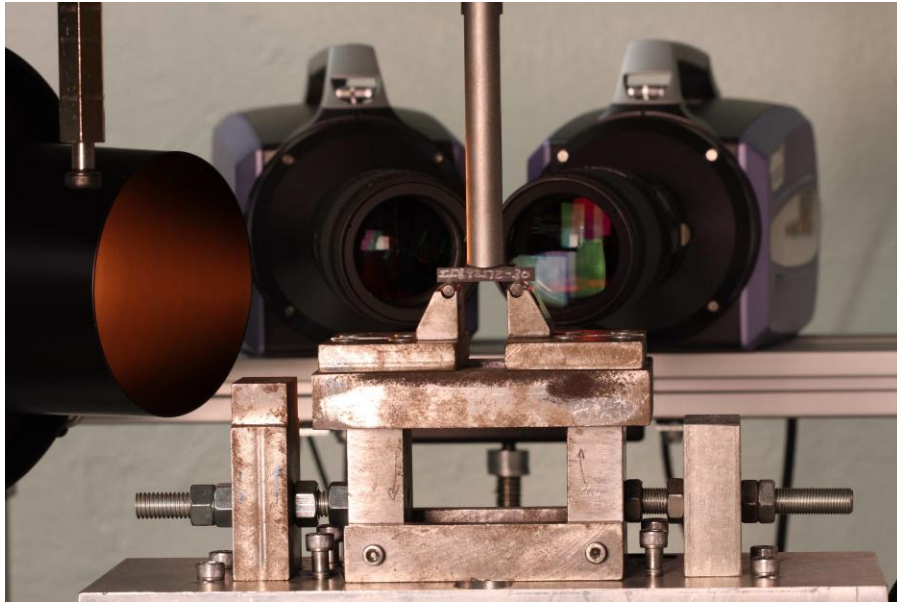


Figure 3-33 Experimental setup for three point bending impact test with a two inch diameter impactor nose

DIC software Vic3D [29] was used in this work for assessment of Lagrange strain tensor components on the specimen surface. A sequence of images are acquired using a stereo camera system. For impact testing a Shimadzu high speed camera system is used that can record up to 1 million frames per second while maintaining a constant resolution of .8 MP, allowing more than 50 images to be captured per specimen. Initial interlaminar shear delamination can be captured in these images. Figure 3-34 shows a typical interlaminar shear failure for an S2-glass/E773-epoxy SBS specimen subject to 4.4 m/s impact.

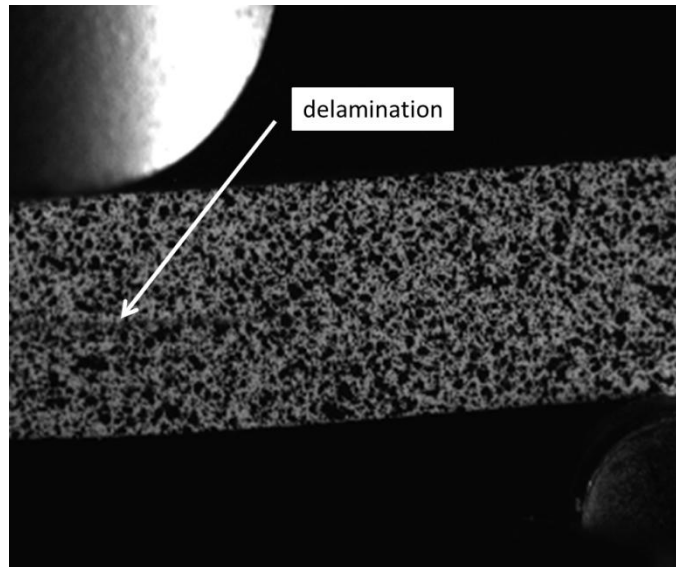


Figure 3-34 Shear delamination failure of unidirectional S2-glass/E773-epoxy SBS specimens subject to drop-weight impact

Initial images are set at impact initiation. A force vs. time curve is generated from a strain gage sensor connected to the impactor. Force data can be acquired at 2 million frames per second. Images were obtained at ¼ million frames per second for these low velocity tests. Figure 3-35 compares the contact force history obtained from the S2-glass/E773-epoxy SBS specimens with the force history obtained using an explicit FEM simulation implementing S2-glass/E773-epoxy material properties. An explicit FEM was developed in Abaqus/Explicit with the obtained nonlinear shear properties obtained from experimental results. The FEM involved geometric nonlinearity, material nonlinearity and contact interaction. Only half width of the specimen was modeled, using appropriate symmetry boundary conditions in the 1-3 plane. The impact nose and supports were assumed to be rigid and modeled with cylindrical surfaces. A discrete mass representing the impactor weight was tied to the reference point of the impact nose and an impact velocity was applied at the reference point to simulate the low-speed impact event. 8-

node brick elements with reduced integration (C3D8R) were used for better computational efficiency. The nonlinear shear model was implemented via user subroutine VUMAT. The time history of impact load was extracted from the reaction force at the reference point of the impact nose.

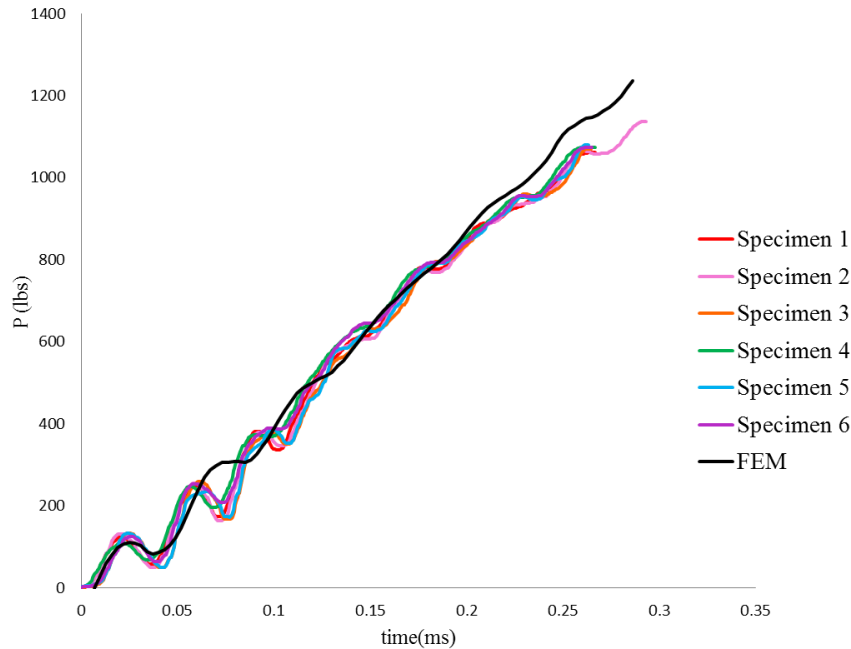


Figure 3-35 FEM and experimental contact force history for S2-glass/E773-epoxy SBS impact tests run at a 4.4 m/s impact velocity (10^2 strain rate)

The good agreement between the FE results and the test measurements in the impact load histories demonstrates that the dynamic characteristics of the specimens at impact strain rates of $10^2/s$ are captured by the FEM. For further verification the surface strain tensor components contour plots are compared using both FE based strains and DIC based strains. As can be seen in Figure 3-36 good agreement is found between FEM and DIC based strain distributions. Both of these observations give us confidence in the developed FEM to accurately model the stress strain behavior of the SBS specimen subject to low velocity impact loads. FE-based maximum shear stresses for

the impact model are within 5% of stresses approximated using Eq. (19) at close to failure loads, confirming the applicability of the geometric stress approximation to low velocity impact S2-glass/E773-epoxy SBS tests. Such approximations are used to measure the shear stress-strain response under impact loads in this work.

Each specimen was analyzed using a subset window size of 17x17 pixels, corresponding to an approximate area of .0014 in² (.904 mm²) for SBS specimens. Displacement vectors were analyzed on 5 pixel centers, resulting in roughly 1,000 data points for SBS tests. The displacement measurements were then numerically differentiated over a local neighborhood using an 11x11 array of points applied to a strain algorithm in VIC-3D software in order to compute the Lagrange strain tensor. We can compare the load history curve with the DIC based strain history curve to approximate load values for each specific strain level. The force curve is used to approximate the stresses in the beam for each image from static equilibrium. Close to linear axial strain distributions through the thickness of the specimen are observed till failure. Figure 3-36 shows a typical axial, transverse, and shear surface strain distribution for an S2-glass/E773-epoxy SBS specimen subject to 4.4 m/s impact at close to failure load.

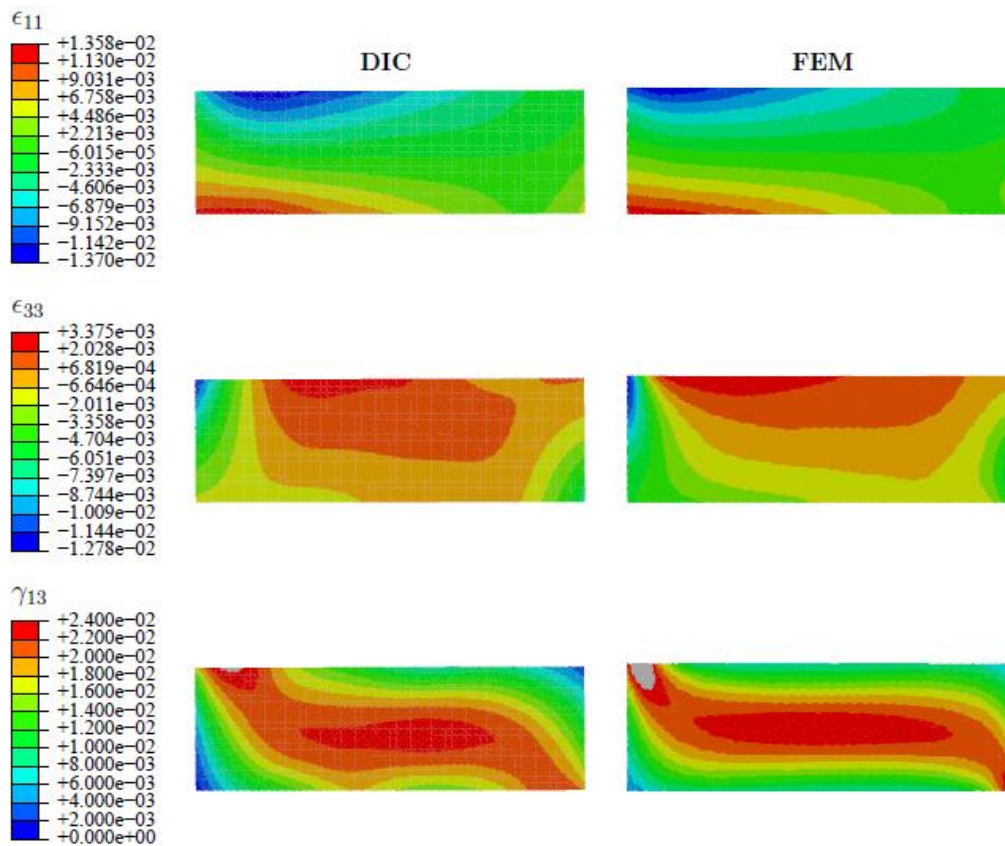


Figure 3-36 DIC data and FE results for surface strain components for a unidirectional S2-glass/E773-epoxy SBS specimen at $t = 0.240$ ms

The low resolution of the high speed camera system, .8 MP, decreases the image scale factor, measured in pixels/mm (in.), requiring larger subset regions for DIC deformation and strain analysis. The subset regions used in these tests are approximately three times larger in physical size than the subset regions of the typical static and fatigue SBS specimens. Using the prescribed parameters, the displacements are differentiated over a region of .12 x .12 in. (3x3 mm), known as the strain window, in the Vic3D software to calculate the Lagrange strain tensor. The large strain window introduces additional error to the DIC calculations, most noticeable in regions of strong

strain gradient. The cause of these errors is explained further in a later chapter. The effects of a larger subset region and strain window to the strain measurements of the SBS specimen using the DIC Vic3D software was simulated for S2-glass/E773-epoxy unidirectional composite tape tested in the (1-3) principal material plane by applying larger input parameters to the analysis of high resolution static SBS specimens. Parameters were chosen such that the subset area and step size compared with impact tests, the filter size was then determined based off these values. It is observed from each S2-glass/E773-epoxy SBS static specimen that a constant ratio of .11 (11%) of the peak interlaminar shear strain can be added to the original measured strain value as a good approximation of the true maximum shear strain in the specimen. This value is further confirmed in a later section for S2-glass/E773-epoxy by simulating the effect of the physical size of the filter on the resulting shear strain distribution for this material system. The shear stress-strain response for each of the six specimens is plotted in Figure 3-37 along with the static stress-strain response for S2-glass/E773-epoxy SBS specimens tested from the same panel.

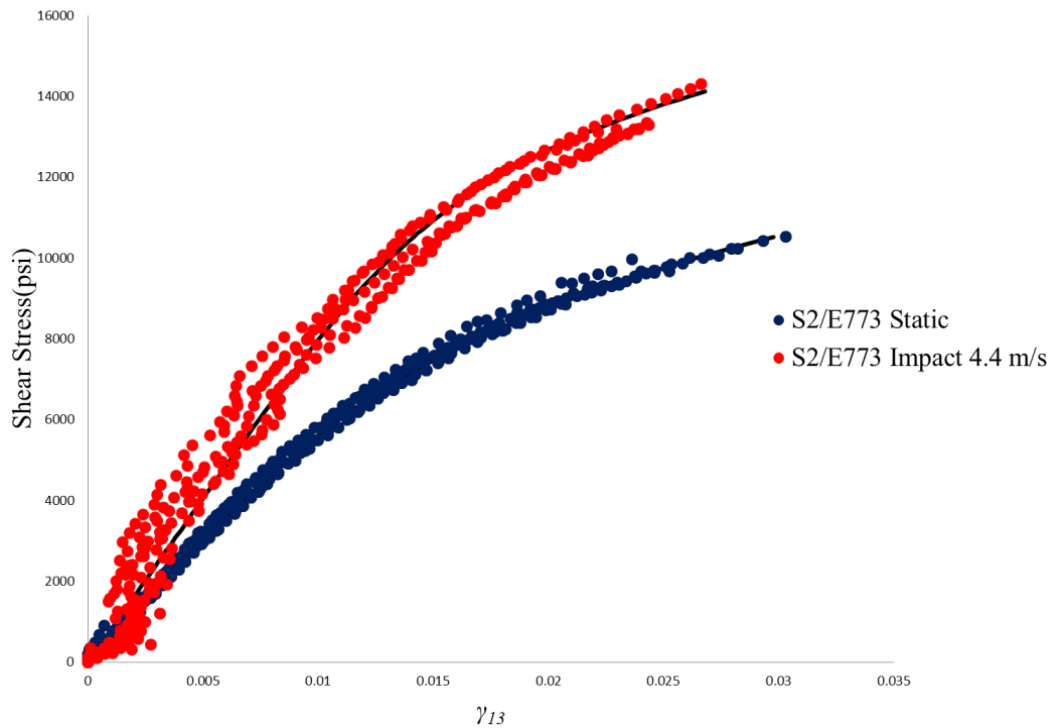


Figure 3-37 Shear stress strain responses for unidirectional S2-glass/E773-epoxy SBS specimens subjected to quasi static and 4.4 m/s impact tests

The average shear stress-strain response under impact loading conditions can be generalized using log-linear regression. Specifically, the Ramberg-Osgood equation (4) is used in this work for direct comparison of the nonlinear shear stress-strain parameters of S2-glass/E773-epoxy unidirectional composite tape subject impact velocity of 4.4 m/s and static loading conditions. Such impact load resulted in approximately $10^2/s$ strain rate. It should be noted that alternative nonlinear models could be used to generalize this response. Table 3-12 lists the linear shear modulus, G_{13} , secant-intercept modulus, K_{13} , and exponent term, n_{13} , associated with the Ramberg-Osgood equation (4) as well as the interlaminar shear strength, S_{13} measured from S2-glass/E773-epoxy unidirectional composite SBS specimens subject to 4.4m/s impact tests.

Table 3-12 Specimen dimension, failure loads and shear properties for unidirectional S2-glass/E773-epoxy prepreg tape measured from 4.4 m/s impact tests

Specimen	T mm(in)	W mm(in)	G_{13} GPa (msi)	K_{13} MPa (msi)	n_{13}	S_{13} MPa (ksi)
1	6.0 (.236)	6.4 (.250)	5.27 (.765)	197.5 (28.64)	.156	91.7 (13.3)
2	6.0 (.236)	6.3 (.2495)	4.95 (.718)	209.0 (30.31)	.158	98.7 (14.3)
3	6.0 (.236)	6.3 (.249)	5.70 (.826)	205.2 (29.77)	.172	91.0 (13.2)
4	6.0 (.236)	6.3 (.2495)	5.15 (.747)	211.8 (30.72)	.164	91.0 (13.2)
5	6.0 (.2375)	6.3 (.249)	5.71 (8.28)	204.2 (29.62)	.169	92.0 (13.4)
AVG	6.0 (.2363)	6.3 (.2494)	5.36 (.77)	205.5 (29.81)	.164	92.9 (13.5)
COV	.4%	.3%	6.3%	2.6%	2.6%	3.5%

Low variability is observed in the measured results. Table 3-13 lists the average interlaminar shear properties measured from both the static S2-glass/E773-epoxy SBS tests and 4.4 m/s impact SBS S2-glass/E773-epoxy tests cut from the same panel.

Table 3-13 Comparison of shear properties under quasi static and 4.4 m/s impact tests
for unidirectional S2-glass/E773-epoxy prepreg tape

	S2-glass/E773-epoxy Static	S2-glass/E773-epoxy Impact
G_{13} , GPa (msi)	4.17 (.604)	5.36 (.777)
K_{13} , MPa (msi)	187.1 (27.13)	205.5 (29.8)
n_{13}	.218	.164
S_{13} MPa (ksi)	70.2 (10.2)	92.9 (13.47)

These results indicate a sensitivity of the shear stiffness to strain rate effects. An increase of approximately 25% is observed for the linear shear stiffness of S2-glass/E773-epoxy due to low velocity impact loads resulting in strain rates of $10^2(1/s)$.

Chapter 4

Verification Tests

4.1 V-notch Specimens

To verify the interlaminar shear measurements obtained from the short beam method the V-notch test, ASTM D 5379, was expanded using the DIC technique. The V-notched test method loading conditions and specimen design is detailed in Ref. [41] and ASTM D 5379 [42]. The test fixture, developed by Adams and Walrath [41], and specimen schematic is shown in Figure 4-1. The conventional material orientation is used for these tests where the 0° unidirectional composite has fibers oriented in the x direction, perpendicular to the rails, and a 90° unidirectional composite has fibers oriented in the y direction, parallel to the rails. This test method can be used to measure both in-plane and interlaminar shear properties of composite materials. The V-notch test method attempts to achieve a state of pure shear stress of the test cross section by applying two counteracting force couples. The average shear stress along the cross section between the supports is approximated using the following simple equation

$$\sigma_{xy} = \frac{P}{A}, \quad A = wt \quad (32)$$

where w is the width of the specimen through the cross section of the two notches and t is the thickness of the V-notch specimen. Analysis of the V-notch test method shows a state of uniform shear stress in the center of this cross section, but not in the region close to the notches [43, 44]. The normal stresses are found to be negligible throughout this cross section.

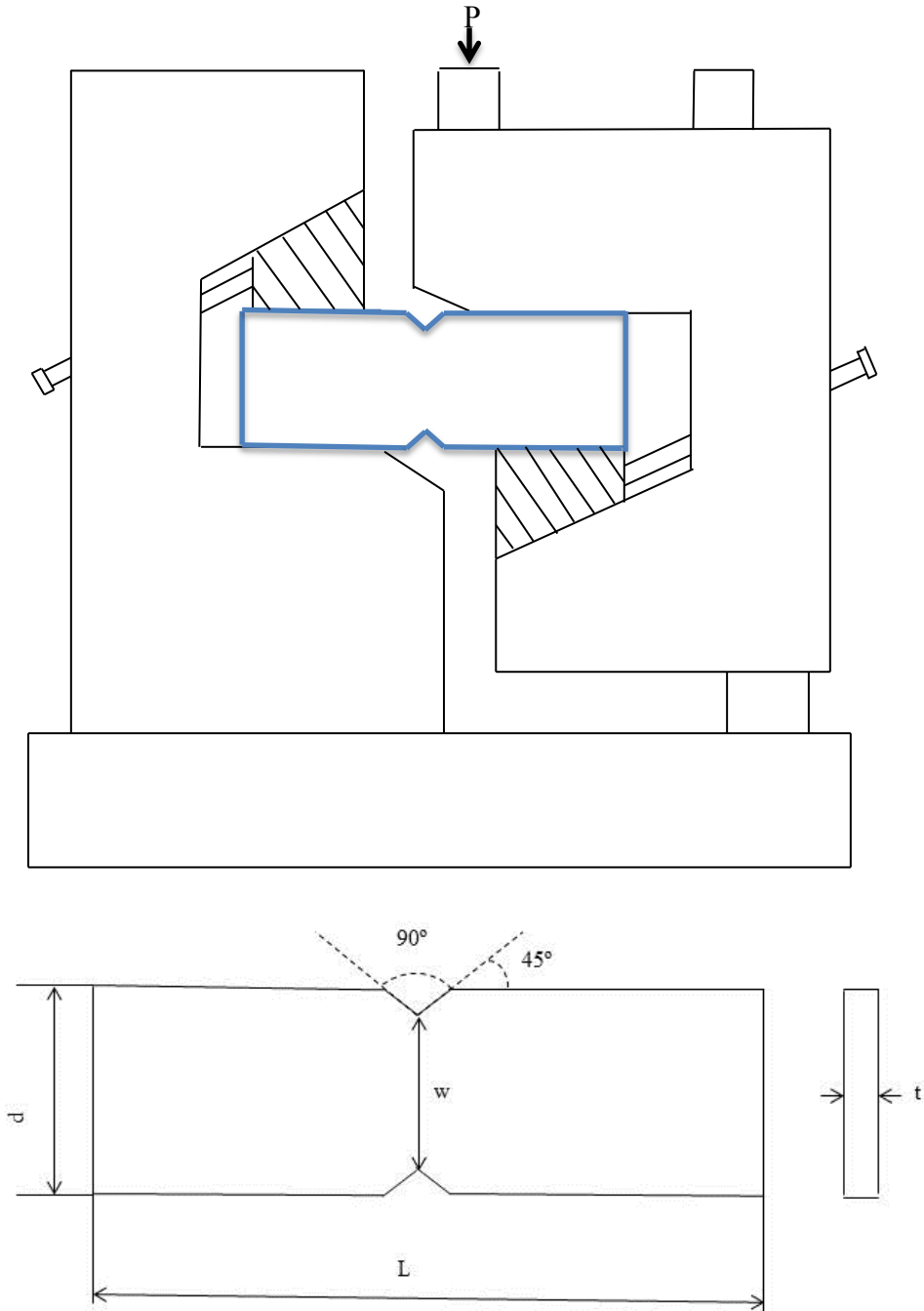


Figure 4-1 V-notch test fixture and specimen dimensions

The specimens were monotonically loaded at a 1.3 mm/min (.05 in/min) rate using a hydraulic testing machine. A random speckle pattern was applied to the surface of each specimen. The DIC Vic 3D system was used for strain calculations based on images obtained at a 1 Hz frequency using a 16 MP stereo camera system. Each specimen was analyzed using a subset window size of 21x21 pixels, corresponding to an approximate area of .0004 in² (.26 mm²) for SBS specimens. Displacement vectors were analyzed on 5 pixel centers, resulting in roughly 14,000 data points for SBS tests. The displacement measurements were then numerically differentiated over a local neighborhood using a 15x15 array of points applied to a strain algorithm in VIC-3D software in order to compute the Lagrange strain tensor [29]. Shear strain is averaged through a line of length equal to half the width between the two notches. Close to uniform stress and strain distributions allows for average values to be used within the gage region.

4.1.1 Experimental Results IM7-carbon/8552-epoxy

A set of ten IM7-carbon/8552-epoxy unidirectional composite V-notch coupons were tested in both the 0° and 90° to obtain both in-plane and interlaminar shear stress-strain behavior. Highly nonlinear shear stress-strain behavior was observed for specimens tested in the 0° plane. The nonlinear interlaminar shear stress-strain data was fit to the Ramberg Osgood Eq. (4) using a least squares approximation. A comparison between the average (1-3) interlaminar shear stress-strain responses measured for IM7-carbon/8552-epoxy using both SBS tests using (19) for the maximum shear stress approximation and V-notch tests is shown in Figure 4-2. Updated shear properties for the SBS tests, using (30) for maximum shear stress approximation, were used for the average values plotted in Figure 4-3. The interlaminar shear properties measured for the

V-notch specimens are listed in Table 4-1. The 90° V-notch specimens failed at low strain levels while still in the linear elastic regime. Figure 4-4 shows the shear stress-strain responses for each of these five specimens. The shear properties measured for these specimens are listed in Table 4-2.

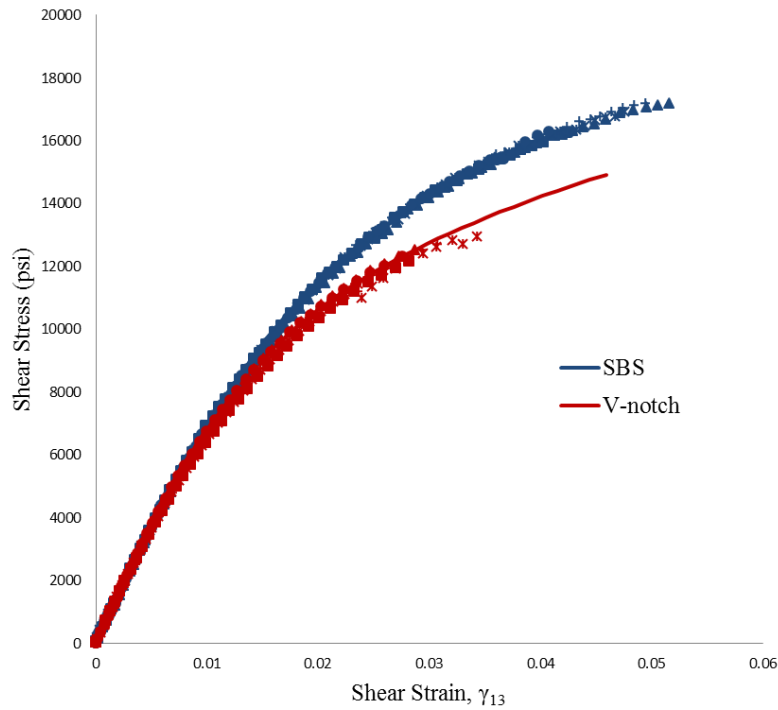


Figure 4-2 Comparison of average measured interlaminar (1-3) shear stress-strain response from the SBS using beam theory (19) stress approximation and the V-notch test for IM7-carbon/8552-epoxy unidirectional composite tape

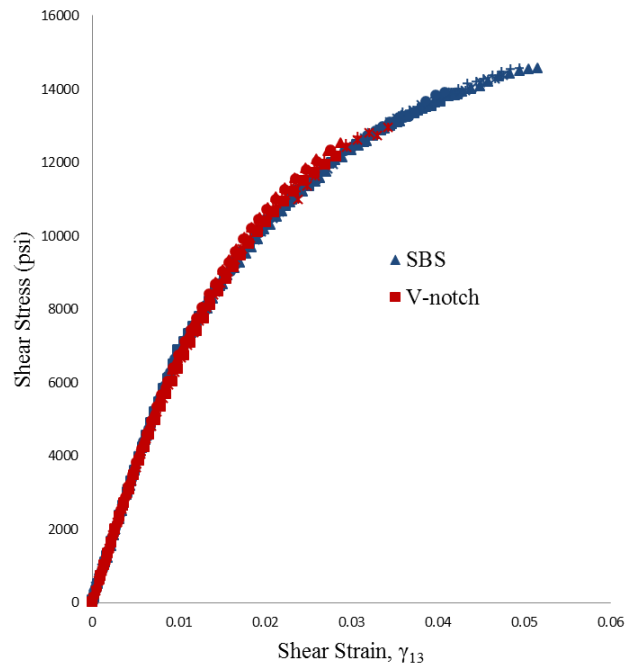


Figure 4-3 Comparison of average measured interlaminar (1-3) shear stress-strain response from the SBS test using bilinear (30) stress model and the V-notch test for IM7-carbon/8552-epoxy unidirectional composite tape

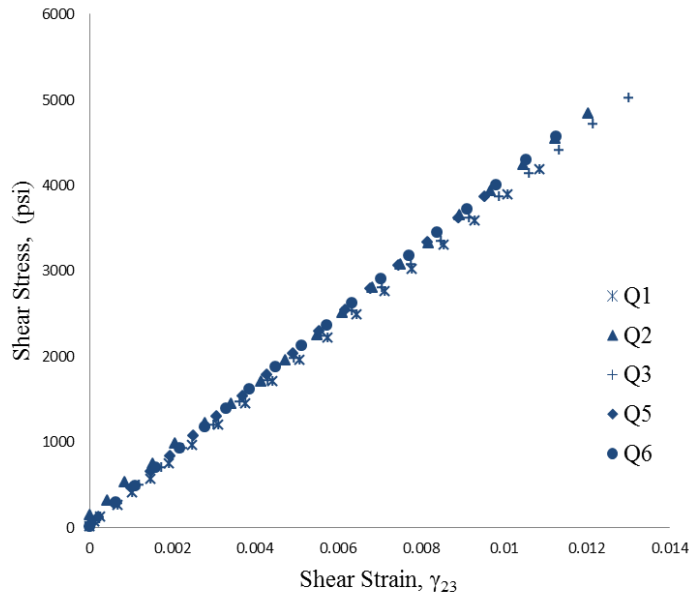


Figure 4-4 In-plane shear stress-strain response for IM7-carbon/8552-epoxy unidirectional tape V-notch specimens in the (2-3) material plane

Results, seen in both Figure 4-3 and Table 4-1, show that the interlaminar shear stress-strain parameters measured using the V-notch test are very consistent with the parameters obtained from the developed SBS test method using the bilinear stress model (30) for the maximum shear stress approximation. Interlaminar shear strength was not obtained from the V-notch tests for IM7-carbon/8552-epoxy unidirectional composites in the (1-3) material plane, due to premature failure at the notch roots resulting from stress concentrations which can be caused by geometric discontinuities commonly found in V-notch specimens [44]. The average linear shear modulus in the (2-3) material plane, measured from the 90° V-notch tests, is also consistent with SBS measurements.

Table 4-1 IM7-carbon/8552-epoxy unidirectional V-notch interlaminar (1-3) shear parameters

Specimen	t mm (in)	w mm (in)	G_{13} GPa (msi)	K_{13} GPa (ksi)	n_{13}
1	11.7 (.462)	2.8 (.112)	4.92 (.714)	.23 (33.4)	.22
2	11.8 (.464)	2.9 (.113)	5.18 (.752)	.23 (33.2)	.22
3	11.7 (.461)	2.9 (.113)	4.95 (.718)	.21 (30.8)	.20
4	11.7 (.463)	2.8 (.112)	5.07 (.735)	.24 (35.0)	.23
5	11.7 (.461)	2.8 (.112)	5.20 (.754)	.25 (35.6)	.23
AVG	11.7 (.462)	2.8 (.112)	5.06 (.735)	.23 (33.6)	.22
COV	.26%	.58%	2.6%	5.6%	5%

Table 4-2 IM7-carbon/8552-epoxy unidirectional V-notch in-plane (2-3) shear parameters

Specimen	t mm (in)	w mm (in)	G_{23} GPa (msi)
Q1	11.6 (.4585)	2.8 (.1105)	2.65 (.385)
Q2	11.8 (.463)	2.8 (.1085)	2.69 (.391)
Q3	11.8 (.4635)	2.9 (.1125)	2.68 (.388)
Q5	11.7 (.4625)	2.8 (.1115)	2.79 (.405)
Q6	11.7 (.46)	2.8 (.11)	2.79 (.404)
AVG	11.7 (.4615)	2.8 (.1106)	2.72 (.395)
COV	.47%	1.37%	2.3%

4.1.2 Experimental Results E-glass/5216-epoxy

A set of twenty E-glass/5216-epoxy unidirectional composite V-notch coupons were tested in the 0° to verify the interlaminar shear stress-strain properties measured using the SBS test and listed in Table 3-4. Full field strain calculations were obtained on the surface of each specimen from the same DIC technique utilized by the carbon/epoxy V-notch specimens. Test results for ten of the specimens were discarded due to

excessive twisting. Highly nonlinear shear stress-strain behavior was observed above 1% shear strain. The nonlinear interlaminar shear stress-strain data was fit to the Ramberg Osgood Eq. (4) using a least squares approximation. Figure 4-5 shows the interlaminar shear stress-strain response of E-glass/5216-epoxy unidirectional composites measured from each V-notch specimen along with each SBS specimen for comparison purposes. The interlaminar shear properties measured for the V-notch specimens are listed in Table 4-3 along with the average and covariance of the results.

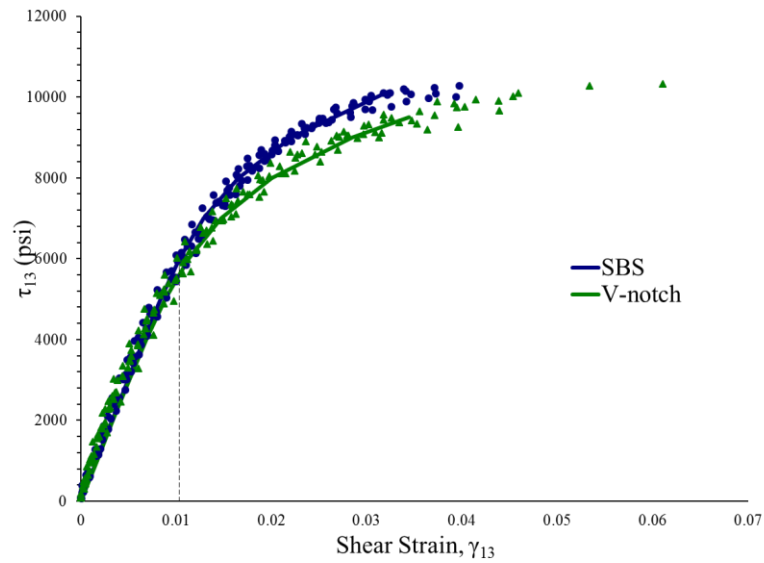


Figure 4-5 Comparison of interlaminar shear stress-strain response from the SBS test method using beam theory (4) stress approximations and the V-notch test for E-glass/5216-epoxy unidirectional composite tape

Table 4-3 E-glass/5216-epoxy unidirectional V-notch interlaminar (1-3) shear parameters

Specimen	t mm (in)	w mm (in)	G_{13} GPa (msi)	K_{13} GPa (ksi)	n_{13}
V7	13.2 (.5195)	2.5 (.0995)	4.41 (.640)	.122 (17.6)	.15
V8	13.1 (.5155)	2.5 (.0985)	4.44 (.643)	.117 (16.9)	.14
V10	13.1 (.5175)	2.5 (.1)	4.17 (.604)	.111 (16.1)	.13
V11	13.2 (.519)	2.5 (.097)	3.79 (.550)	.109 (15.8)	.13
V12	13.1 (.517)	2.5 (.0985)	3.84 (.557)	.111 (16.2)	.13
V14	13.1 (.515)	2.5 (.099)	3.53 (.512)	.111 (16.1)	.13
V15	13.1 (.515)	2.4 (.0945)	4.07 (.591)	.126 (18.3)	.16
V16	13.1 (.5175)	2.3 (.0915)	4.12 (.597)	.109 (15.8)	.13
V18	12.7 (.501)	2.5 (.1)	4.03 (.585)	.116 (16.8)	.15
V20	13.1 (.516)	2.3 (.0895)	4.28 (.621)	.129 (18.8)	.17
AVG	13.1 (.5153)	2.8 (.0968)	4.07 (.590)	.116 (16.8)	.14
COV	1.02%	3.53%	7%	10%	6%

SBS shear interlaminar shear measurements, listed in Table 3-4, and V-notch interlaminar shear measurements, listed in Table 4-3, for E-glass/5216-epoxy show consistent linear shear modulus values, but inconsistent nonlinear shear parameters. Referring to Figure 4-5 it can be observed that the SBS measured shear stress-strain response deviates from the V-notch measured shear stress strain response in the nonlinear shear regime reaching a maximum difference of 9% close to failure. Table 3-4 lists the updated nonlinear shear parameters and strength values measured for E-glass/5216-epoxy unidirectional composite tape using the SBS test method and replacing the closed form solution Eq. (19) with the bilinear stress model, Eq. (30), for maximum shear stress approximations.

Table 4-4 Updated shear results for SBS E-glass/5216-epoxy unidirectional composite tape specimens using the bilinear model Eq. (30)

Specimen	K_{13} GPa (ksi)	n_{13}	S_{13} MPa (ksi)
SBE 1	.101 (14.7)	.12	64.9 (9.42)
SBE 2	.102 (14.8)	.12	64.8 (9.40)
SBE 4	.107 (15.5)	.12	61.5 (8.93)
SBE 5	.109 (15.8)	.14	63.0 (9.14)
SBE 6	.107 (15.5)	.13	63.7 (9.24)
AVG	.105 (15.2)	.12	63.6 (9.22)
COV	3.2%	6.8%	2.2%

Table 4-4 shows that the interlaminar shear stress-strain response measured using the V-notch test are very consistent with the response measured using the developed SBS test method when the bilinear stress model (30) is employed for the maximum shear stress approximation. The interlaminar shear stress-strain response of E-glass/5216-epoxy unidirectional composites measured from each V-notch specimen and each SBS specimen, using the bilinear stress model (30) for maximum shear stress approximation, is shown in Figure 4-6.

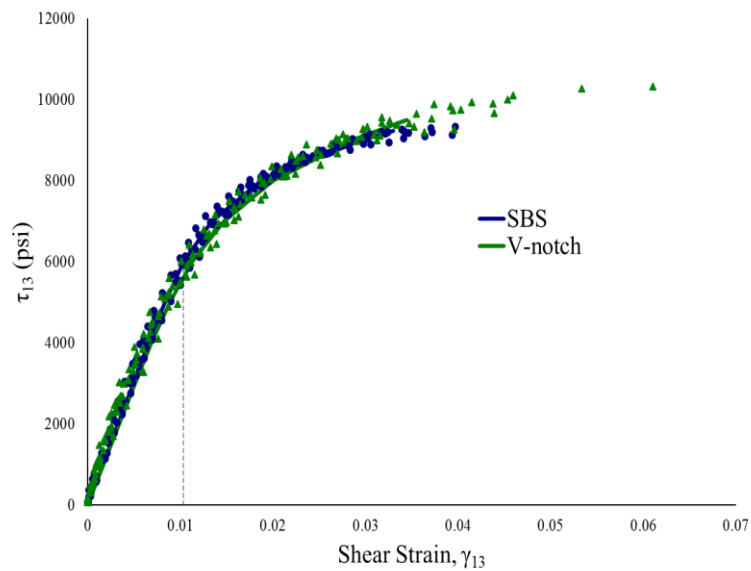


Figure 4-6 Comparison of interlaminar shear stress-strain response from the SBS test method using the bilinear model (30) for shear stress approximations and the V-notch test for E-glass/5216-epoxy unidirectional composite tape.

Interlaminar shear strength was not obtained from the V-notch tests for the same reason as the carbon/epoxy V-notch tests. Using the bilinear model (30) for the maximum interlaminar shear stress approximations good agreement was reached between the SBS and V-notch measurements.

4.2 Four Point Bending Tests

To verify the accuracy of axial tensile and compressive moduli results measured from the SBS test method a set of ten S2-glass/E773-epoxy unidirectional tape composite four point bending (FPB) specimens were tested in the (1-3) and (1-2) material plane. In addition, to confirm the large difference in axial compressive and tensile modulus values measured for carbon/epoxy material systems, a set of five IM7-carbon/8552-epoxy unidirectional composite FPB specimens were tested in the (1-3) material plane. The FPB test method is outlined in ASTM D 7264 [45]. Changes to the standard test configuration were made by decreasing the distance between the top supports in order to reduce the shear stress in the specimen and eliminate the possibility for shear delamination. The tests were run with a lower support span of 4 in. (101.6 mm) and an upper support span of 1 in. (25.4 mm). Each specimen had a square cross section with a .25 in. (6.35 mm) thickness and .25 in. (6.35 mm) width. All glass/epoxy specimens were cut from the same 26-ply unidirectional S2-glass/E773 composite tape panel and all carbon/epoxy specimens were cut from the same 35 ply unidirectional IM7-carbon/8552-epoxy composite tape panel. Specimens were machined at a length of 4.5 in. (114.3 mm). Each specimen was statically loaded using a hydraulic load frame at the same rate used in the short beam shear test method, 1.3 mm (.05 in)/min. DIC Vic 3D software [29] was used for strain calculations based on images obtained at a 3 Hz frequency using a 16 MP stereo camera system. Each specimen was analyzed using a subset window size of 35x35 pixels, corresponding to an approximate area of 0004 in² (.26 mm²) for FPB specimens. Displacement vectors were analyzed on 7 pixel centers, resulting in roughly 17,000 data points for each specimen. The displacement measurements were then numerically differentiated over a local neighborhood using a 15x15 array of points applied to a strain algorithm in VIC-3D software in order to compute

the Lagrange strain tensor. Compressive failure under the loading nose was observed for each specimen. The loading schematic and test geometry is shown in Figure 4-7.

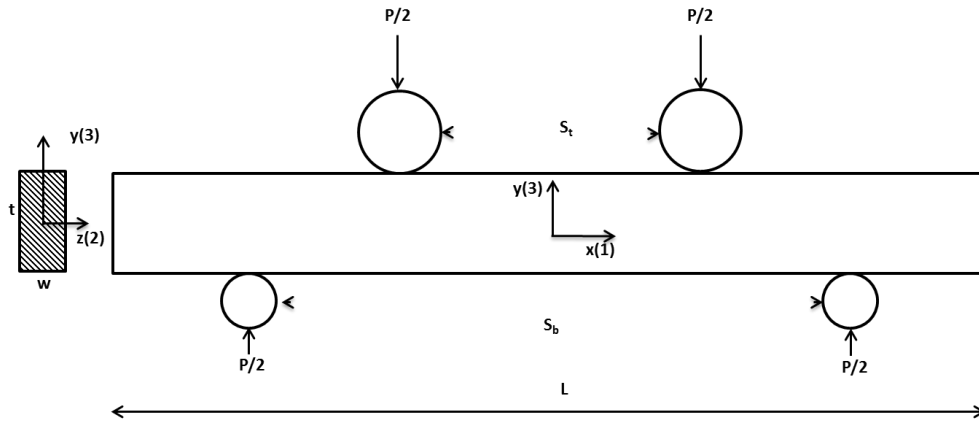


Figure 4-7 Test configuration and geometry of the four point bending test

This test method is well-suited for acquiring reliable axial normal tensile and compressive moduli results because of the pure bending in the center region of the specimen resulting in a zero shear state in this region and constant axial state along the x axis. In addition, without the presence of shear strains the axial strain distribution is no longer sensitive to small misalignments between the coordinate axes of the specimen and the DIC system. The closed form solution Eq. (13) can be used to approximate the axial tensile and compressive modulus in FPB specimens, where the bending moment, M , is equal to half the applied load, P , multiplied by the distance between top and bottom rollers on one side. Also, the axial strains do not need to be normalized with respect to the central cross section since the axial stresses should remain constant along the x axis in region far from the loading noses. Figure 4-8 shows a typical full field axial strain distribution for a four point bending S2-glass/E773-epoxy specimen close to failure load. Indeed, linear axial strain distributions are observed till failure.

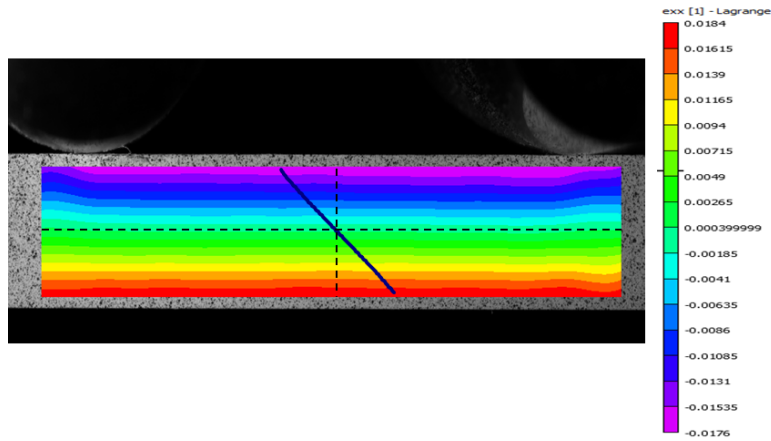


Figure 4-8 Typical axial strain distribution for S2-glass/E773 epoxy FPB specimen at 95% failure load in the (1-3) principal material plane

4.2.1 Experimental Results for S2-glass/E773-epoxy

Eq. (13) is used to determine the axial tensile and compressive moduli for each FPB specimen, the results are listed in Table 4-5 for S2-glass/E773-epoxy specimens tested in the (1-3) principal material plane and Table 4-6 for S2-glass/E773-epoxy specimens tested in the (1-2) principal material plane. No transformations were necessary for the data acquired from these tests.

Table 4-5 S2-glass/E773-epoxy Tensile and Compressive Moduli results for Four Point

Bending Tests tested in the (1-3) material plane

Specimen	T mm(in)	W mm(in)	E_{11T} GPa (msi)	E_{11} GPa (msi)	E_{11C} GPa (msi)	ν_{13}
1	6.1 (.2385)	6.4 (.2505)	45.2 (6.56)	45.3 (6.57)	4.54 (6.59)	.29
2	6.1 (.2385)	6.3 (.249)	45.3 (6.57)	45.9 (6.66)	4.65 (6.75)	.28
3	6.1 (.2385)	6.3 (.249)	45.9 (6.65)	46.0 (6.67)	4.61 (6.69)	.28
4	6.1 (.24)	6.3 (.2485)	44.9 (6.51)	45.5 (6.60)	4.61 (6.68)	.28
5	6.11 (.2405)	6.3 (.249)	46.1 (6.68)	45.7 (6.63)	4.53 (6.57)	.28
AVG	6.1 (.2392)	6.3 (.2492)	45.5 (6.60)	45.7 (6.63)	4.59 (6.66)	.28
COV	.4%	.3%	1%	.6%	1%	3%

Table 4-6 S2-glass/E773-epoxy Tensile and Compressive Moduli results for Four Point

Bending Tests tested in the (1-2) material plane

Specimen	T mm(in)	W mm(in)	E_{11T} GPa (msi)	E_{11} GPa (msi)	E_{11C} GPa (msi)	ν_{12}
6	6.3 (.2495)	6.1 (.239)	45.1 (6.54)	45.4 (6.58)	45.6 (6.62)	.28
7	6.3 (.249)	6.1 (.2385)	45.2 (6.55)	45.6 (6.62)	46.2 (6.70)	.28
8	6.3 (.2485)	6.2 (.2435)	43.0 (6.23)	44.7 (6.49)	46.6 (6.76)	.28
9	6.3 (.2485)	6.1 (.242)	42.9 (6.22)	43.9 (6.37)	45.0 (6.53)	.28
10	6.3 (.2495)	6.1 (.2405)	45.1 (6.54)	44.8 (6.50)	44.5 (6.45)	.28
11	6.3 (.248)	6.2 (.2445)	44.3 (6.43)	45.3 (6.57)	46.3 (6.72)	.28
AVG	6.3 (.2488)	6.1 (.2413)	44.3 (6.42)	45.0 (6.52)	45.7 (6.63)	.28
COV	.2%	1%	1%	1.4%	1.8%	0%

The measured tensile modulus values for S2-glass/E773-epoxy are very similar to the compressive modulus values in the corresponding directions, showing that the average modulus can accurately describe both the tensile and compressive properties of the material system. Both the tensile and compressive moduli show low variability and correlate well with measurements from the SBS measurements for S2-glass/E773-epoxy material system.

4.2.2 Experimental Results for IM7-carbon/8552-epoxy

For carbon/epoxy material systems a higher difference is expected between the tensile and compressive modulus values. The measured tensile and compressive modulus values for IM7-carbon/8552-epoxy four point bending tests are listed in Table 4-7.

Table 4-7 IM7-carbon/8552-epoxy Tensile and Compressive Moduli results for Four Point Bending Tests

Specimen	E_{11T} GPa (msi)	E_{11C} GPa (msi)
1	163.4 (23.7)	141.3 (20.5)
2	157.2 (22.8)	146.2 (21.2)
3	171.0 (24.8)	141.3 (20.5)
4	166.2 (24.1)	144.1 (20.9)
5	161.3 (23.4)	147.5 (21.4)
AVG	164.1 (23.8)	144.1 (20.9)
COV	3.11%	2.10%

Both the tensile and compressive moduli show low variability and correlate well with the axial normal tensile and compressive properties for IM7-carbon/8552-epoxy provided by the prepreg manufacturer [36] as well as the axial tensile and compressive modulus measurements from the SBS test method in Table 3-5.

4.3 Curved Beam Test

To verify the accuracy of the short-beam shear method to capture the interlaminar tensile (ILT) modulus, the ASTM Standard D 6415 curved-beam test method [46] is also expanded using the DIC technique. ASTM D 6415 is limited to measurement of the ILT strength. Complexity of the strain state including strong gradients in the curved-beam coupons prohibits the use of electrical strain gages for modulus characterization. The ILT modulus data will be generated for the IM7-carbon/8552-epoxy tape composite based on the curved-beam tests employing the DIC technique; and compared with the short-beam based values. The test configuration and specimen geometry for the curved beam is shown in Figure 4-9.

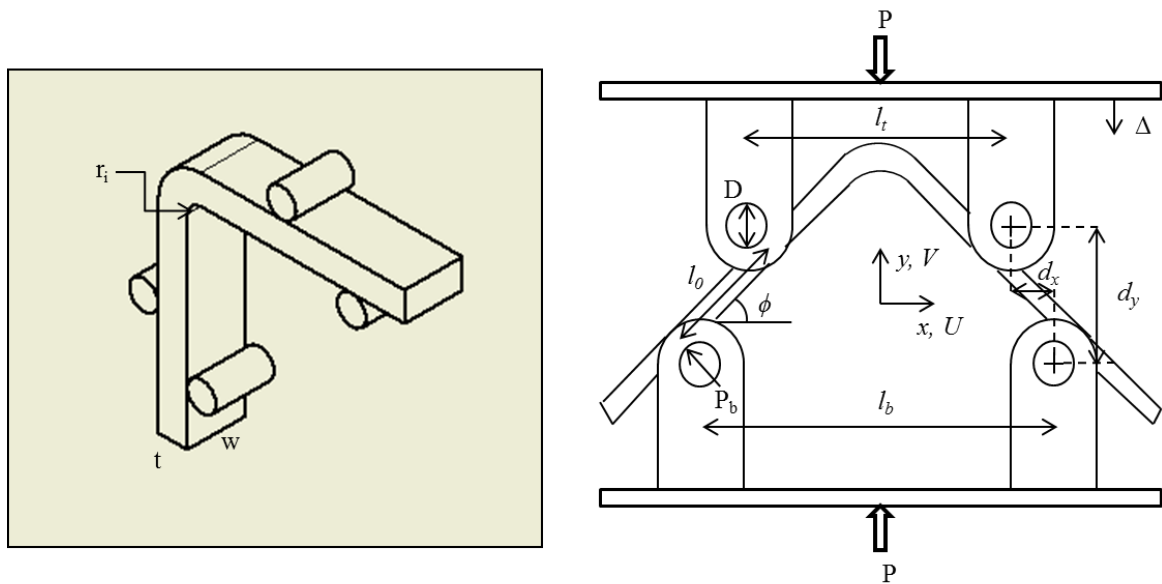


Figure 4-9 Curved beam geometry and schematic of a curved beam under four point bending

The curved beam test measures the curved beam strength for continuous fiber reinforced composites by applying a constant bending moment in the center of a 90° curved beam loaded under four point bending. For unidirectional composites with fibers

that run along the legs and around the curved portion of the specimen the ILT strength can be measured when appropriate failure is observed. The curved beam strength is a representation of the moment per unit width required for delamination and can be calculated using the following equation

$$CBS = \frac{M}{w} \quad (33)$$

where w is the width of the specimen and M is the bending moment applied to the center of the specimen. The applied bending moment on the center section of the curved beam is the product of the applied force, P_b , exerted by one of the loading bars and the distance between two bars on the same leg, l_0

$$M = P_b l_0 \quad (34)$$

From force equilibrium and the geometry of the loading fixture and specimen we have

$$P_b = \frac{P}{2 \cos(\phi)} \quad (35)$$

and

$$l_0 = \frac{d_x}{\cos(\phi)} + (D + t) \tan(\phi) \quad (36)$$

where P is the applied load, ϕ is the angle in degrees between the horizontal and the loading arm, d_x is the horizontal distance between two of the top and bottom rollers $(l_b - l_t)/2$, D is the diameter of the rollers, and t is the specimen thickness.

The angle, ϕ , between the horizontal and loading arm can change significantly during loading. For more accurate measurements ϕ should be calculated during loading. To determine ϕ during loading the vertical distance between rollers, d_y , must be measured during loading as well. This can be determined by subtracting the vertical crosshead displacement, Δ , from the initial value of d_y obtained from Eq. (37).

$$d_y = d_x \tan(\phi_i) + \frac{D+t}{\cos(\phi_i)} - \Delta \quad (37)$$

The vertical crosshead displacement, Δ , is a measurement that can be outputted from the loading machine or a displacement gage. The initial angle, ϕ_i , is half the overall angle between the loading arms of the specimen before loading. Based on geometric relations this angle can be calculated for a given value of d_y using the following equation

$$\phi = \sin^{-1} \left(\frac{-d_x(D+t) + d_y \sqrt{d_x^2 + d_y^2 - D^2 - 2Dt - t^2}}{d_x^2 + d_y^2} \right) \quad (38)$$

All other parameters in Eq. (38) remain fixed under loading.

Closed form solutions for interlaminar tensile strength of curved beams with cylindrical anisotropy were derived in Ref. [35]. The radial stress is given in Eq. (39) for a curved beam under pure bending. Since this segment is subject to pure bending the radial stresses in this region are independent of angular position.

$$\sigma_{rr} = -\frac{CBS}{r_0^2 g} \left[1 - \frac{1-p^{k+1}}{1-p^{2k}} \left(\frac{r_m}{r_0} \right)^{k-1} - \frac{1-p^{k-1}}{1-p^{2k}} p^{k+1} \left(\frac{r_0}{r_m} \right)^{k+1} \right] \quad (39)$$

where

$$g = \frac{1-p^2}{2} - \frac{k}{k+1} \frac{(1-p^{k+1})^2}{1-p^{2k}} + \frac{kp^2}{k-1} \frac{(1-p^{k-1})^2}{1-p^{2k}}, k = \sqrt{\frac{E_\theta}{E_r}}, p = \frac{r_i}{r_o} \quad (40)$$

and

$$r_m = \left[\frac{(1-p^{k-1})(k+1)(pr_o)^{k+1}}{(1-p^{k+1})(k-1)r_o^{-(k-1)}} \right]^{\frac{1}{2k}} \quad (41)$$

where r_m is the radius of the location of approximation and r_i and r_o are the inner and outer radius of the specimen. This model for maximum radial stress is quite complicated. A simpler model for maximum radial stress in a curved beam was developed in Ref. [47]. This simpler model is developed from classical beam theory and is based on the assumption that the location of maximum radial stress occurs at the location:

$$r_m = \sqrt{r_o r_i} \quad (42)$$

The maximum radial stress in the curved beam can be approximated using the following equation

$$\sigma_r^{\max} = \frac{3CBS}{2t\sqrt{r_i r_o}} \quad (43)$$

This equation becomes less accurate as the ratio E_θ/E_r , approximately E_{xx}/E_{yy} in the flatwise panels, increases or the ratio r_i/r_o decreases. For curved beam specimens with the ASTM recommended geometry and an E_θ/E_r ratio less than 20 this approximation (43) results in less than 2% error [46].

A set of six 26-ply thick unidirectional IM7-carbon/8552-epoxy curved-beam coupons was manufactured following the ASTM D 6415 specifications [46]. The coupons were 6.6 mm (0.26 in) thick, and 25.4 mm (1 in) wide.

Figure 4-10 shows a curved-beam test setup. The coupons were placed in a standard ASTM D 6415 test fixture [46]; and loaded in an electromechanical load frame at a constant 0.05 in/min crosshead displacement rate till failure. The tests were conducted at 72° F room-temperature ambient conditions. The failure mode was tensile delamination which started in the beam radius area at about 60% of the thickness

corresponding to the maximum ILT stress location [46] and quickly propagated through the beam flanges. All curved-beam coupons exhibited similar behavior.

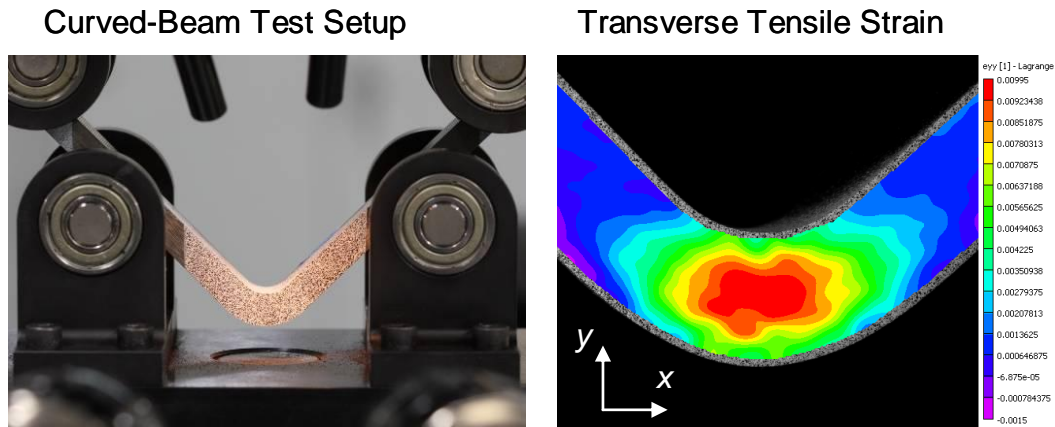


Figure 4-10 A curved-beam test setup and the DIC measured transverse tensile strain distribution right before delamination failure

Figure 4-10 also shows typical transverse tensile surface strain captured right before failure using the DIC technique. Surface strains in the curved-beam coupons were assessed with the VIC-3D software [29] using a 45x45 pixel subset size corresponding to a 0.465 mm² area. Data was obtained on 9 pixel centers, resulting in roughly 7,000 data points per load case. The parameters defined in VIC-3D analysis are determined on an individual test basis and are based on several testing parameters including the size of the specimen, resolution of the cameras, speckle pattern, and magnification level. Different parameters were chosen for the curved beam tests which resulted in a similar number of data points compared with the SBS tests. However, running the analysis on the curved beam specimens with the same input parameters

including 31×31 pixel subset and 7 pixel step sizes used for the SBS tests results in less than a 2% difference in the measured tensile and compressive moduli.

Figure 4-11 shows the ILT stress-strain response for the curved-beam coupons. The symbols in the stress-strain plots correspond to the individual data points captured till delamination failure onset. Each data point includes a DIC based ILT strain value and an independently calculated closed-form stress approximation (43). The ILT stresses and strains are tied through the load measurements. The DIC based ILT strain corresponding to each data point is the maximum transverse strain in the center cross-section (symmetry plane) of the curved-beam coupon. And the ASTM D 6415 provides the closed-form geometric (material-independent) approximation of the maximum ILT stress derived using a beam theory [35, 47]. Figure 4-11 clearly indicates linear ILT stress-strain behavior. Slope of the stress-strain response represents the ILT modulus.

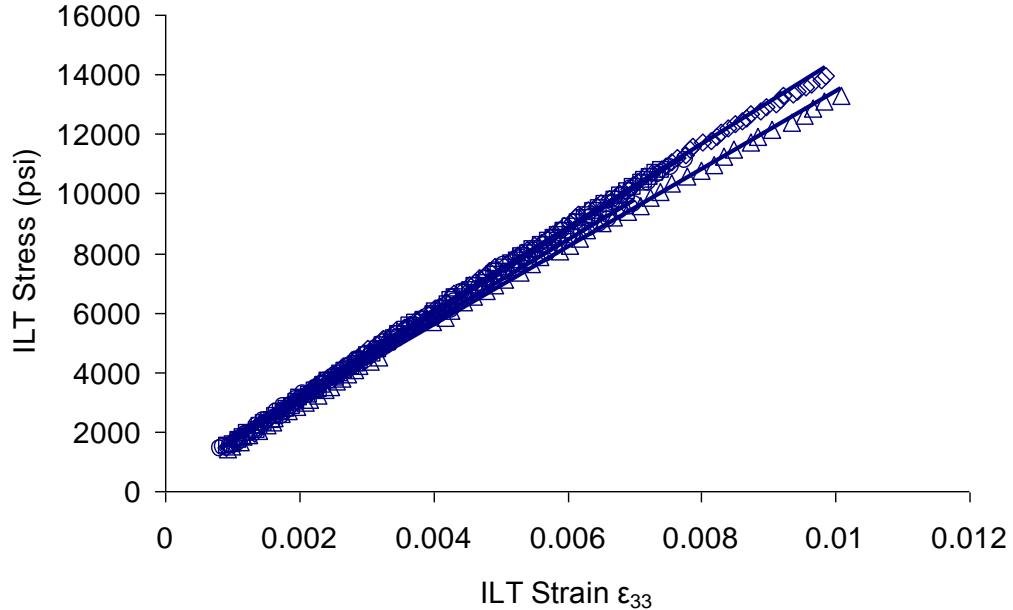


Figure 4-11 ILT stress-strain response of unidirectional curved-beam coupons CB1-CB6

Table 4-8 lists the ILT modulus measurements from the ASTM D 5416 curved-beam coupons. The average 9.52 GPa (1.38 msi) ILT modulus value is 4% lower compared to the ILT modulus value generated using the short-beam tests. The discrepancy could be attributed to the prepreg quality as well as variations in the manufacturing process as the subject curved-beam tests were accomplished approximately one year before the ILT short-beam tests.

Table 4-8 ILT modulus values measured using the first batch of unidirectional 25.4-mm (1-in) wide curved-beam coupons.

W 25.4 mm (1 in)	E_{33T} GPa (msi)
CB1	9.34 (1.35)
CB2	9.94 (1.44)
CB3	9.69 (1.40)
CB4	9.04 (1.31)
CB5	9.69 (1.41)
CB6	9.44 (1.37)
AVG	9.52 (1.38)
COV	3.35%

To reproduce the ILT modulus results, another batch of curved-beam coupons was manufactured and tested after the ILT short-beam tests were completed. The curved-beam coupon dimensions were identical to the previous batch; except the width was reduced from the ASTM D 6415 recommended 25.4 mm (1 in) to 12.7 mm (0.5 in) to machine 9 coupons from a single panel. The smaller width also improves the accuracy of

coupling between the DIC based surface strain and the beam-type stress approximations (43).

The test setup and the process to generate the ILT modulus values from the reduced-width coupons were identical to the regular ASTM D 6415 curved-beam coupons producing similar results. Table 4-9 lists the ILT modulus values generated from the new batch. The average 9.93 GPa (1.44 msi) ILT modulus value is almost identical to the 9.92 GPa (1.44 msi) short-beam result. Figure 4-12 shows the ILT stress-strain response for these curved-beam coupons. Larger scatter in the curved-beam test data is not surprising due to extreme sensitivity to the manufacturing quality as reported in the ASTM D 6415 [46].

Table 4-9 ILT modulus values measured using the second batch of unidirectional 12.7-mm (0.5-in) wide curved-beam coupons.

W 12.7 mm (0.5 in)	E_{33T} GPa (msi)
CB7	10.73 (1.56)
CB8	9.84 (1.43)
CB9	10.93 (1.59)
CB10	10.09 (1.46)
CB11	10.31 (1.49)
CB12	9.17 (1.33)
CB13	9.11 (1.32)
CB14	9.18 (1.33)
AVG	9.92 (1.44)
COV	7.25%

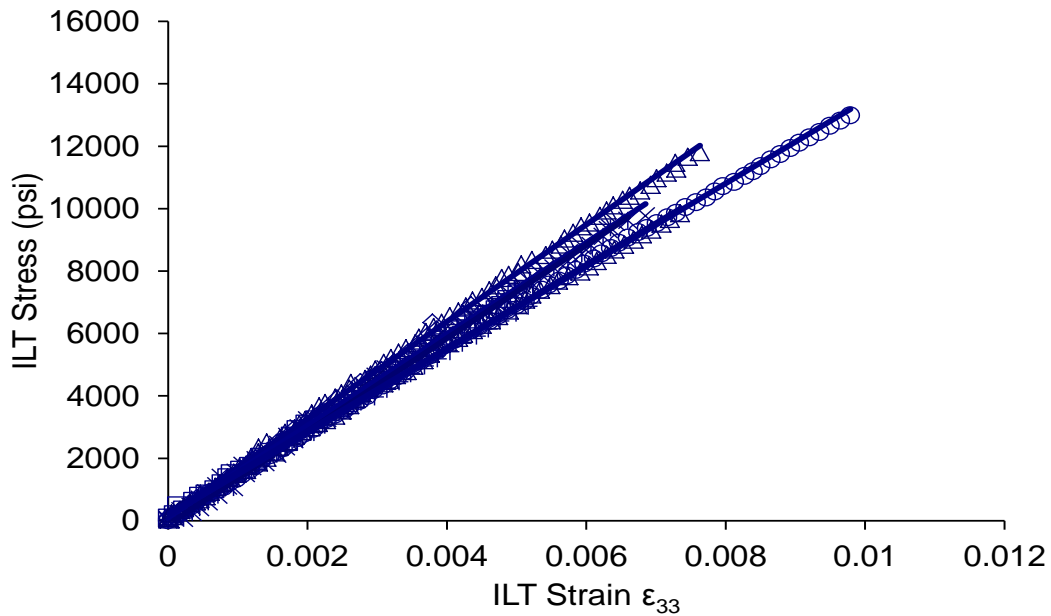


Figure 4-12 ILT stress-strain response of unidirectional curved-beam coupons CB7-CB14

4.4 Interlaminar Compressive Tests

To verify the interlaminar, E_{33C} , compressive modulus obtained from the SBS test method for IM7-carbon/8552-epoxy unidirectional composite tape a set of ten through-the-thickness compression tests were run. Each specimen was machined in the through-the-thickness (interlaminar) direction from a 106-ply thick IM7-carbon/8552-epoxy unidirectional tape panel cured at 350° F per prepreg manufacturer's specifications [36]. Specimens were placed in the center between two metal plates and statically loaded using a hydraulic load frame. The tests were conducted at 72° F room-temperature ambient conditions. Five specimens were thrown out due to non-uniform stress caused by taper. DIC Vic 3D software was used for strain calculations based on images obtained at a 1 Hz frequency using a 16 MP stereo camera system. Each specimen was analyzed using a subset window size of 35x35 pixels, corresponding to an approximate

area of 0006 in² (.39 mm²) for each specimen. Displacement vectors were analyzed on 7 pixel centers, resulting in roughly 14,000 data points for each specimen. The displacement measurements were then numerically differentiated over a local neighborhood using a 15x15 array of points applied to a strain algorithm in VIC-3D software in order to compute the Lagrange strain tensor. The specimen geometry and test configuration can be seen in Figure 4-13 along with a typical interlaminar compressive strain distribution at around 75% of the failure load. A nonlinear compressive interlaminar stress-strain response was observed for strains above 1.5%. Assuming the stresses are uniformly distributed over the cross section, the following equation can be used to approximate the interlaminar compressive stress in the specimen [8]

$$\sigma_{33} = \frac{P}{A}, \quad A = wt \quad (44)$$

where P is the applied load, and A is the undeformed cross sectional area of the specimen.

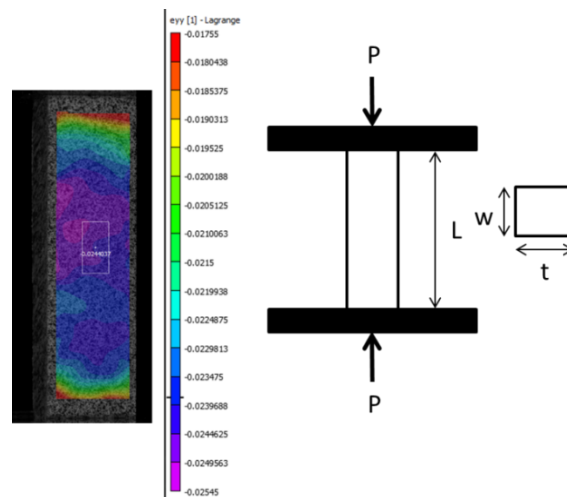


Figure 4-13 A compression test setup and typical DIC measured transverse compressive strain distribution

Uniform stresses and strains through the center of the specimen allow us to take the average interlaminar compressive strain in the center of the specimen. Figure 4-14 shows the interlaminar compressive stress-strain response for the compression specimens. The symbols in the stress-strain plots correspond to the individual data points captured till failure. Each data point includes a DIC based interlaminar compressive strain value and an independently calculated closed-form stress approximation (44).

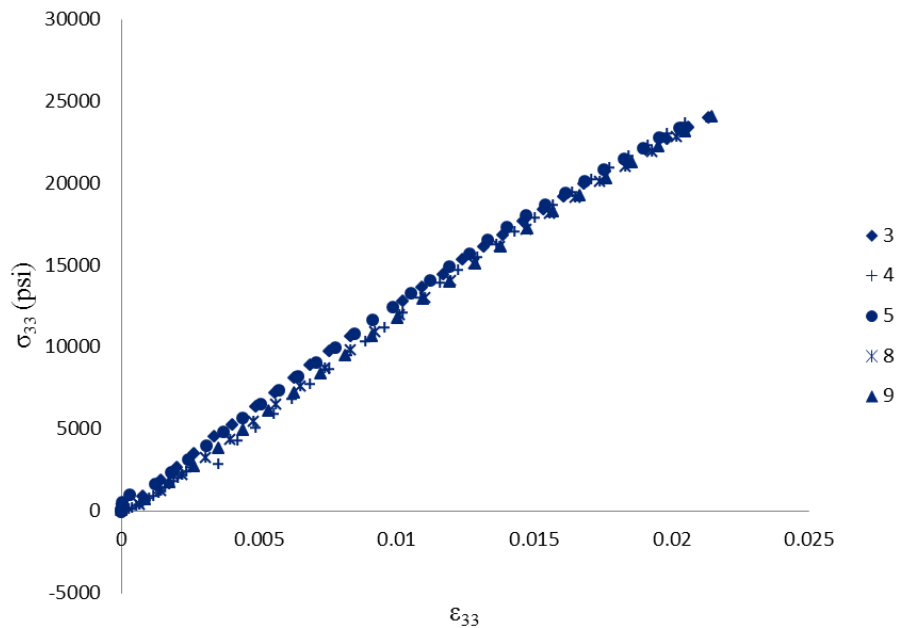


Figure 4-14 Interlaminar compressive stress-strain response for IM7-carbon/8552-epoxy short beams machined and loaded through the thickness direction

The interlaminar compressive modulus was measured from the slope of the stress-strain response in the linear regime, between 1,000 $\mu\epsilon$ and 6,000 $\mu\epsilon$. Table 4-10 lists specimen dimensions and measured interlaminar compressive modulus values for each of the five specimens tested.

Table 4-10 Interlaminar compressive modulus values measured using IM7-carbon/8552-epoxy thick panel composite beams machined and loaded in the thickness direction

Specimen	t mm (in)	w mm (in)	E_{33C} GPa (msi)
3	6.1 (0.239)	6.0 (0.237)	8.8 (1.28)
4	6.1 (0.239)	5.9 (0.2325)	8.9 (1.29)
5	6.2 (0.2425)	6.1 (0.2385)	8.7 (1.27)
8	5.2 (0.206)	5.8 (0.2285)	8.7 (1.26)
9	5.2 (0.205)	5.8 (0.2295)	8.4 (1.22)
AVG	5.6 (0.219857)	5.91 (0.232714)	8.7 (1.26)
COV	8.67%	1.60%	4.44%

The average value of 8.57 GPa (1.26 msi) for the interlaminar compressive modulus is within 5% of the average interlaminar compressive modulus values, 8.96 GPa (1.30 ms), generated from the SBS tests, also listed in Table 3-11.

Chapter 5

DIC Errors in SBS Testing

There are multiple ways for error to be introduced into the DIC deformation measurements and strain calculations. Errors in DIC deformation measurements and strain calculations can arise from a combination of both the experimental setup (speckle patterns, low resolution cameras, lighting, calibration errors, etc.) and analysis of the software (intensity interpolation methods, subpixel approximations, filtering, subset size, step size, subset shape functions, etc.). Basic rules have already been introduced to ensure minimal errors associated with speckle patterns and subset size. Experimental errors can be reduced with experience and knowledge of the test configuration and material system. Correct experimental setup and appropriate DIC input parameters can help reduce these errors.

Error introduced into the DIC measurements through subpixel approximations of the grayscale values is referred to as interpolation errors, while error introduced by Gaussian smoothing filter to the strain calculations is referred to in this work as filtering errors. Interpolation errors correspond to the subset matching process and appear in the displacement measurements, which can introduce noise to the strain calculations. Methods for quantifying subset matching errors have been outlined in studies by Schreier and Wang [30, 48]. Filtering errors occur in the strain calculation process in an attempt to reduce the noise from the deformation measurements, which can introduce even larger noise to the strain fields. The type and size of the filter applied can alter the strain distributions, mainly in areas of strong strain gradient. The following sections will approximate the errors caused by interpolation and filtering for a typical static SBS test. In addition, potential filtering errors in analysis of low velocity impact SBS tests will be

predicted for the maximum interlaminar shear strain of S2-glass/E773-epoxy unidirectional composite tape.

5.1 Interpolation Errors

Interpolation errors are errors introduced to the displacement field as a result of subpixel approximations. The magnitude of these errors is dependent on the type of interpolation function used along with subset size and experimental considerations such as speckle pattern. In order to reduce displacement errors caused by interpolation, Vic3D uses an optimized interpolation filter with the option of 4, 6, or 8 pixels of support [29]. In order to determine the interpolation errors that can be expected using this SBS test method a numerical study outlined by Schreier [30] was employed on a [300x300] pixel sample speckle pattern from an IM7/8552 SBS specimen seen in Figure 5-1.

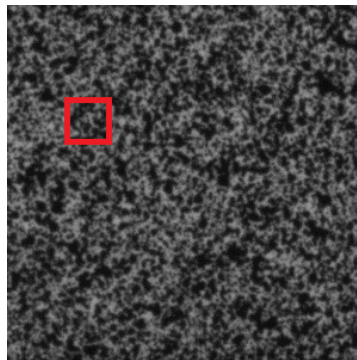


Figure 5-1 A 300x300 pixel sample of an IM7/8552 SBS specimen surface image used for interpolation error study with corresponding subset size

The sample used demonstrates a typical resolution and speckle pattern for static SBS tests. A set of 20 images were generated at .05 pixel increments. The images were then run through Vic2D software analysis using each interpolation option, all having the same subset size of 35x35 and step size of 7 to correspond with the parameters most

often used throughout this work. Figure 5-2 shows the interpolation error, Δu , at each true subpixel location, u_T .

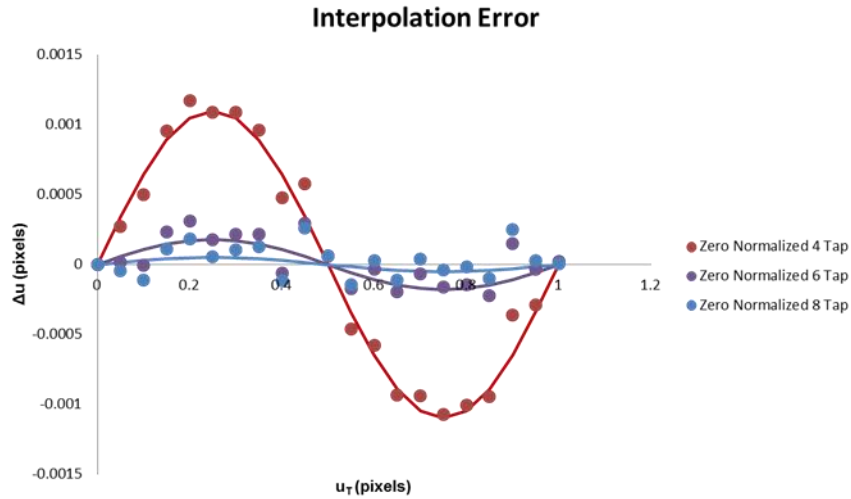


Figure 5-2 Interpolation bias as a function of subpixel location for different interpolation filters used in Vic3D/2D software analysis

Based on these results, an approximate maximum pixel error of .0011 is determined using an optimized 4 tap interpolation filter. The error is significantly reduced by increasing the support of the interpolation filter to 6. Little difference is observed between the optimized 6 and 8 tap filters. By switching to a 6 tap filter the maximum error that can be expected from interpolation is approximately .0002 pixels in displacement errors. This error translates to strain error by taking the gradient of the error curve for displacements. For the optimized 4 tap filter this corresponds to a maximum strain error of approximately .006 at the integer locations. This error reduces to a maximum of .001 strain error for the optimized 6 tap filter. Looking at the sinusoidal fit of the 8 tap data the gradient is very close to zero, introducing very little error to the strain calculations. All of these results indicate that there is little error introduced into the

data from interpolation for our tests. Still it is best to use the optimized 6 or 8 tap filters since a large reduction in maximum error is observed.

5.2 Filtering Errors

To calculate the strains, Vic3D, calculates the derivative of the displacement field over a local neighborhood of $n \times n$ data points, referred to as the strain window. A Gaussian smoothing filter is applied to the strain calculations. The idea behind Gaussian smoothing is to use the 2-D Gaussian distribution as a “point-spread” function, and this is achieved through convolution. Since each data point from FEM is a discrete value, the discrete approximation of the Gaussian distribution must first be determined before the convolution process. This can be computed in matlab using the `fspecial` function, specified for the Gaussian distribution. The sigma value designated in this function is the standard deviation of the filter. Theoretically the Gaussian distribution is non-zero everywhere, however, in practice it is effectively zero past three standard deviations. For this reason the standard deviation used in this study was $1/3$ the filter size. This method is used to smooth out the strain field reducing the noise that might appear from the displacement field. It is a non-uniform low pass filter, smoothing out areas of high spatial frequency. This is a concern for the SBS test method, since this might alter the strain values in regions of interest for our measurements, in particular the peak shear strain value in the region between loading nose and support might be artificially reduced due to the parabolic nature of the shear strain distribution.

5.2.1 Static Tests

To approximate the effect of the filter on the measurement of peak shear strain values in a typical glass/epoxy and carbon/epoxy SBS specimen a Gaussian filter was applied to FEM based strains of a SBS specimen at close to failure load using both

IM7/8552 material properties and S2/E773 material properties. Strain values were obtained from the right portion of the model between the supports and loading nose. In this region both the horizontal and vertical mesh are evenly distributed along the axis, resulting in a vertical distance of .11 mm (.0045 in) and a horizontal distance of .322 mm (.01267 in) between nodes. This correlates well for the density of the DIC data in the vertical direction, however, in the horizontal direction the strain data needs to be interpolated. Two points were created between each nodal point along the x axis of the FEM data. Linear interpolation was used for the axial normal strain distribution and an average of the nodal values was used for the shear strain distribution. Also, noise that might be introduced to the DIC displacement field was added to a designated number of strain values in order to determine if the filter size being used was large enough to sufficiently suppress the noise that could be present in a typical SBS test. Surface strains were extracted from each model in the 2 mm region equidistant between loading nose and support. The filter was applied to a .35 in (8.9 mm) region between supports consisting of approximately 4,500 data points. Strain distributions in a .079 in (2 mm) region between supports are compared with and without the filter, and with and without noise.

5.2.1.1 IM7-carbon/8552-epoxy

The strain distributions for IM7-carbon/8552-epoxy come from FEM for a 1.2 inch short beam specimen with a 1437 lb applied load, corresponding to an approximate peak shear stress of 14 ksi. Random noise was introduced to the strain values in the .079 in (2mm) gage region, with magnitudes between 0 and .002. This magnitude was approximated based off the sigma output from the Vic3D project file, which represents the confidence interval at each data point in pixels. This value can be converted into displacement error and used to estimate noise introduced into the strain data before

filtering. The magnitude of added noise is doubled for the shear strain to convert from Lagrangian strain to engineering strain. A 15x15 Gaussian filter is applied to the FEM based shear strain distribution in the center region between supports and loading nose. An additional 30x30 Gaussian filter is applied to the noise-free shear strain distribution to demonstrate the effect of larger filter sizes. Both the unfiltered and filtered distributions are shown in Figure 5-3 and Figure 5-4. The filtered interlaminar shear strain distribution using a 15x15 filter size has a slightly smaller maximum interlaminar shear strain value and artificially larger shear strain values close to the edges of the specimen, where the values should be close to zero. This distortion around the edges is an artifact caused by the Gaussian filter, referred to as an “edge effect”, and occurs at points that do not have enough data surrounding them to fit the size of the filter. An alternative filtering process is used by Vic3D analysis in these regions to account for this effect. A Gaussian filter acts as a low pass filter and is therefore expected to also decrease the maximum strain value for a strain distribution that varies parabolically. The unfiltered shear strain has a peak value of .0818 at this load. After the filtering process the peak shear strain drops by 1% of its original value. With added noise the peak strain value can vary around 5% of its total. Applying the same Gaussian filter to the FEM based strain distribution with added noise produces similar results. This indicates that the filter is large enough to effectively reduce noise of this magnitude in the shear strain distribution of a SBS test configuration, without appreciably reducing the maximum shear strain value. Larger filter sizes will produce greater deviations between maximum shear strain values. Increasing the filter window size to 30 produces an approximate 4% decrease in peak shear strain values after the filter is applied. Such filter sizes effectively produce errors in the peak shear strain value similar to maximum noise levels.

The axial strain distribution is shown in Figure 5-4. For unidirectional carbon/epoxy and glass/epoxy SBS tests loaded in the (1-3) material plane the peak axial strains are much smaller in comparison to the peak shear strains. Noise from the displacement data becomes more of a concern for the axial strain distribution in a three point bending configuration, where the relative magnitude is more significant. It is therefore important to have a filter large enough to minimize this noise. A Gaussian filter size of 15x15 successfully reduces the noise in the data, resulting in similar distributions from both the noise-free and noisy data. Even the larger filter size does not significantly alter the axial strain distribution in the central region of the specimen. Noticeable deviations in the filtered strain distributions are observed close to the edges of the data. Such “edge-effects”, caused by this type of filter, are not reflective of DIC analysis, which uses an alternative filter along the edges to reduce this effect.

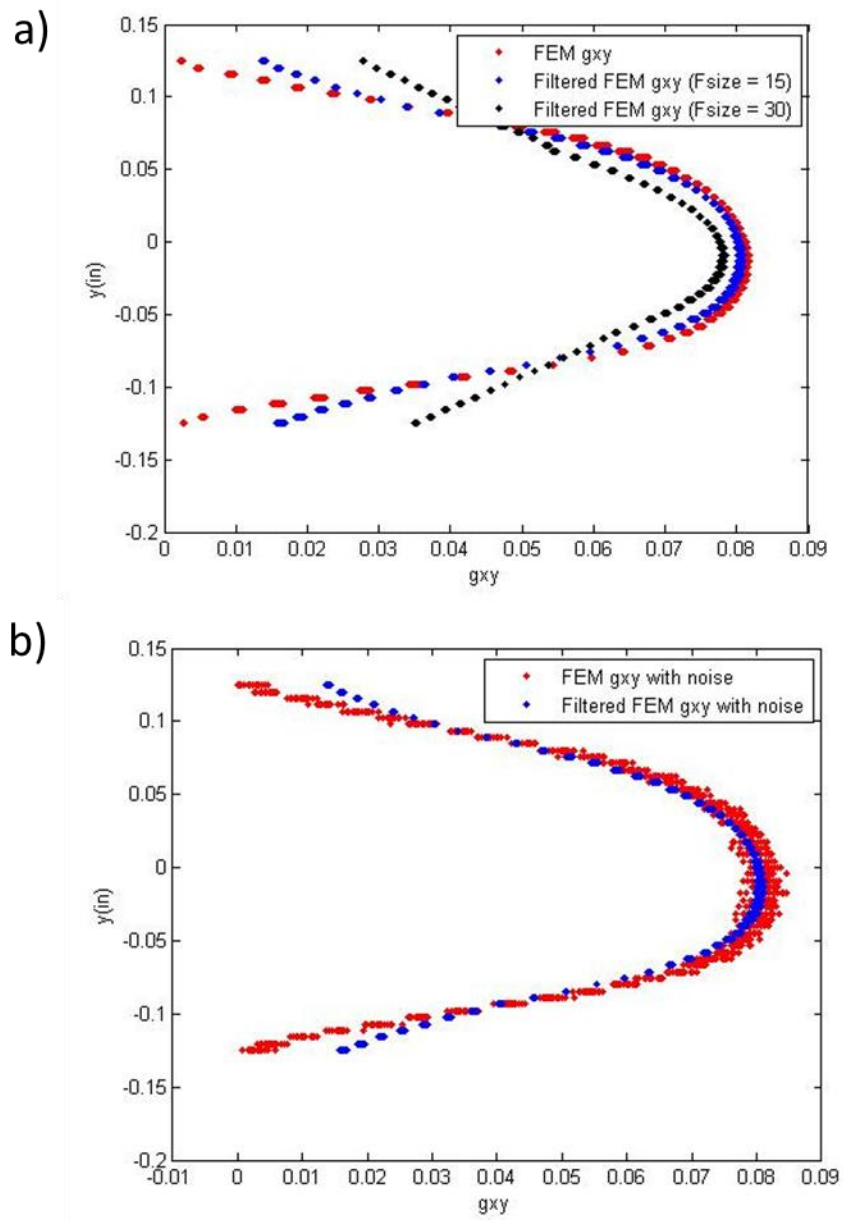


Figure 5-3 Filtered and unfiltered interlaminar shear strain distribution through the thickness and between supports of an FEM simulated IM78552 SBS specimen at close to failure loads (a) without noise (b) with noise

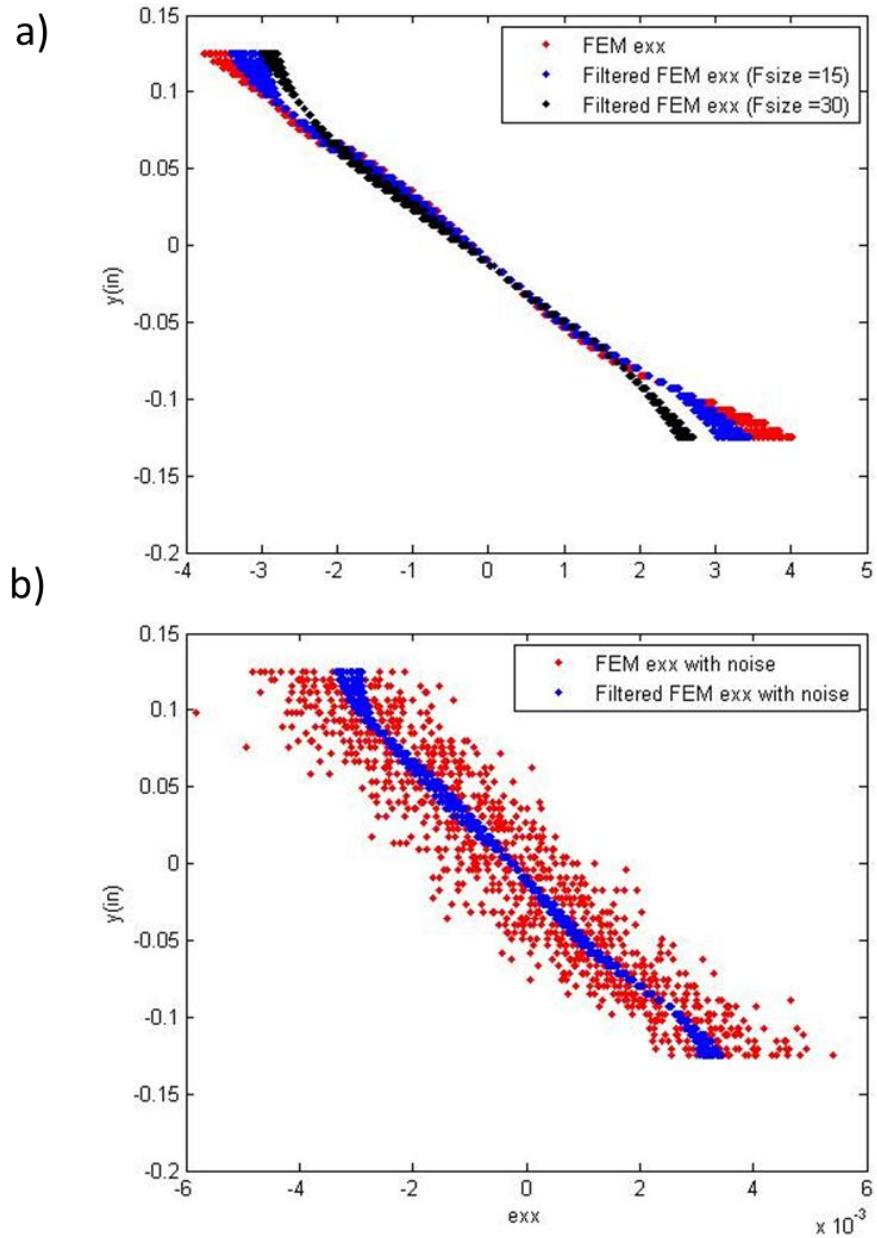


Figure 5-4 Filtered and unfiltered axial strain distribution through the thickness and between supports of an FEM simulated IM78552 SBS specimen at close to failure load a) without noise (b) with noise

5.2.1.2 S2-glass/E773-epoxy

The strain distributions for S2-glass/E773-epoxy come from a finite element simulation of a 1.2 inch short beam shear specimen with an 846 lb applied load, corresponding to an approximate peak shear stress of 10 ksi. Random noise, with magnitudes between 0 and .002, was added to the strain values. For shear strains this value is doubled. Typical glass/epoxy SBS specimens are analyzed using the following input parameters for Vic 3D analysis, 35 subset size, 7 step size, and 15 filter size for the strain computations. For this simulation a 15x15 gaussian filter was applied to both the shear strains and the axial strains obtained from FEM. The resulting strain distributions in the 2 mm (.079 in) region of interest can be seen in Figure 5-5 and Figure 5-6, where the simulated results are shown with and without added noise. For an idealized case, noise free, the peak interlaminar shear strain reduces by approximately 3% of its original value, where the estimated noise magnitude reaches approximately 7% of the peak shear strain.

The maximum axial strain is much lower than the maximum shear strain, reaching a maximum strain of approximately .008 at this load level compared to a maximum interlaminar shear strain of approximately .06. With the noise magnitude estimated to as much as 25% of the maximum axial strain, it is important that an appropriately large filter is applied to the data. The axial strain distribution with added noise is shown in Figure 5-6 (b), where it can be observed that the Gaussian filter successfully reduces the noise in the data to acceptable levels.

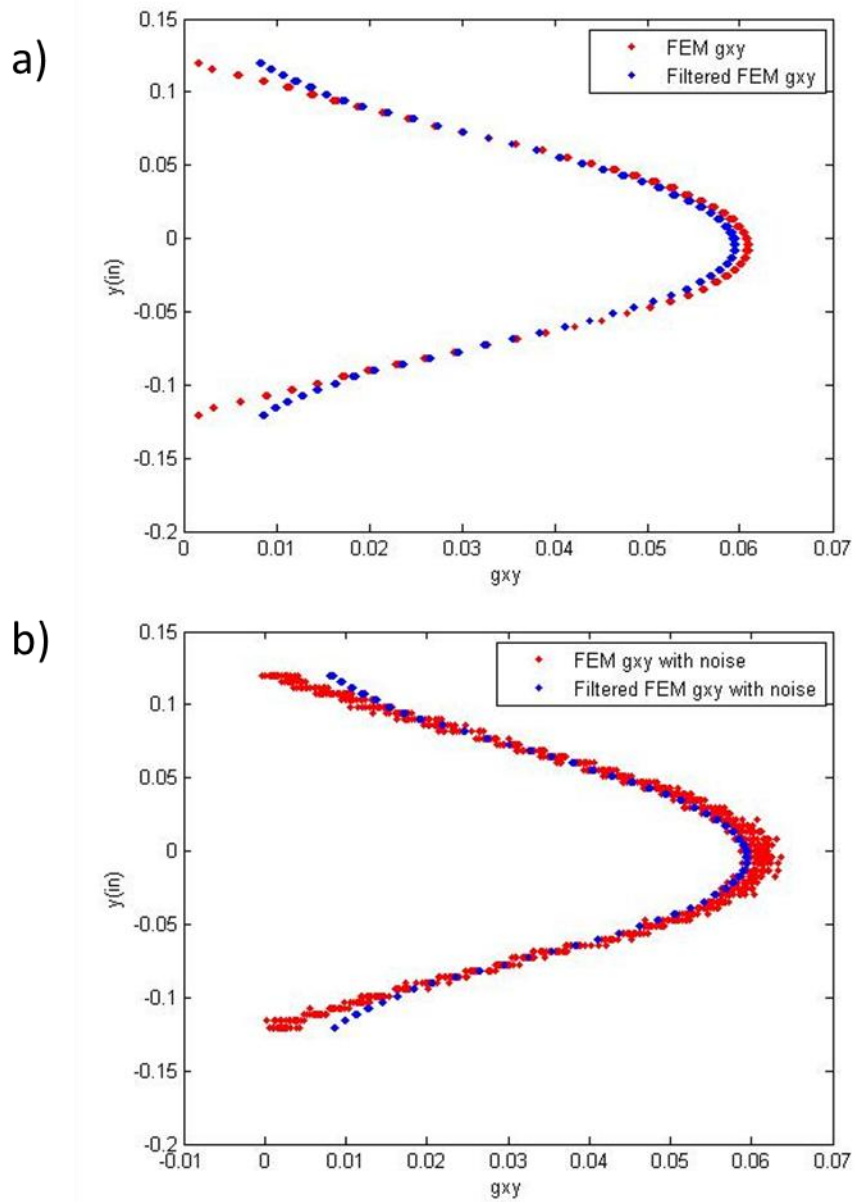


Figure 5-5 Filtered and unfiltered interlaminar shear strain distribution through the thickness and between supports of an FEM simulated S2E773 SBS specimen at close to failure load (a) without noise (b) with noise

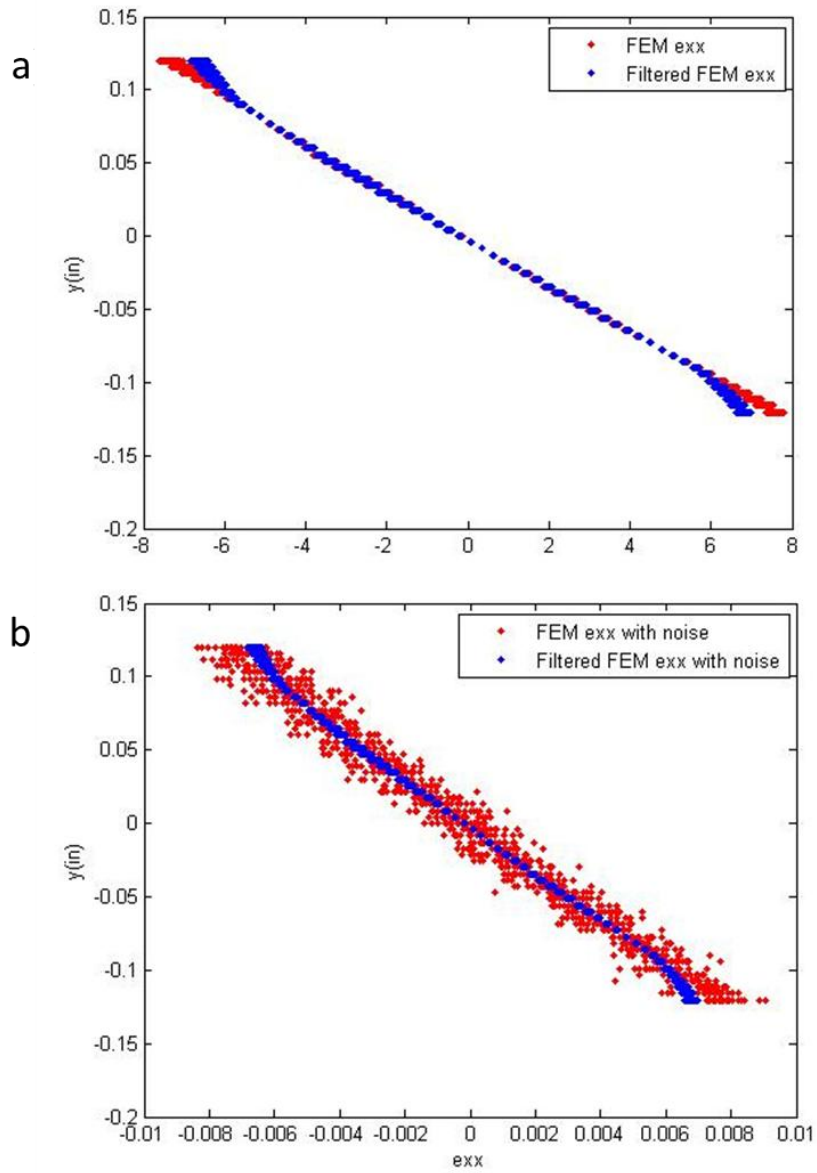


Figure 5-6 Filtered and unfiltered axial strain distribution through the thickness and between supports of an FEM simulated S2E773 SBS specimen at close to failure load (a) without noise (b) with noise

5.2.2 Impact Tests

To simulate typical strain distributions for S2-glass/E773-epoxy SBS specimens subject to 4.4m/s impact velocity, surface strains were obtained from a nonlinear explicit FEM model for a 1.2 inch S2-glass/E773-epoxy SBS specimen subject to 4.4m/s impact velocity, resulting in $10^2(1/s)$ strain rates, at .240 μ s after initial impact, corresponding to an approximate peak shear stress of 13.7 ksi. The FEM model is based on DIC strain measurements. Random noise with a magnitude between 0 and .007 was applied to the shear strain values. The magnitude of noise was determined from the sigma output variable. A larger noise magnitude is expected from impact tests in comparison to static tests, based on experimental considerations including lighting, motion of the specimen, resolution of the camera system, etc. Typical glass/epoxy SBS impact specimens were analyzed using the following input parameters in Vic 3D analysis, 17 subset size, 5 step size, and 11 filter size for the strain computations. The distance between DIC data points using these input parameters corresponds well with the distance between nodes, in the region far from loading nose and support, in the FEM simulation of the impact SBS specimen. For this simulation an 11x11 Gaussian filter was applied to the FEM based interlaminar shear strain distribution.. Figure 5-7 (a) demonstrates how the Gaussian filter alters the noise-free shear strain distribution of an S2-glass/E773-epoxy SBS specimen subject to a 4.4 m/s impact velocity. Even under near ideal experimental conditions noise will be introduced to the DIC measurements. Figure 5-7 (b) demonstrates how the Gaussian filter affects the noisy shear strain data. From these simulations, we can see how both the noise and filter change the peak shear strain values. A peak shear strain value of approximately .045 is estimated from finite element simulations. The Gaussian filter effectively reduces this value by 9%, or .004, which is large enough to be considered significant. However, the noise in the data could alter the peak shear strain values even

more significantly. For further verification of the peak shear strain reduction caused by the filter, static SBS specimens were analyzed using comparatively large DIC input parameters. A subset size of 69, step size of 20, and filter size of 11 was used to reanalyze the static specimens. An average peak shear strain decrease of 9% is also observed from the DIC shear strain distributions obtained using the larger input parameters. To reduce the error introduced in the peak shear strain values by the filter, the physical size of the filter must be reduced. This can be accomplished using high speed cameras that have higher resolution.

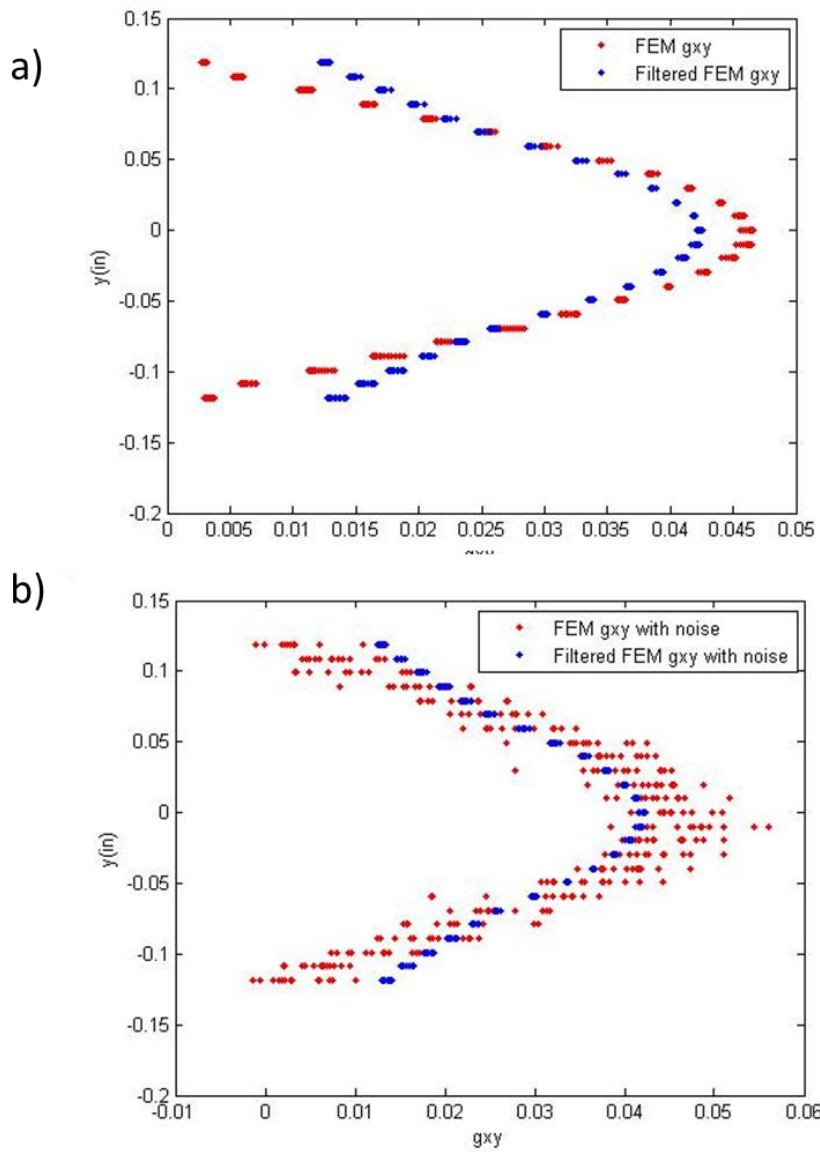


Figure 5-7 Interlaminar shear strain distribution through the thickness and between supports of an S2/E773 SBS specimen subject to an initial impact velocity of 4.4 m/s at 240 μ s after initial impact based on FEM strains and Gaussian filtered FEM strains (a) without noise (b) with noise

Chapter 6

Conclusion and Future Work

A reliable method for assessment of three-dimensional material constitutive properties including tensile, compressive, and shear stress-strain relations is developed in this work. The method is based on the short beam specimens subject to three point loading, and the digital image correlation (DIC) full field deformation measurement technique. Tensile and compressive Young's moduli, Poisson's ratio, and shear stress-strain response in the plane of loading are measured in a single SBS test using simple stress and modulus approximations. The concept is demonstrated for both glass/epoxy and carbon/epoxy unidirectional composite tape material systems, where SBS specimens are machined from a single panel and loaded in the three principal material planes. While additional specimens can be machined through the thickness of thick panel composites for interlaminar tensile and compressive properties. Good agreement was found from test results measured using the short beam shear method and alternative verification test methods. Custom SBS test method design resulted in consistent interlaminar shear failure mode for both glass/epoxy and carbon/epoxy material systems under various loading conditions. Linear axial strain distributions through the specimen thickness were observed for multiple composite material systems. Such observations allow for simple closed form geometric stress approximations and simple tensile and compressive axial modulus solutions to be developed. Furthermore, this test method was demonstrated for both fatigue and impact loading conditions. FEM results confirm that simple shear stress approximations (20), developed from static equilibrium, apply for specimens subject to low impact velocities.

It is worth noting that simple axial normal and shear stress approximations rigorously derived based on the observations from the full-field strain measurement and

equilibrium, are essentially the same as one would determine based on the classical beam theory which assume rigid cross section remaining perpendicular to the neutral axis during deformation (Bernoulli-Euler assumption). So one can get away with the stresses determined based on erroneous kinematic assumptions. It is also noteworthy that characterization of the multiple material constitutive properties confirms the accuracy of the transverse isotropy approximation for the stiffness properties for materials tested. Transverse isotropic material approximation reduces the number of tests to determine the stress-strain constitutive properties. However, the strength properties of composites are not transversely isotropic and the transverse isotropy assumptions are not accurate in characterizing failure mechanisms.

Symmetric loading of the specimen, ensured using an alignment device, should produce symmetric strain distributions between the left and right side of each specimen throughout the majority of the loading history. Observations of nonsymmetric axial strain distributions on the left and right side of each specimen forced the author to look into the reliability of the axial strain measurements. Further investigation revealed a strong dependence of the axial strain values on the axes of measurement in regions of comparatively high shear strains. For carbon/epoxy unidirectional SBS specimens loaded in the (1-3) principal material plane, small transformations of the axial strain distribution can lead to large shifts between the transformed and original distribution. Alignment of the coordinate axes corresponding to the strain measuring device with the material principal coordinate axes in the SBS specimen is found to be imperative for reliable axial strain measurements along the thickness of the specimen. The proper orientation of the coordinate system used for assessment of strain in the process to determine material constitutive properties, including tensile and compressive axial modulus, is critical to accuracy of measuring such properties. For DIC measurements,

coordinate transformations can easily be applied to the data in the post-processing stage of analysis to correct any coordinate misalignment.

Unlike in the tensile and compressive modulus assessment, sensitivity to coordinate axes alignment is not observed for the interlaminar shear strain distributions in the SBS specimens. However, for beams with short spans, it appears that the maximum shear stress in the beam is lower than simple shear stress approximations (20) predict producing a larger “apparent” interlaminar shear strength. As the span increases, the transverse normal stresses decrease in the region equidistant from loading nose and supports and the “apparent” shear stress approximation (20) becomes a more accurate approximation. The difference in “apparent” interlaminar shear strength and true interlaminar shear strength becomes more obvious in the higher axial stiffness materials, like carbon/epoxy unidirectional composites, which fail at higher shear stresses further in the nonlinear regime compared to the lower axial stiffness materials, like glass/epoxy composites. A reduced geometric stress model (31) was derived from three dimensional FEM-based iterative stress calculations for carbon/epoxy SBS specimens with varying s/t ratios. If proven general, such approximation can be used to replace the FEM-based iterative stress procedure, reducing the complexity and time associated with the developed SBS method for accurate material characterization.

The larger transverse normal stresses, found in the specimens subject to smaller s/t ratios, do not appear to influence the axial tensile and compressive moduli measurements obtained using the closed form solution, Eq. (20). This could be a result of the transverse normal stresses in the location equidistance from loading nose and support being most noticeable in the mid-plane of the beam where axial stress is small. One dimensional Hooke’s law is shown to be a good basis for approximation for the axial normal stresses along the thickness even at lower s/t ratios, such as 4.8.

Small errors introduced in the DIC-based Lagrange strain tensor calculations for the static SBS specimens ensure reliability of these measurements. Larger errors are observed in the DIC-based shear strain calculations for the impact SBS specimens, mostly caused by the low resolution of the high speed stereo camera system. By increasing the resolution of these cameras the magnitude of the filtering errors can be reduced, making the peak shear strain calculations more reliable. Simplicity of the short beam and accuracy of the constitutive property approximations make the presented experimental method attractive for measurement of three-dimensional stress-strain relations for anisotropic materials at various load rates.

The methodology developed in this work can be further expanded to capture spatial variability of basic material properties in composites. The basis of assessing constitutive properties in the principal material directions from unidirectional SBS tests was the identification of regions which exhibit simple stress states that can be used to extract the individual components of the stress-strain behavior till material failure. The stress state in a SBS specimen is complex, where stress concentrations exist at the loading nose and supports. However, midway between supports and loading nose the SBS specimens do exhibit regions of pure shear stress and strain along the neutral axis until failure. Despite having strain data over the entire surface of the specimen, only small regions along the neutral axis were used to extract the shear stress-strain response; and cross sections in the small .079 in. (2 mm) region were used to extract the tensile and compressive modulus values. Most of the strain data essential for assessment of the spatial variability of the material properties as well as various couplings, such as the effect of transverse compression on shear stress-strain constitutive relations, have been ignored thus far. A technique for measuring spatial variability based on virtual fields method is introduced in References [49, 50], however,

this method requires assumptions of the formulation of the stress-strain constitutive model. Such assumptions might not reflect the true material behavior. In particular, a priori assumption in the formulation of a material nonlinear constitutive model might result in wrong conclusions. The assumed nonlinear formulation entails the process of determining the model parameters using the virtual fields method being a curve fitting exercise. Therefore, an alternative method must be developed which does not require predefined constitutive model formulation. A good start is to introduce a method which enables the measurement of strain components and independent geometric initial approximation of the corresponding stresses. Then true relations between the stresses and strain can be determined. As long as the initial step does not include a priori formulation of the stress-strain relations, an iterative process will determine the model which captures the physics of material behavior. The methodology developed in this work provides the initial step as well as the foundation for further development.

References

- [1] A. Dobyns, C. Rousseau and P. Minguet, *Comprehensive Composite Materials*, Elsevier Science Ltd., 2000.
- [2] O. Bauchau and J. Craig, *Structural Analysis*, Springer, 2009.
- [3] V. Volovoi, D. Hodges, D. Cesnik and P. Popescu, "Assessment of Beam Modeling Methods for Rotor Blade Applications," *Mathematical and Computer Modeling*, Vol. 33, no. 10, pp. 1099-1112, 2001.
- [4] American Society for Testing and Materials, *Standard test method for short-beam strength of polymer matrix composite materials and their laminates*, ASTM Standard D 2344/D 2344M, 2006.
- [5] V. Vasiliev and E. Morozov, *Advanced Mechanics of Composite Materials*, Oxford: Elsevier, 2007.
- [6] K. T. Kedward, "On the short beam shear test method," *Fibre, Science and Technology*, vol. 5, pp. 85-95, 1972.
- [7] A. Makeev, C. Ignatius, Y. He and B. Shonkwiler, "A test method for assessment of shear properties of thick composites," *Journal of Composites*, vol. 43, no. 25, pp. 3091-3105, 2009.
- [8] S. Timoshenko and J. Gere, *Mechanics of Materials Fourth Edition*, Boston: PWS Publishing Company, 1990.
- [9] Y. Wenbin, D. Hodges, V. Volovoi and C. Cesnik, "On Timoshenko-like modeling of initially curved and twisted composite beams," *International Journal of Solids and Structures*, vol. 39, pp. 5101-5121, 2002.
- [10] Y. He, A. Makeev and B. Shonkwiler, "Characterization of nonlinear shear properties for composite materials using digital image correlation and finite element analysis," *Composites Science and Technology*, vol. 73, pp. 64-71, 2012.

- [11] D. Stouffer and L. Dame, *Inelastic Deformation of Metals*, New York: John Wiley and Sons, Inc., 1996.
- [12] G. D. Renieri and H. C. T., *Nonlinear analysis of laminated fibrous composites*, Tech. Rep. VPI-E-76-10, 1976.
- [13] H. T. Hahn and S. W. Tsai, "Nonlinear elastic behavior of unidirectional composite laminae," *Journal of Composite Materials*, vol. 7, pp. 102-118, 1973.
- [14] D. Adams, E. Lewis, "Current status of composite material shear test methods," *SAMPE*, vol. 31, no. 6, pp. 32-41, 1984.
- [15] D. Adams, M. Xie, "Study of three- and four- point shear testing of unidirectional composite materials," *Composites*, vol. 26, no. 9, pp. 653-659, 1995.
- [16] W. C. Cui, M. R. Wisnom and M. Jones, "Failure mechanisms in three and four point bending tests of unidirectional glass/epoxy," *Journal of Strain Analysis*, vol. 27, no. 4, pp. 235-243, 1992.
- [17] J. Whitney and C. E. Browning, "On the short beam shear tests for composite materials," *Experimental Mechanics*, vol. 25, no. 3, pp. 294-300, 1985.
- [18] J. M. Whitney, "Elasticity analysis of orthotropic beams under concentrated loads," *Composites Science and Technology*, vol. 22, pp. 167-184, 1985.
- [19] A. Makeev, "Interlaminar shear fatigue behavior of glass/epoxy and carbon/epoxy composites," *Composites Science and Technology*, vol. 80, pp. 93-100, 2013.
- [20] M. Xie and D. F. Adams, "Contact finite element analysis of three- and four- point shear test for composite materials," *Computers and Structures*, vol. 57, no. 2, pp. 183-91, 1994.
- [21] MIL-HDBK-17-1F, *Composite Materials Handbook, Vol 1: Polymer Matrix Composite Guidelines for Characterization of Structural Materials*, U.S. Department of Defense, 2002.

- [22] A. Makeev, Y. He, P. Carpentier and B. Shonkwiler, "A Method of measurement of multiple constitutive properties for composite materials," *Composites: Part A*, vol. 43, no. 12, pp. 2199-2210, 2012.
- [23] Y. He, *Matrix-dominated constitutive laws for composite materials*, Atlanta: Georgia Institute of Technology, 2010.
- [24] E. Q. Lewis and D. F. Adams, "An Evaluation of Composite Material Shear Test Methods," in *Report UW-CMRG-R-91-103*, Wyoming, University of Wyoming , 1991.
- [25] M. Rosensaft and G. Marom, "Evaluation of Bending Test Methods for Composite Materials," *Journal of Composites Technology and Research*, vol. 7, no. 1, 1985.
- [26] A. Christiansen, J. Lilley and J. Shortall, "A Three Point Bend Test for Fibre Reinforced Composites," *Fibre Science and Technology*, vol. 7, no. 1, pp. 1-13, 1974.
- [27] G. Hanna and S. Steingiser, "Defining the Adhesive Characteristics in Advanced Composites," *ASTM STP 460*, pp. 182-191, 1969.
- [28] M. Sutton, J. H. Yan, V. Tiwari, H. W. Schreier and J. J. Orteu, "The effect of out of plane motion on 2D and 3D digital image correlation measurements," *Optics and Lasers in Engineering*, vol. 46, pp. 746-757, 2008.
- [29] M. Sutton, J. Orteu and H. W. Schreier, *Image Correlation for Shape, Motion, and Deformation Measurements*, New York: Springer, 2009.
- [30] H. W. Schreier, J. R. Braasch and M. Sutton, "Systematic errors in digital image correlation caused by intensity interpolation," *Optics Engineering*, vol. 39, no. 11, pp. 2915-2921, 2000.
- [31] Y. Wang, P. Lava, S. Coppieters, M. De Strycker, P. Van Houtte and D. Debruyne, "Investigation of the Uncertainty of DIC Under Heterogeneous Strain States with Numerical Tests," *Strain*, 2012.
- [32] J. Vinson and R. Sierakowski, *The Behavior Of Structures Composed Of Composite Materials*, Springer, 1986.

- [33] P. Carpentier and A. Makeev, "Novel Methods for Assessment of Three Dimensional Constitutive Properties for Composites," in *Advances in Fracture and Damage Mechanics*, Nagasaki, 2010.
- [34] M. Xie and D. F. Adams, "Study of three- and four-point shear testing of unidirectional composite materials," *Composites*, vol. 26, no. 9, pp. 653-659, 1995.
- [35] S. Lekhnitskii, *Anisotropic Plates*, New York: Gordon and Breach Publishers, 1968.
- [36] "<http://www.hexcel.com/Products/Aerospace/APrepregs.>," [Online].
- [37] M. May and S. Hallett, "An Assessment of Through Thickness Shear Tests for Initiation of Fatigue Failure," *Composites Part: A*, vol. 41, pp. 1570-1578, 2010.
- [38] Y. Nikishkov, A. Makeev and G. Seon, "Progressive Fatigue Damage Simulation Method for Composites," *International Journal of Fatigue*, vol. 48, pp. 266-279, 2013.
- [39] R. Lakes, *Viscoelastic Materials*, New York: Cambridge University Press, 2009.
- [40] A. Yigit, A. Christoforou, "Impact Dynamics of Composite Beams," *Composite Structures*, Vol. 32, pp. 187-195, 1995.
- [41] D. Adams and D. Walrath, "Current status of the Iosipescu shear test," *Journal of Composites*, vol. 21, pp. 494-506, 1987.
- [42] American Society for Testing and Materials, "Standard test method for shear properties of composite materials by the V-notched beam method," *ASTM Standard D 5379/D 5379M*, 2005.
- [43] H. Henjen, J. Morton and G. Farley, "Nonlinear numerical analysis of the Iosipescu specimen for composite materials," *Composites Science and Technology*, vol. 50, pp. 355-365, 1994.
- [44] Y. Xing, C. Poon and C. Ruiz, "A whole field strain analysis of the Iosipescu specimen and evaluation of experimental errors," *Composites Science and Technology*, vol. 47, pp. 251-259, 1993.

- [45] ASTM Standard D 7264/D 7264M, *Standard test method for flexural properties of polymer matrix composites*, ASTM International, 2007.
- [46] American Society for Testing and Materials, "Standard test method for measuring the curved beam strength of a fiber reinforced polymer matrix composite," *ASTM Standard D 6415*, 2006.
- [47] K. Kedward, R. Wilson and S. Mclean, "The flexure of simply curved composite shapes," *Composites*, vol. 20, no. 6, pp. 527-553, 1989.
- [48] Y. Q. Wang, M. Sutton, H. A. Bruck and H. W. Schreier, "Quantitative error assessment in pattern matching: effects of intensity pattern noise, interpolation, strain and image contrast on motion measurements," *Strain*, vol. 45, pp. 160-178, 2009.
- [49] M. Grediac, F. Auslender and F. Pierron, "Applying the Virtual Fields Method to Determine the Through-the-thickness moduli of Thick Composites with a Nonlinear Shear Response," *Composites Part A*, vol. 32, pp. 1713-1725, 2001.
- [50] M. Grediac and F. Pierron, "Numerical Issues in the Virtual Field," *International Journal for Numerical Methods in Engineering*, vol. 59, pp. 1287-1312, 2004.

Biographical Information

Paige Carpentier received a bachelor of science degree in Electrical Engineering from Georgia Institute of Technology in 2007. She began her master's degree in the Aerospace Engineering department at Georgia Tech under the advisement of Dr. Erian Armanios in the summer of 2008. In January 2009 she started working in experimental testing with Dr. Andrew Makeev. She received a master's of science degree in Aerospace Engineering from Georgia Tech in the summer of 2010 under the advisement of Dr. Makeev. She transferred to University of Texas at Arlington in January of 2011 to continue her work with Dr. Makeev. Her main research focus is on the development of the short beam shear test method for three dimensional material characterization of polymer composites. Her projects were in collaboration with industry leaders such as Bell helicopter, Boeing, Sikorsky, and Kaman.